

The Nigerlikasik supracrustal belt in the Kvanefjord area, South-West Greenland: Geochemistry and petrology of a tholeiitic—calc-alkaline metavolcanic sequence

Martin B. Klausen, Thomas F. Kokfelt, Nynke Keulen,
John C. Schumacher & Alfons Berger



GEOLOGICAL SURVEY OF DENMARK AND GREENLAND
MINISTRY OF CLIMATE AND ENERGY



GEUS

The Nigerlikasik supracrustal belt in the Kvanefjord area, South-West Greenland: Geochemistry and petrology of a tholeiitic—calc-alkaline metavolcanic sequence

Martin B. Klausen, Thomas F. Kokfelt, Nynke Keulen,
John C. Schumacher & Alfons Berger

**The Nigerlikasik supracrustal belt in the Kvanefjord
area, South-West Greenland: Geochemistry and pe-
trology of a tholeiitic—calc-alkaline metavolcanic
sequence**

Martin B. Klausen, Thomas F. Kokfelt, Nynke Keulen,
John C. Schumacher and Alfons Berger

Table of contents

Editorial note	4
Abstract.....	5
Introduction	6
Regional setting	7
Field relationships, rock classification and geochronology.....	9
The Nigerlikasik section	11
Geochronology.....	15
Structural overprint.....	18
Igneous protolith classification	22
Multi-elemental statistical analysis	23
Stratigraphic variations.....	25
Possible fractionating phases	31
Geochemical discrimination	35
Petrogenesis and differentiation.....	40
Model implications.....	44
Combined island arc and backarc	44
Single island arc with slab melting.....	45
Progressive island arc to crustal accretion	47
Single island arc without significant crustal melting.....	48
Summary and conclusions	49
Acknowledgements	51
References.....	51
Appendices	56
Appendix 1: Zircon U/Pb age data for felsic sheets and TTG rocks at Nigerlikasik supracrustal sequence	57
Appendix 2: Sample processing and geochemical analysis at the Central Analytical Facility (CAF, University of Stellenbosch)	60
Appendix 3: Geochemical data for the Nigerlikasik supracrustal rock sequence	63

Editorial note

This GEUS report is a partial contribution within the framework of the 'Homogenisation' project, which is a co-financed project by GEUS and Greenland's Bureau of Minerals and Petroleum (BMP) that has had the main goal to reassess the geology in the area of SW Greenland between 61.5 and 64.0°N. The aim of this report is to present and discuss various aspects of the rocks from the SW Greenland Archaean Craton from a geochemical and petrological perspective. The data presented represent some of the results stemming from the field work carried out in the Paamuit area during the 2010 field season.

This report covers the field work of five persons over 2.5 days, as well as the subsequent geochemical and geochronological studies that were done on a single meta-volcanic profile situated on the north of Nigerlikasik in the inner part of Kvanefjord. Complementary data and information about the structural geology of the Nigerlikasik profile are given in Keulen *et al.* (2011), whereas structural, geochemical as well as Sm-Nd and Lu-Hf isotopic data and information on similar supracrustal units from different parts of southern West and South-West Greenland are given in Szilas *et al.* (2011a), as well as Szilas (2012) and Szilas *et al.* (2011b, 2012a, b).

Abstract

The Archaean Craton in South-West Greenland is made up of a series of predominantly amphibolite facies crustal terranes, which in the Kvanefjord area (~62°S) are dominated by foliated TTG gneisses and a number of inter-folded amphibolite belts, named Kvanefjord amphibolites by Escher (1971). These ca. 4 km wide and synformally folded and faulted belts appear as dismembered parts of a presumed continuous supracrustal sequence. One supracrustal belt on the Nigerlikasik peninsula was visited during the 2010 GEUS-led (co-sponsored by Greenland Bureau of Mining and Petroleum) field expedition in the area, with the intent of establishing a detailed stratigraphical log and a dense sampling profile for geochemical and geochronological characterisation.

The sequence at Nigerlikasik is relatively well-preserved and coherent, and describes a compositional evolution from ultramafic serpentinites near the base (~30 m), to mafic amphibolites through mid-section (~220 m), to felsic biotite-hornblende (bio-hbl) schists in the top-section (~300 m). All rocks are of likely igneous origins based on examples of relict volcanic structures, such as possible *fiamme*-textured ignimbrites, pyroclastic breccia-flows and rare pillow-basalts. Underlying parts of the lava sequence was intruded by a small number of syn-volcanic gabbroic and felsic feeder intrusions. The latest magmatic activity is represented by concordant to obliquely cross-cutting aplite sheets (<2 m wide) that dominate at the base (closer to the contact to the surrounding TTG's), but are found up through the entire sequence (decreasing in abundance upwards).

A total of 99 rock samples were collected from the ~550 m thick metavolcanic section, including 6 samples from the TTG 'basement' and aplite sheets of similar compositions. Four of these aplite sheets were dated by LA-ICPMS zircon U/Pb dating at GEUS, yielding fairly consistent igneous ages of (1) 2929 ± 5 , (2) 2931 ± 4 , (3) 2913 ± 5 and (4) 2922 ± 5 Ma, and providing a minimum age of the metavolcanic succession at ~2.93 Ga. One TTG gneiss at the base of the section yielded an igneous age of 2903 ± 4 Ma, but its geochemical similarity with the aplites supports a petrogenetic relationship between them.

The metavolcanic units are geochemically classified as part of a subalkaline succession, ranging from picrites, through basalts, basaltic andesites, andesites to dacites. With increasing stratigraphic height, there is an overall systematic increase in SiO₂ and corresponding decreases in CaO, MgO, Fe₂O₃ and MnO, with several off-set sub-trends typical of some crystal fractionation cycles. Whereas the lower mafic section defines a tholeiitic trend in an AFM-diagram, the upper felsic section is distinctly calc-alkaline and cannot be petrogenetically related to the basaltic tholeiites through crystal fractionation, on the basis of many other geochemical characteristics. For example, the high-FeO_T and low-Al₂O₃/TiO₂ basaltic tholeiites have flat REE-patterns whereas the relatively low-FeO_T and high-Al₂O₃/TiO₂ calc-alkaline andesites-dacites have steep, HREE-depleted patterns that are more consistent with a deeper, garnet-bearing crustal source. In addition, the picrites could also *sensu lato* be referred to as low-Al₂O₃, yet Ti-enriched, Karasjok-type komatiitic basalts, without any preserved spinifex textures and only one sample with >18 wt% MgO.

It is uncertain whether the lower (ultra)mafic part of the Nigerlikasik metavolcanic section is made up of tholeiitic island arc basalts, derived from a hydrated juvenile mantle wedge, OIBs, or "hot" Archaean MORBs. The overlying andesites-dacites represent a more diagnostic calc-alkaline volcanic island arc suite, which (together with the ≤ 2930 Ma intrusive TTG?) could have been derived either from decreased proportions of partial melts from a garnet-bearing crustal source (e.g., a subducted oceanic slab) or through extensive high-P garnet-amphibole fractionation within a subcrustal magma reservoir.

Introduction

Archaean cratons are characterized by large volumes of tonalite-trondhjemite-granodiorite (TTG) gneiss terrains within which supracrustal greenstone belts preserve relict tholeiitic suites of mafic to ultramafic volcanic rocks, calc-alkaline suites of andesitic-rhyodacitic volcanic rocks, as well as sediments, intrusions, and possibly even obducted slices of the mantle (e.g., Condie 1981, de Wit 2004). Pervasive deformation and high metamorphic grades within these accretionary terranes often limit field interpretations, in which case bulk rock analysis of immobile geochemical data may assist in protolith identifications, discrimination into igneous-tectonic associations, as well as petrogenetic interpretations (e.g., Polat et al. 2011, and references therein).

The supracrustal belts of southern West and South-West Greenland are variably distributed amongst TTG gneisses across the Archaean craton, as illustrated in *Figure 1*. It is generally accepted that most TTG gneisses intruded into the supracrustal belts, when these at around 2.9 Ga amalgamated into accretionary terranes that stabilised at around 2.7 Ga (e.g., Nutman and Friend 2007, Windley and Garde 2009, Polat et al. 2009). Szilas (2012) and Szilas et al. (2011a, b, 2012a, b, and references therein) show that the supracrustal belts of southern West and South-West Greenland predominantly are made up of metamorphosed (greenschist-granulite but predominantly amphibolite facies) meta-igneous (tholeiitic basalt and calc-alkaline andesitic) protoliths of volcanic and intrusive origins, with subordinate occurrences of underlying ultramafic igneous rocks and overlying metasediment, which collectively resemble sections through oceanic crusts. After more than 40 years of research, it is still debated whether these fragments of oceanic crust initially formed along oceanic (back-arc) spreading centres (Kusky and Polat 1999, Furnes et al. 2007, 2009, Polat et al. 2008), as hot spot generated intraplate oceanic islands or plateaus (Campbell et al. 1989, Bickle et al. 1994, Arndt et al. 1997), along juvenile island arcs (Polat et al. 2011, Szilas 2012, Szilas et al. 2011a, b, 2012a, b), or as 'cratonic' flood basalts (Said et al. 2010). Correct determinations of their tectonic-igneous associations are further complicated by the possibility of radically different modes of mantle dynamics, mantle *versus* crustal melting and plate tectonic processes during the Archaean (e.g., Davies 1992, Zegers and van Keken 2001, Bedard 2006, van Huenen et al. 2008).

A case study on a ~550 m wide transect through the margin of the supracrustal belt north of Niglerlikasik is presented in this report, along which a detailed stratigraphic log and dense sampling for geochemical and geochronological characterisation was established during 2.5 days of field work in 2010. Ninety-nine samples were analysed for major (XRF) and trace (LA-ICPMS) element analyses, at the Central Analytical Facility (University of Stellenbosch, Appendix Table 1). The age data on zircons from 4 aplitic sheets and 1 TTG gneiss were acquired using a Laser Ablation – Sector Field – Inductively Coupled Plasma Mass Spectrometry (LA-SF-ICPMS), which has been set up at GEUS (Frei and Gerdes, 2009, Appendix Table 2). Our results elucidate a supracrustal belt made up of a composite sequence comprising a picrites and tholeiitic basalt suite, and calc-alkaline andesite-dacite suite, which provides further field constraints to proposed models. Based on whole rock geochemistry, we also find that all units bear a subduction zone signature, where the entire sequence arguably could be related to different petrogenetic processes during the evolution of a single island arc system. As a possible modification to Szilas et al's (2012a) model of mixing between mantle-derived tholeiitic basalts and lower crustal melts, we find that the calc-alkaline suite had to have been derived through either deeper garnet amphibolite crustal melting or high-P garnet+amphibole fractionation (Alonzo-Perez et al. 2009). We also do not completely dismiss the possibility of the tholeiitic suite being derived in a back-

arc rift and thereby end up also considering an additional three alternatives of (1) a combined arc and backarc setting, (2) contemporaneous hydrous mantle wedge and slab melting within a single, hot subduction zone setting, and (3) an evolving island arc to crustal accretion model (in addition to high-P garnet+amphibole fractionation), which all conform to the temporal and geochemical constraints imposed by the Nigerlikasik section.

Regional setting

The North Atlantic craton of southern West Greenland and South West Greenland is dominated by Paleo- to Mesoarchaeon orthogneisses of trondhjemite-tonalite-granodiorite (TTG) composition that often contain conformable layers of supracrustal rock sequences, mainly comprised of metavolcanic rocks and anorthosite complexes (Windley 1966), and rarer inclusions of ultramafic rocks and metasediments (*Figure 1*). These rock associations occur in what has been described as alternating amphibolite and granulite facies metamorphic belts (e.g., Escher 1971, Bridgwater *et al.* 1976, Pidgeon and Kalsbeek 1978).

A long-standing scientific debate regards the tectonothermal evolution of the Nuuk region (e.g., Bridgwater *et al.* 1974, Friend *et al.* 1987, 1988, 1996, Friend and Nutman 2005, Nutman *et al.* 1989, 2004, Nutman and Friend 2007, Windley and Garde 2009). Whereas the earliest work in the region envisaged a regional continuity in metamorphic history and rock ages throughout the entire Archaean SW Greenland (e.g. Bridgwater *et al.* 1974, Wells 1976), a terrane model by Coney *et al.* (1980) was initially adapted for the Nuuk region by Friend *et al.* (1987, 1988) and then for the more easterly located Isukasia and Kapisilik terranes (Friend and Nutman 2005, just north of *Figure 1*). Each tectonostratigraphic terrane is characterised by related orthogneiss complexes and distinct early histories (Friend *et al.* 1988). Neighbouring terranes are bound along folded mylonitic zones, interpreted as ductile shear zones that were generated during the progressive assemblage and amalgamation into a stabilising craton (Friend *et al.* 1987, 1988, Nutman *et al.* 1989). Friend *et al.* (1996) proposed that extensive ca. 2720–2700 Ma high-grade metamorphism occurred in response to crustal thickening caused by this terrane amalgamation.

The Tasiusarsuaq terrane represents the largest terrane of the entire Archaean SW Greenland as it extends from the southern part of the Nuuk region at the Amaralik fjord down to Frederikshåb Isblink (*Figure 1*). The Tasiusarsuaq terrane is characterised by TTG gneisses with intrusion ages of 2880–2860 Ma (Friend and Nutman 2005), but new geochronological data suggest that a significant crust forming event also took place at around 2920 Ma (Kokfelt *et al.* 2011). South of the Tasiusarsuaq terrane four smaller blocks have been identified, from north to south these are the: Sioraq, Paamuit, Neria and Sermiligaarsuk block. Friend and Nutman (2001) suggested that each of these blocks contain TTG gneisses of distinct ages and as such could be ascribed to distinct tectonometamorphic terranes. According to McGregor and Friend (1997), each of these tectonically-separated blocks or terranes can be characterised as follows: (1) The Sioraq block situated just south of the Isblink, contains granulite facies TTG rocks (2870–2830 Ma) that were partly retrogressed to amphibolite facies. (2) The Paamiut block contains younger TTG's (2870–2850 Ma) that show no evidence for metamorphism above amphibolite facies, (3) The TTG's within the Neria block (2940–2920 Ma) were metamorphosed to granulite facies, but totally retrogressed to amphibolite facies, (4) The Sermiligaarsuk block hosting the Tartôq Group supracrustal rocks and gneisses, were metamorphosed from greenschist and up to granulite facies (< 3000 Ma).

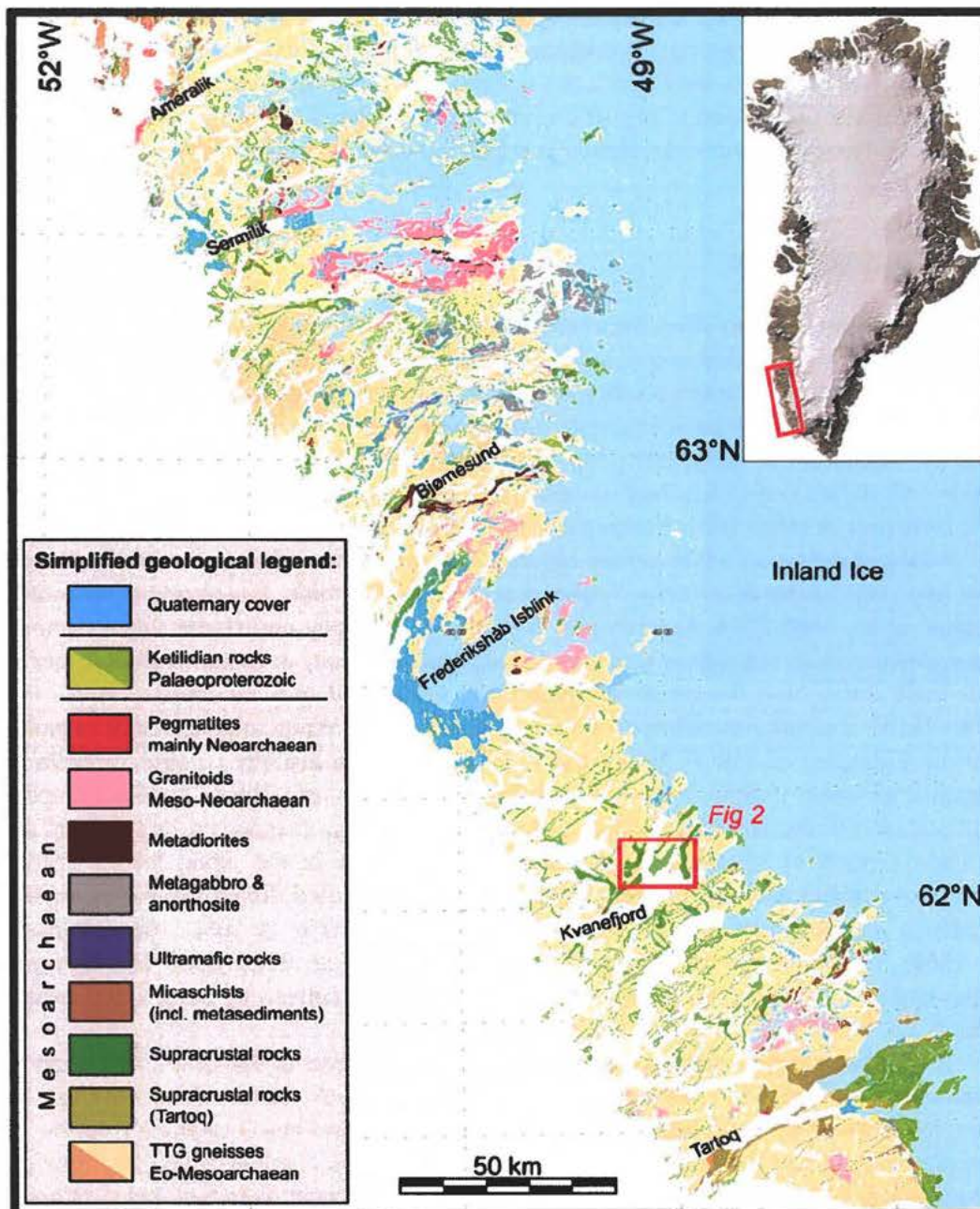


Figure 1: Geological map of southern West Greenland (from www.geus.dk/swgmap/), showing the location of the studied part of the Kvanefjord area (Figure 2). Note that this part of South-West Greenland is dominated by relatively large and continuous supracrustal bands.

An alternative to the terrane concept was described by Windley and Garde (2009) who envisaged the SW Greenland Archaean craton to consist of crustal blocks rather than petrogenetically unrelated terranes, *sensu stricto*. Based on a regional reinterpretation of available data on regional structures and metamorphism, Windley and Garde (2009) explained the apparent N-S change in metamorphic grade as reflecting a series of gently southward tilted blocks (i.e., in a regional scale domino-block fashion). Within each tilted block the northernmost part should therefore expose deeper erosional levels, reflected in a higher metamorphic grade of the rocks compared to the neighbouring block's southern part.

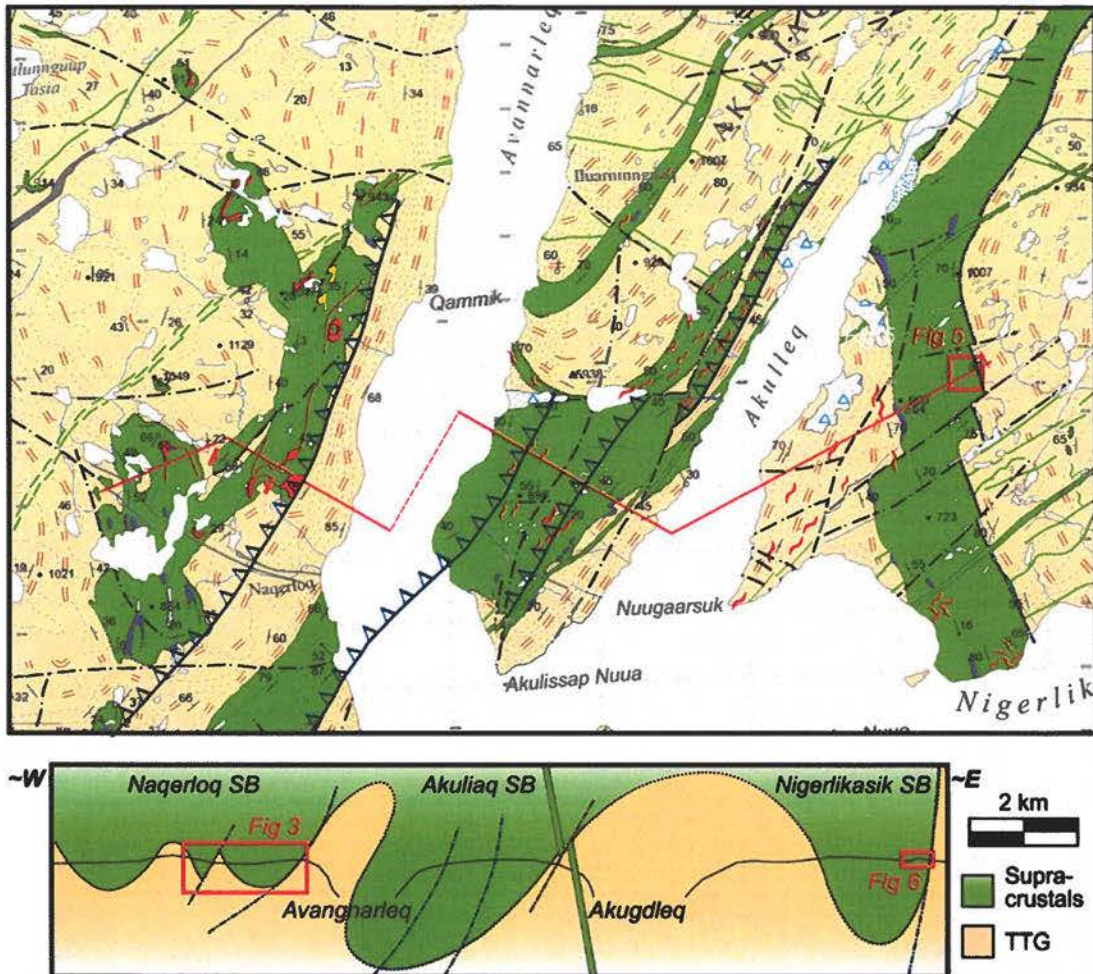


Figure 2: Extract from geological map sheet Nigerdlikasik 62 V. 2 Syd, in 1:100 000, showing three prominent supracrustal belts (SB; from W to E, Naqerloq, Akuliaq and Nigerlikasik) within foliated TTG gneiss, around three inland fjord-branches to Kvanefjord. Possible thrusts are added from Kolb (2011). A highly schematic cross section envisages these belts to be synformal relics from a coherent supracrustal sequence, deformed during the Archaean as well as cut by later, extensional and SW-NE trending Palaeoproterozoic MD2-dykes and associated normal faults. Inserted red squares indicate the locations where the supracrustals were studied by the authors in the field.

Field relationships, rock classification and geochronology

The studied part of the Kvanefjord area (~62°S) is located in the Sioraq/Paamiut block according to Friend and Nutman (2001) and the centre of the Kvanefjord block according to Windley and Garde (2009). The area is dominated by foliated TTG gneisses and a number of conformably inter-folded supracrustal (*sensu lato*) belts (SB, Figures 1-2, Escher 1971). As argued below, it is likely that the ultramafic-bearing margins of these belts also represent the basal parts of these supracrustal sequences, and that these up to 4 km-wide SB's may then be viewed as dismembered synforms of a continuous supracrustal sequence (Windley and Garde 2009), even if some components of thrusting along these contacts (Kolb 2011) cannot be ruled out. A similar overall stratigraphy of peripheral ultramafic rocks within the mafic amphibolites and an 'overlying' felsic core suggest that the most eas-

terly positioned Nigerlikasik supracrustal belt in *Figure 3(b)* is a tight synform with steep and pervasively foliated limbs (with few isoclinal folds), whereas the most westerly positioned Naqerloq supracrustal belt appears to be a more open and parasitically folded synform (*Figure 3*).

Variably boudinaged and sheared ultramafic units generally occur near the 'base' (i.e., at the margins) of these amphibolites, where they may reach thicknesses of up to 100 m (more commonly less than 10 m). The ultramafic units within the Naqerloq supracrustal belt occur amongst characteristic 'zebra-striped' amphibolite/aplite units (on cm-scale) and outcrop consistently above a rusty amphibolite marker horizon (2-5 m in thickness). The ultramafic outcrops within this belt often exhibit up to 20×2 cm large marginal "spinifex"-like textures with zones variably dominated by single tabular crystals and by more "spotted" crystal-rich agglomerates (*Figure 3a*), which in both cases are substantially coarser than typical komatiitic textures (e.g., Donaldson 1982). Thus, such coarser crystals may have formed within an intrusion or arguably be of a metamorphic rather than igneous origin.

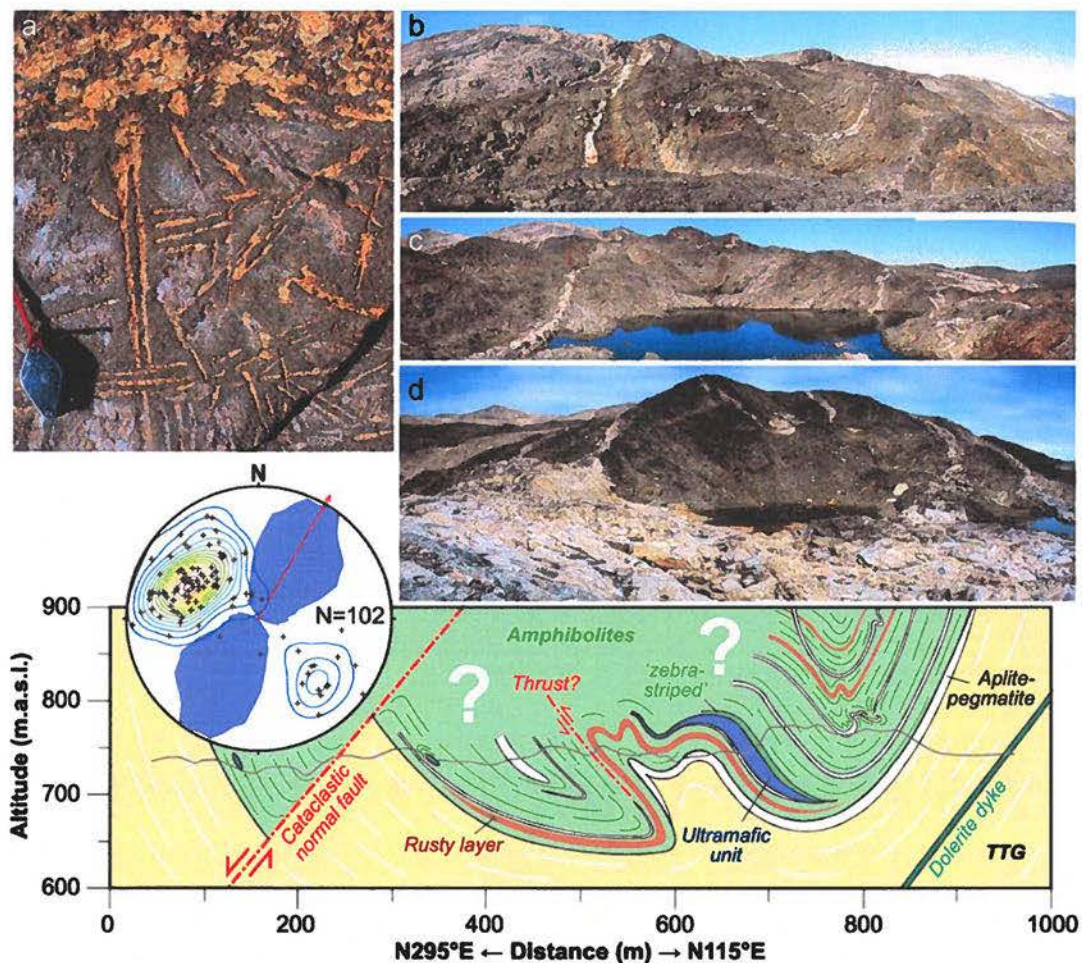


Figure 3: Cross section through the Naqerloq supracrustal belt, with field photos of: (a) Spinifex-like textures at the margin of an ultramafic unit, including an edge of its internally spotted zone. (b-d) Stratigraphically lower cross sections through a parasitically folded and shallowly north-plunging synform in the eastern part of the Naqerloq supracrustal belt (see *Figure 2* for location). Inserted lower hemisphere stereographical diagram shows a moving average strike rose plot together with Kamb's contoured distribution of poles to 102 foliation measurements across the Naqerloq supracrustal belt.

Archaean ultramafic rocks in South-West Greenland generally consist of either (1) talc ± anthophyllite ± actinolite ± phlogopite or (2) hornblende ± phlogopite ± diopside. The protoliths of talc-rich types were most likely peridotitic, and may have been subjected to some Si-metasomatism, whereas it appears that metasomatizing K-feldspar and quartz saturated fluids from felsic rocks converted plagioclase-bearing ultramafic protoliths into hornblendites (Schumacher *et al.* 2011). Normatively, ultramafic units (*senso lato*) within the Naqerloq supracrustal belt are classified as melanocratic olivine gabbronorites, whereas similar units from the western and eastern margin of the Nigerlikasik supracrustal belt classify as dunite (only one sample) and melanocratic (olivine) gabbronorites, respectively (Figure 4). Only the dunite sample from the western margin of Nigerlikasik supracrustal belt could potentially be a mantle rock, whereas the other three units have too much normative plagioclase and must therefore have been either cumulates or ultramafic intrusions/lavas. These ultramafic samples also display a large compositional variation within each unit, which most easily is ascribed to variable accumulation of mainly olivine and/or pyroxene. In this report we will focus on the generally much finer grained, and darker coloured ultramafic rocks from the eastern margin of the Nigerlikasik supracrustal belt, whereas a more regional study on the remaining ultramafic rocks will be published elsewhere.

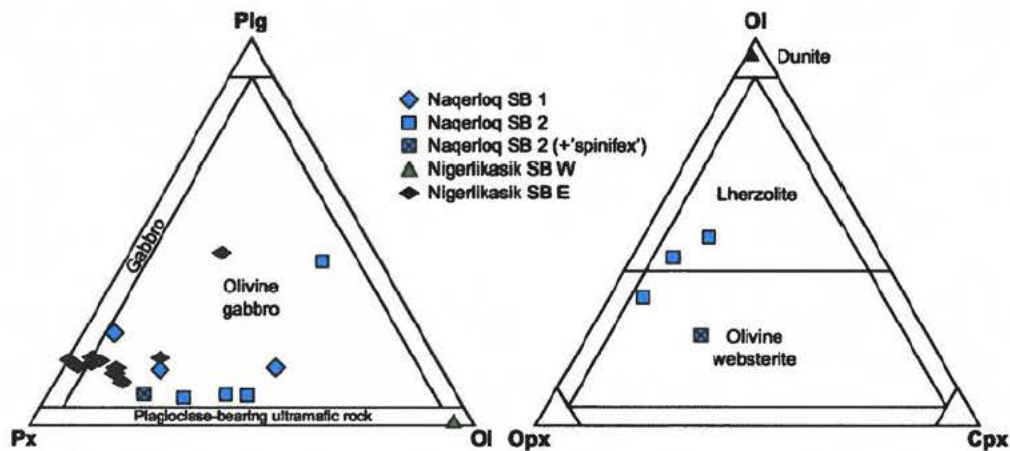


Figure 4: Normative proportions (Johansson, 1931) of plagioclase (plg), hypersthene (opx), diopside (cpx) and olivine (ol) of 21 samples from at least four ultramafic units in the Kvane-fjord area are plotted in an IUGS classification diagram for mafic rocks (left; Le Maitre, 2002). Only five of the least plg-normative samples from two units are plotted in the IUGS classification diagram for ultramafic rocks (right).

The Nigerlikasik section

The Nigerlikasik section comprises a transect that runs from the eastern margin of the supracrustal sequence and the contact to the surrounding TTG basement, and westward into the felsic unit of the Nigerlikasik supracrustal belt. The profile was logged and systematically sampled by the authors during 2.5 days of field work. Due to the belt's nearly vertical and N-S striking foliation, all observations and sample gps-locations are simply projected onto a ~550 m long E-W section (Figure 5). Logged observations are compiled into Figure 6, with overall stratigraphical changes illustrated by photographs (a-j) and more important details recorded by photographs (k-r).

The (ultra)mafic and felsic supracrustal units along the Nigerlikasik sections are generally fine grained, commonly layered down to a mm-scale, and are – as will be shown in

later geochemical sections – probably the metamorphic equivalent of (high-MgO) mafic and felsic volcanics, respectively (e.g., Le Maitre 2002). Some coarser grained and more likely intrusive units are intermittently distributed as up to 20 cm-wide ultramafic boudins within the supracrustal rock sequence, as well as one up to 15 m-thick meta-gabbroic layer in the upper part of the mafic supracrustal sequence. As all rocks described here have undergone metamorphism the prefix “meta” will furthermore be taken as implicit to all igneous rock names throughout this report.

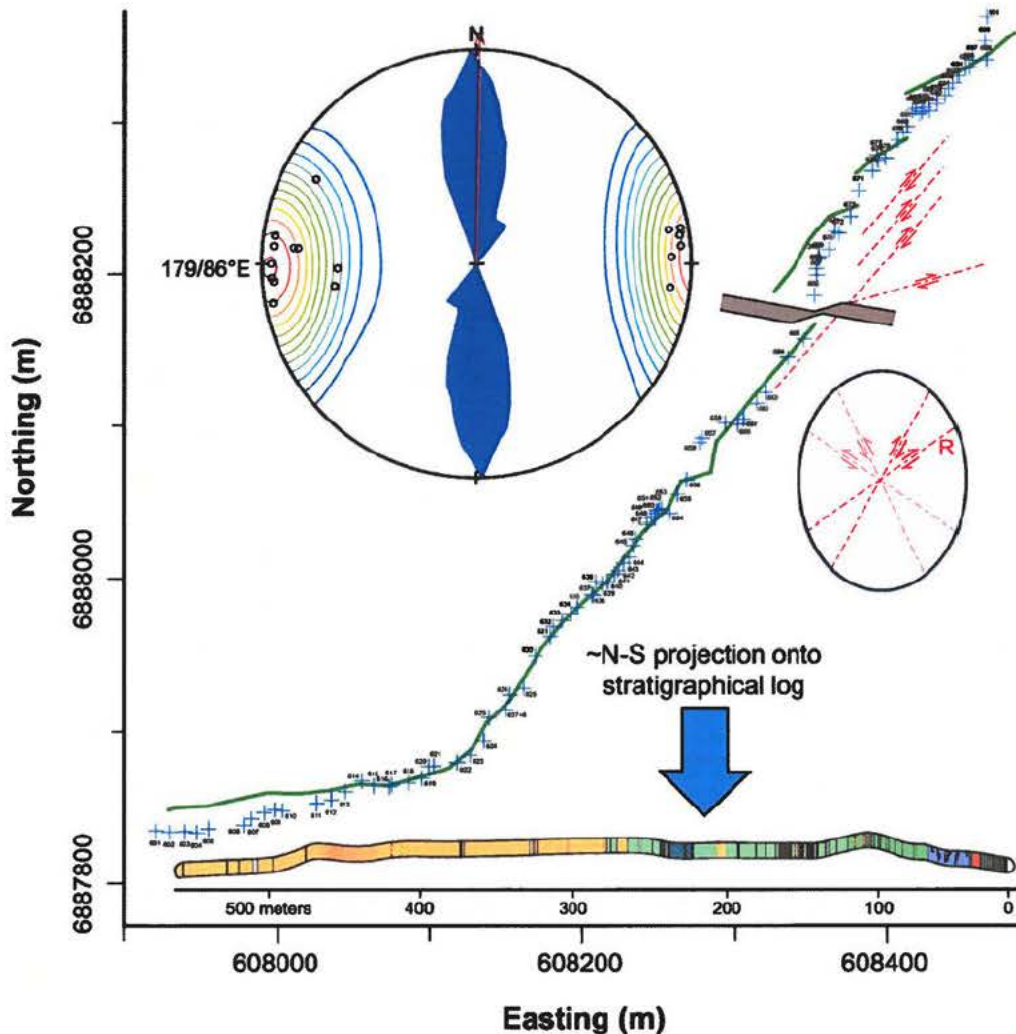


Figure 5: GPS location of 100 samples (blue crosses labelled, from left to right, 601-699 and 901) along a mapped traverse (green lines). Inserted stereographical diagram with Kamb's contoured distribution of 17 poles to sub-vertical foliation/bedding planes suggests a simple N-S projection produces a ~550 m-thick lava-profile (Figure 6) along the Easting-axis; after accommodating one ca. 30 m left-lateral component of fault displacement (red arrows). A simple strain ellipse is added, in order to explain fault displacements. The lower lithological cross section is enlarged in Figure 6 and shown together with a legend.

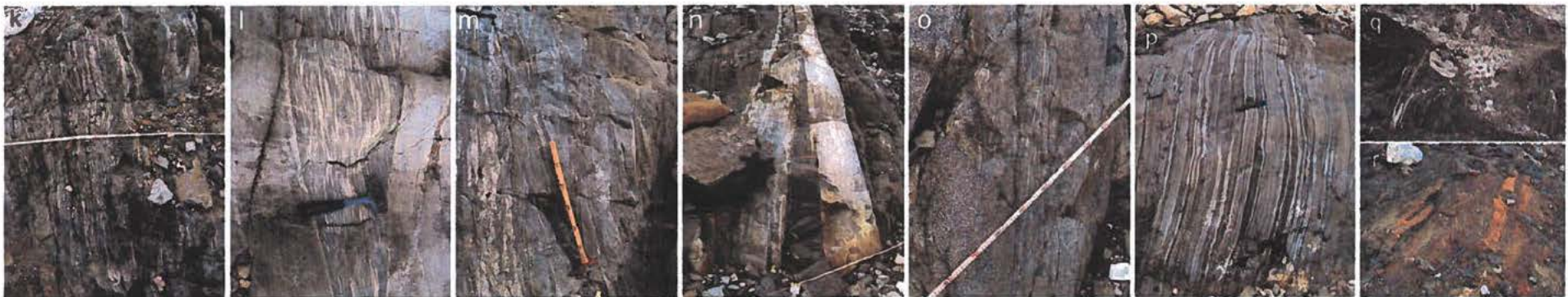
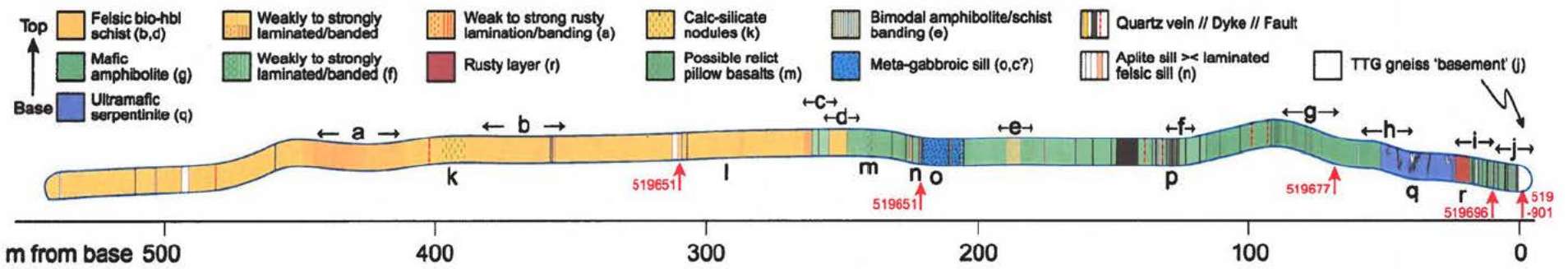
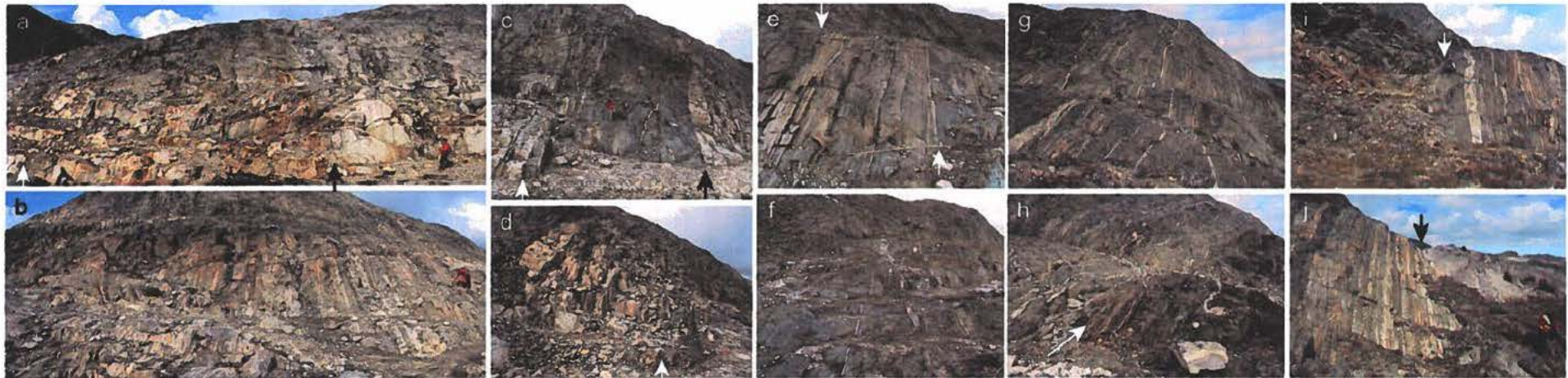
The following list of generally fine grained metamorphic rocks, exposed along the Nigerlikasik section, are tentatively classified on the basis of field observations into four distinctly different major units, which resemble Szilas' (2012) TTG/aplites, ultramafics, amphibolites and leucomphibolites, respectively:

- The foliated *TTG gneisses* were emplaced as either a coarser grained biotite-quartz-plagioclase unit at the 'base' of the older supracrustal sequence of ultramafic-mafic-felsic meta-volcanic rocks, or as syn-tectonic intrusive *aplitic* sheets into the section. These intrusive units will henceforth be referred to as either "TTG" or "aplite sheets", respectively.
- The *ultramafic* supracrustals within the Nigerlikasik section are in most cases better classified as hornblendites ± phlogopite ± diopside ± serpentinite/talc, but will for practical reasons be referred to as either serpentinites, or appropriate meta-volcanic name (e.g., picrite), throughout the remainder of this report. These units generally appear to be more sheared, finer grained, and darker coloured than the dunite along the western margin of the Nigerlikasik supracrustal belt, but do occasionally include small (<1 m) and coarser grained boudins.
- The *mafic* supracrustal rocks in the lower (eastern) part of the log (transect) are generally fine-grained and layered hornblende ± biotite ± plagioclase amphibolites. These mafic units will hereafter be referred to as amphibolites, or appropriate meta-volcanic name (e.g., basalt). Subsequent geochemical classifications are able to subdivide this group into more 'enriched' and 'depleted' units.
- The *felsic* supracrustal rocks in the upper (western) part of the log (transect) are generally fine-grained, layered biotite ± hornblende ± plagioclase ± quartz schists and gneisses. As there are a subordinate number of gneisses, these felsic units will hereafter collectively be referred to as bio-hbl schists, or by their appropriate meta-volcanic name (e.g., andesite). Subsequent geochemical classifications are able to subdivide this group into an underlying (W) andesitic and an overlying (E) dacitic unit.

It is difficult to determine in the field whether the relatively sharp contact between the basal amphibolites and the coarser grained TTG gneiss (*Figure 6j*) is tectonic or intrusive. The basal amphibolites are intruded by a dense swarm of <1 m thick aplitic sheets (<50%). As we will show, these aplite sheets have a similar chemical composition as the TTG gneisses, favouring an intrusive contact for the TTG gneiss protoliths. Such an intrusive contact is also most consistent with the western margin of the supracrustal belt representing the lowermost 'base' of this meta-volcanic sequence, up through which the intrusive aplite sheets decrease in abundance towards the east.

Above the lowermost ~50 m of amphibolites/aplites and a continuous 3-5 m thick rusty layer (*Figure 6r*), we find a ~30 m thick ultramafic unit, which appears to be more variably folded (*Figure 6q*) than the more competent looking amphibolites and bio-hbl schists/gneisses along the same section. The fine grain size suggests that these ultramafic units are volcanic rather than intrusive. Both the lower (*Figure 6i*) as well as the upper (*Figure 6h*) contacts between the amphibolites and the surrounding lithologies are relatively sharp and in some places isoclinally folded (*Figure 6q-r*).

Figure 6 (next pages): Field relationships along the mapped and sampled transect in *Figure 5*, projected N-S onto a ~560 m-long profile. The black/white arrows in photos (a-j) point at important unit boundaries that are mentioned in the text. Details in photos (k-r) are located along the profile. All rock units and particular features along the schematic cross section are briefly described by the legend but more fully in the text. Note that this cross section, in a vertical position with the western end as the base and the eastern end as the top, is the equivalent to the stratigraphical log added to subsequent *Figures 12-13* and *15-16*, and modified further in *Figures 22* and *26*. Labelled red arrows locate aplite sheets and TTG 'basement' samples used for the U-Pb geochronology (*Figure 7*).



Disregarding the intrusive felsic sheets, which appear to decrease rapidly in volume up through the lower part of the section, the amphibolites appear to be more massive the first ~100 m above the contact to the TTG gneiss (cf., profile scale in *Figure 6*). Above 100 m, the amphibolites possess a more banded texture (*Figure 6e* and *p*) that continues another ~150 m up towards the contact to an upper bio-hbl schist sequence. Banded amphibolites dominate this part of the section and they are only interrupted by a declining number of minor (<1 m thick) aplite sheets (*Figure 6n*), and one spotted meta-gabbroic unit (<15 m thick; *Figure 6o*) with < 1cm large amphiboles. A similar, coarse grained meta-gabbro crops out in roughly the same stratigraphical position along the western limb of this supracrustal belt's tight synform in *Figure 2*, into what appears to be only moderately deformed pillow structures within the amphibolites. The amphibolite sequence therefore appears to be made up of both intrusive and extrusive igneous protoliths; based on interpretation of the best preserved igneous textures, the bulk part of the rocks represent lava flows that appear as relatively fine-grained, massive to banded amphibolites. The origin of the so-called banded amphibolites remains speculative and could reflect tectonically thinned lava beds of either rhythmically varying compositions, internal flow zones of more massive centres and more amygdaloidal-rich tops, and/or massive lavas with inter-bedded pyroclastic material.

The upward transition from underlying amphibolites to overlying bio-hbl schists is sharp, but appears to contain one sequence of mutually inter-bedded amphibolites/ bio-hbl schist units (*Figure 6c-d*), which could reflect either (1) contemporary bimodal volcanism, (2) intrusion of a bio-hbl schist protolith into a basaltic lava protolith, or (3) repetition through very tight isoclinal folding. The same uncertainty applies to other <1 m thick and banded bio-hbl schists within the amphibolites (*Figure 6n*), which could be interpreted in the field as representing either inter-bedded extrusive flows or intrusive sheets. It will be argued in the geochemistry section, that lower inter-bedded bio-hbl schists probably represent intrusive felsic sheets, as part of an igneous plumbing system that may have fed the overlying extrusive rocks. Thus, the actual compositional change in the original lava stratigraphy occurs at 261 m along this section, and only one isolated amphibolite layer (<1 m thick) – amongst several aplitic sheets – crops out above this major transition.

Like the amphibolites, the bio-hbl schists can be subdivided into more or less massive to finer layered varieties (*Figure 6a-b*). Unlike the amphibolites, most of these layers are lenticular and in some places *fiamme* textured (*Figure 6l*), typical for classical ignimbrites. Such '*fiammes*' could however, also in many cases represent clasts that were stretched tectonically within pyroclastic flows. Nonetheless, these observations all indicate that relict igneous textures have survived the deformation and that the other finer grained and massive-layered bio-hbl schist units with high degree of certainty also are volcanic. More than halfway through the meta-volcanic bio-hbl schists sequence, at ~395 m along the section, a ~10 m thick unit with several, boudinaged, and <10 cm thick dark greenish bands (*Figure 6k*) appears in an otherwise monotonous sequence. Slightly farther up section, the bio-hbl schists are rusty stained for ~40 m (*Figure 6a*), before becoming even paler and slightly less banded throughout the uppermost part of the section. The upper schists are only cut by relatively few aplite sheets.

Geochronology

Pre-concentrates of zircons and other heavy minerals were prepared on a Wilfley® shaking table. Jaw-crushed rock material was grinded for c. 6 s in a WC swing mill and sieved to < 500 µm grain size before loaded onto the shaking table. Individual zircon grains were hand-

picked from the heavy mineral fractions under a microscope and mounted onto double-sided sticky tape. The mounted zircons were set in a 2.5 cm diameter circular epoxy mount that was ground to expose the mid-section of the zircons, before polishing to one micron grade. The polished zircons were imaged using back-scattered electrons (BSE) employing a Philips XL40 Scanning Electron Microscope in order to characterise internal morphology of individual grains (e.g., inclusions, inherited cores, metamorphic growth zones), and to select areas suitable for U/Pb analysis. Prior to analysis the sample mounts were vigorously cleaned using Propanol-2 to remove surface Pb contamination.

The age data were acquired using Laser Ablation Sector Field – Inductively Coupled Plasma Mass Spectrometry (LA-SF-ICPMS, Frei and Gerdes, 2009). The method uses a focused laser to ablate minute quantities of a sample contained in an air-tight sample chamber. The laser ablation system used is a NewWave Research/MerchanteK UP213 equipped with a frequency quintupled Nd-YAG laser emitting at a wavelength of 213 nm. The laser was operated at a repetition rate of 10 Hz and nominal energy output of 45 %, corresponding to a laser fluency of 3.5 J cm⁻². All data were acquired with a single spot analysis on individual zircon grains with a beam diameter of 30 µm. Samples and standards were held in low volume sample cell and helium was used as flushing gas, and mixed downstream with argon before entering the mass spectrometer. For the spot diameter of 30 µm and ablation times of 30 s the amount of ablated material approximates ca 200-300 ng.

The ablated material was analysed on an Element2 (ThermoFinnigan, Bremen) single-collector, double focussing, magnetic sector ICPMS with a fast field regulator for increased scanning speed. The total acquisition time for each analysis was 60 s, with the first 30 s used to measure the gas blank. The sample washout time for this configuration was 7 s after which the baseline level was reached without spiking, however, in practice washout time was set to 30 s. The isotope data were corrected for interference of the Hg from the Ar gas on the Pb-204 peak by monitoring the Hg-202 peak. A mass bias correction was carried out for all unknowns based on the deviation of the primary (bracketing) standards from the true values. The accuracy and precision of the data were assessed from repeated analysis of the Plešovice zircon standard. During data acquisition the Plešovice gave an average of 339.3 ± 0.7 Ma as obtained from ²³⁸U/²⁰⁶Pb ages (based on 543 zircons with 24 outliers); in agreement with reported value by ID-TIMS of 338 ± 1 Ma (Aftalion et al. , 1989).

Plotting of concordia diagrams and calculation of ages and their associated uncertainties from either weighted means or from unmixing of multiple age components were done in an off-line Excel sheet using Isoplot/Ex version 3.22 (Ludwig, 2003). All uncertainties are reported at the 2σ level or 95% confidence interval.

Four aplitic sheets sampled at 10, 70, 220 and 310 m above the basis of the supracrustal section yield fairly consistent ages of (1) 2929 ± 5, (2) 2931 ± 4 (3) 2913 ± 5 and (4) 2922 ± 5 Ma, respectively (*Figure 7a-d*). These ages are interpreted as the intrusive ages for the aplite sheets, based on the uniform individual age patterns as well as the zoned zircons that clearly resemble magmatic rather than metamorphic textures (right-hand panel of *Figure 7*). In comparison, a TTG sample taken at 4 m below the basal contact gives two less well constrained ages of 2903 ± 4 and 2845 ± 7 Ma (*Figure 7e*), which we interpret as the intrusion age of the gneiss protoliths and the timing of the metamorphic overprint, respectively. Technically the ages were derived using the “unmix” function of the Isoplot software. Zircon grains in the TTG sample resembles those in the aplites with frequent oscillatory zonation, however, with a relatively larger fraction of grains showing textural evidence for metamorphic overprinting.

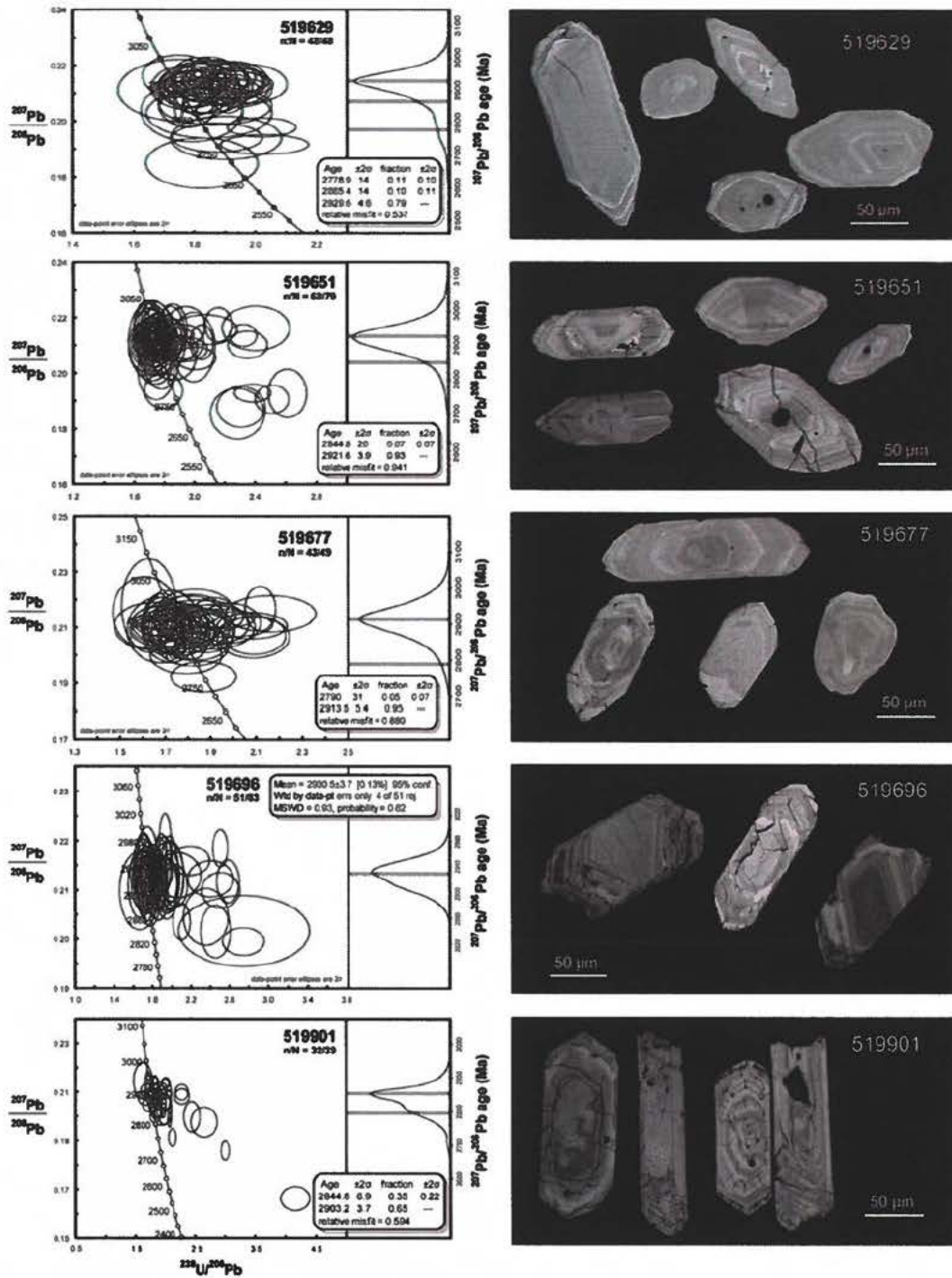


Figure 7: Geochronological results for four aplitic sheets (519629, 519651, 519677 and 519696) and a sample of TTG gneiss from the base of the profile (519901). The U/Pb data are displayed in combined Tera-Wasserburg diagrams (error ellipses being at the 2σ level) and probability-density-distribution plots scaled on the secondary y-axes. Back-scattered electron images of typical zircons from the samples are shown on the right-hand panel. Zircons generally display distinct oscillatory zonations reflecting likely magmatic origins.

Based on the above, it would appear that the aplites are slightly older than the igneous emplacement age of the local TTG gneiss protolith. However, TTG samples dated in the area do show general overlap with the aplite ages, with the nearest example being a TTG sample just south of Kvanefjord (only 12 km south of the sampled profile) which gives an age of 2915 ± 5 Ma (Kokfelt et al. unpublished data). A general overlap between aplite intrusion ages and the regional TTG protoliths formation does therefore exist, suggesting a likely spatial and temporal relation between the two in the area.

Collectively, the five reported ages provide a minimum age of the supracrustal section of ~ 2930 Ma. These age constraints are also generally consistent with the regional understanding of the temporal relationship between the supracrustal belts being earlier and always intruded by later TTG-type intrusions (Szilas 2012, Szilas et al. 2011a, b, 2012a, b).

Structural overprint

At least two regional folding events affected the Nigerlikasik supracrustal sequence, its hosted aplitic sheets, at least one early generation of possibly associated quartz veins, and the surrounding TTG-gneisses (Escher 1971). The first regional scale folding is mimicked by smaller scaled deformations, which all occurred during amphibolite facies conditions. This is typically evidenced by tight to isoclinal folds with steep, and roughly north-south striking axial planes (e.g., *Figure 8a-b*), which affected all supracrustal rock types to variable degrees. Units with contrasting rheological properties reacted differently to this early E-W directed compression, with more competent layers within the amphibolites and felsic intrusive aplites becoming boudinaged within fold limbs (*Figure 8a-b*) and obliquely cross-cutting quartz veins becoming parasitically folded (*Figure 8d*).

In contrast to the rheologically more competent mafic units, the ultramafic units appear much more deformed, with aplitic veins being tightly folded (*Figure 8a-b*). As aplitic sheets in unhydrated ultramafic rocks would normally represent the weaker unit, it is suspected that the ultramafic units were partially serpentised before the folding event took place, because serpentine is more easily deformed by crystal plastic deformation mechanisms (e.g. Escartin et al. 2001, 2008) than olivine (e.g., Evans et al. 1990, Kohlstedt et al. 1995).

Less intense deformation of the amphibolites was for most parts ductile, with a major part of the shortening accommodated by folding, but some brittle displacements along small scale faults or shear zones also took place (e.g., *Figure 8c*). However, occasional faulting along axial fold planes also suggest that either the temperature was just too low for completely ductile shearing of these mafic rocks or the strain rate of the crustal shortening was too high. This is a typical shortening mode of more mafic (i.e. quartz and mica-poor) crust, where shearing associated with grain-size reduction and recrystallisation of the same minerals (i.e., biotite \pm hornblende \pm plagioclase) suggest that the deformation happened under amphibolite-facies condition (*Figure 8e*).

The felsic bio-hbl schists and gneisses appear to have deformed differently than other units, probably because their much higher abundances of biotite and quartz deform more easily through crystal plastic deformation mechanisms. Thus, the foliations of bio-hbl schists and gneisses tend to have become aligned with fold axial planes of isoclinal folds, which are often very difficult to recognise. In some cases, the only evidence of such folding is the occurrence of ptygmatically folded quartz-veins in the schists (*Figure 8d*). To form the ptygmatic folds in *Figure 8(d)*, more oblique and competent quartz-veins must have buckled ductily above (middle-) greenschist facies conditions, yet within a much weaker bio-hbl

schist (e.g. Tullis and Yund 1977). It is therefore likely that this deformation occurred at amphibolite facies conditions.

The overall structure of the supracrustal belt is a large synform, with felsic schists in the core of the fold, and smaller pods of ultramafic rock near the contact to the surrounding orthogneiss (*Figure 2*). The overall wavelength of these first-order folds is ca. 2-3 kilometres, whereas parasitic folds of cm to several tens of meters occur within all rock units, making estimates of original stratigraphical thicknesses difficult. This main folding event, with nearly vertical and north-south striking fold axial planes is locally buckled by a folding event with a nearly east-west trending and steeply dipping fold axial plane. The latter folding event has a large wavelength of tens of kilometres that is most easily recognized as curved trends of supracrustal belts and variations in the dip of their mapped fold axes on geological maps. The large scale buckling has hardly any effect in terms of displacement on the scale of observations made along the 550 m-long section across a fold limb that is roughly parallel to its fold axis.

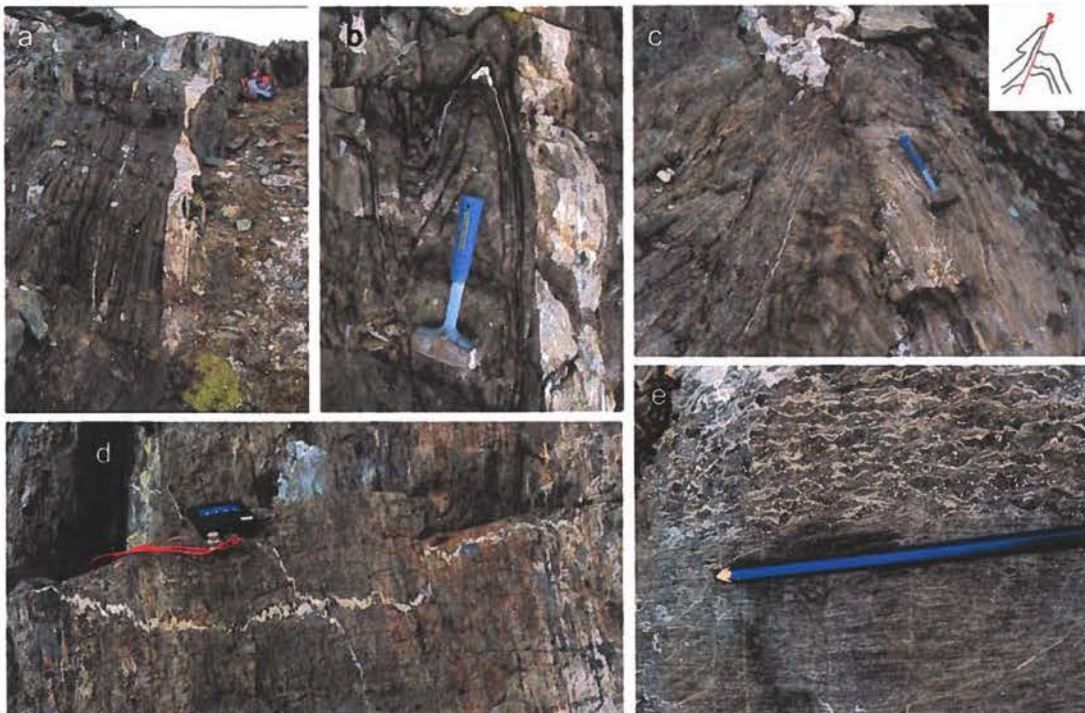


Figure 8: a-b) Tightly-folded serpentinised ultramafic rock with boudinaged folded aplitic sheets and quartz veins. Both images facing north. c) Shearing-folding in amphibolites. Semi-brittle folding under amphibolite-facies conditions causes faulting semi-parallel to the axial plane of the fold. A minor offset of the foliation along the fold can be observed. Quartz veins outline the fault plane. Facing north. d) Ptygmatic folding of the quartz veins in the felsic schist dominated part of the section. The quartz-vein was orientated at a high angle to the current foliation. Due to compressional deformation the quartz-vein shows hundreds of cm-scale folds, while the felsic schist was flattened during the same deformation event. Facing north. e) Deformation induced grain size reduction of amphibolite rock reproduced the same minerals as the regional metamorphism, suggesting deformation to have proceeded under amphibolite facies conditions. The pencil points towards the south.

The later folding that locally overprints the isoclinal/tight folding event might be more locally associated with fault induced compression. A major dextral component of brittle and steeply dipping strike-slip faulting and shearing occurred under greenschist facies conditions (e.g., epidote, quartz and a second phase of serpentinization within the ultramafic

unit), when rock foliations were dragged into brittle fault zones (e.g., *Figure 8c*). A large N-S trending valley defines the westernmost end of the sampled section and it is uncertain whether or not this also marks a major fault zone. It does not visibly offset the 10 m thick MD3 dyke by any large amount but roughly parallels the axial plane of the tight regional synform. It may be that the core of the fold – and thereby the stratigraphically highest part of the section – lies even further west of where the sampled section ends. The exact amount of missing stratigraphy is difficult to precisely assess, due to the tight folding and likely vertical displacement along such a N-S fault, but it is assumed to be minor. Likewise, other parts of the sampled stratigraphy may have been upset by post-volcanic deformations, to which the serpentinites may have been most susceptible.

Apart from some faulting associated with the main folding of the amphibolites (described above), the serpentinitized ultramafic rocks also seem to have faulted roughly parallel to its nearly vertical and N-S striking foliation, apparently displacing its eastern block left-laterally, towards the north. The exact timing of this displacement is unknown, and could have occurred during either (1) the latter stages of the main folding and shearing event, (2) the superimposed buckling event, or (3) during an even later, separate event. As the shearing is associated with some flattening of pre-existing structures, the deformation may have occurred at intermediate to high temperatures (up to amphibolite-facies) conditions. Slickensides on these 30°-dipping E-W fault planes reveal a minor thrust component, which is consistent with regional top-to-N back thrusts in Kolb's (2011) fold-and-thrust belt model for the region.

Several brittle fault/dyke episodes occurred after the main foliation-forming folding event, but possibly still within a regional E-W compressive setting (cf., strain ellipse in *Figure 5*). The first generation consists of ENE-WSW striking and sub-vertical strike-slip faults, which were right-laterally displaced at (upper) green schist-facies conditions (e.g., epidote-quartz-serpentine within the ultramafic units). The foliation is dragged into the fault zone but also associated with some brittle fracturing of the amphibolites. The central part of the Nigerlikasik sample section follows the northern side of one of these 064°-striking faults, whereas the western part of the profile was sampled along one of its 078°-striking Riedel faults (*Figure 5*). The amount of dextral displacement along this fault section appears to vary either due to differential internal compression or vertical N-block-down component.

An 8-m thick and roughly WNW-ESE trending mafic dyke cuts through the sample section and the SW-NE trending dextral fault zone (*Figure 5*). The dyke is left-laterally offset for ~16 m along the dextral reidel fault (note the opposite senses of shear) and, even if the dyke intersection is not visible along the (partly) talus covered fault zone, propagating dykes are known to utilize favourably orientated, pre-existing weaknesses such as fault planes. This interpretation is also consistent with WNW-ESE trending MD3 dykes cutting SW-NE trending MD2 dykes (~2130±65 Ma; Kalsbeek and Taylor 1985, Nilsson et al. 2010) and associated fault zones in other parts of the region, and thereby imparts a minimum age on the SW-NE trending dextral fault activity during (upper) greenschist facies conditions. A second generation of strike-slip faults run roughly parallel to the steep, N-S trending main foliation, and appear to left-laterally offset the ENE-WSW striking strike-slip faults by up to 30 m. The regional implications of this section's structural details are discussed in further detail by Keulen et al. (2011).

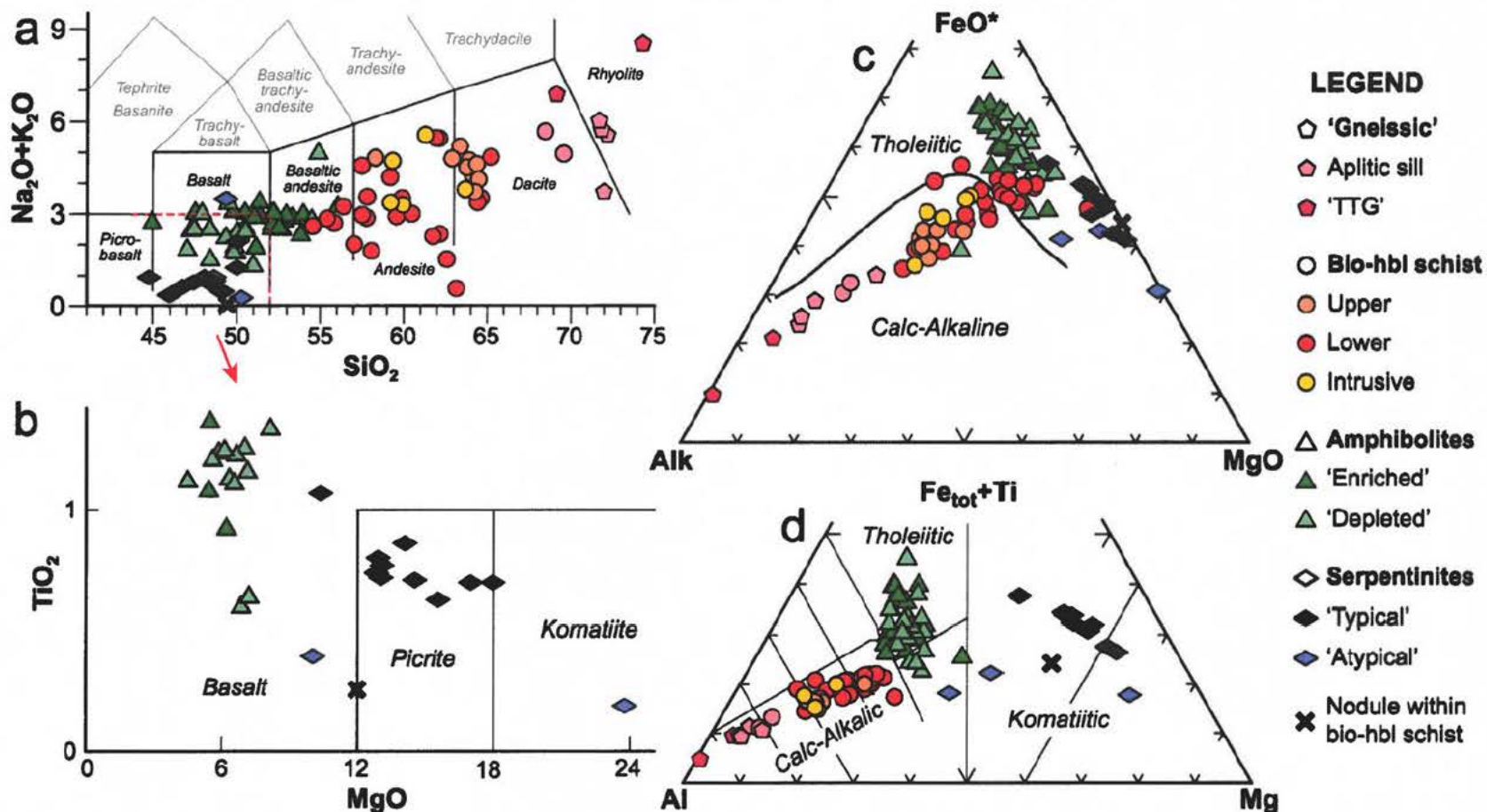


Figure 9: Major element classification diagrams: a) Total Alkali-Silica (TAS) diagram for the classification of volcanic rocks (Le Bas et al. 1989); b) further MgO-discrimination between basalts, picrites and komatiites (Le Maitre 2002) amongst samples from dashed red area in (a); c) alkali-iron-magnesium (AFM) diagram for further subdivision of sub-alkaline igneous rocks into either calc-alkaline or tholeiitic series (Irvine and Baragar 1971); d) alternative discrimination between calc-alkalic, tholeiitic and komatiitic igneous rocks (Jensen 1976). Different rock units are given different symbol shapes and colours, whereas sub-units within these are given slightly different colours. Subdivisions amongst the ultramafic (serpentinite) to mafic (amphibolite) units are based on geochemical differences, made apparent further into this section. Presumed intrusive bio-hbl schists are hosted with the amphibolites, whereas overlying lower and upper bio-hbl schists are both stratigraphically and geochemically different.

Igneous protolith classification

A total of 99 rock samples were collected from the nearly ~550 m-long Nigerlikasik section/log, including 4 basal amphibolites, 12 high-Mg serpentinites from a ~30 m thick zone, another 34 samples up through ~170 m of massive-banded amphibolites, and 35 bio-hbl schists and gneisses from the upper (western) ~300 m of the section/log. Of the remaining 14 samples, one sample was collected from a dark green nodule within the bio-hbl schist/gneiss zone (at ~400 m), two samples were collected from the metagabbroic intrusion with variably sheared relict pyroxene phenocrysts (*Figures 6o and 7e*), three felsic bands from within the amphibolites were sampled, as well as six aplitic sheets from across the lower two thirds of the section/log and two TTG samples from just below its base. All samples were processed and analysed at the Central Analytical facility (University of Stellenbosch; Appendices 2-3).

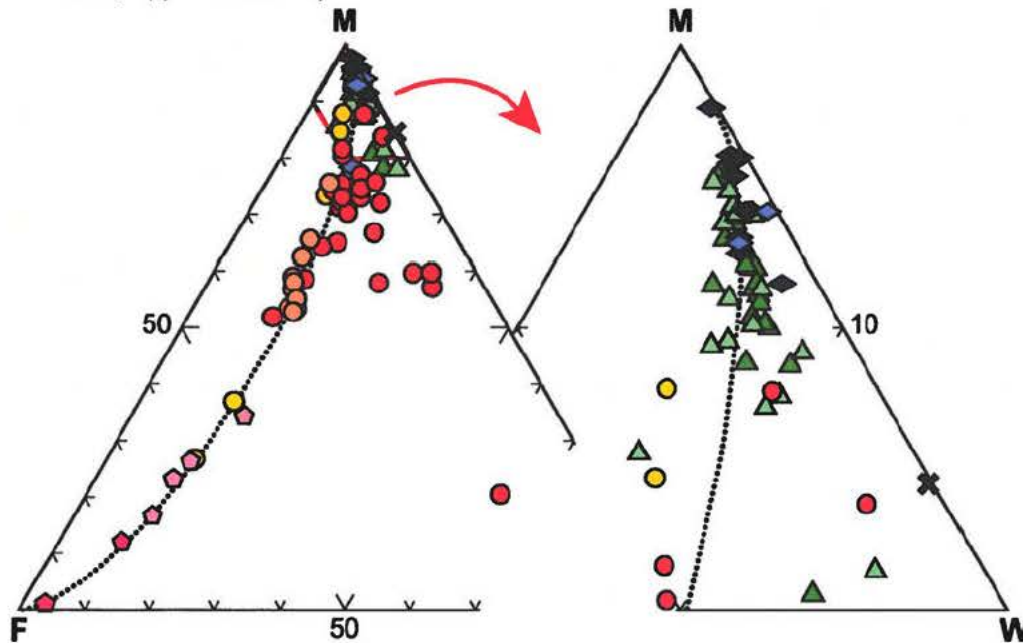


Figure 10: Statistical empirical Weathering Index for igneous rocks, as defined by Ohta and Arai (2007). Note that most samples cluster along the 'unweathered' igneous trend (dotted line), whereas one sample within Ohta and Arai's (2007) 'soil facies 4', and approximately 15 intermediately weathered 'facies 2' samples (all of which primarily are lower bio-hbl schists and amphibolites) extend towards the weathered (W) corner of the ternary diagram. Diagram to the right is an enlargement of the mafic (M) corner of the left diagram. $M = -0.395 \times \ln(\text{SiO}_2) + 0.206 \times \ln(\text{TiO}_2) - 0.316 \times \ln(\text{Al}_2\text{O}_3) + 0.160 \times \ln(\text{Fe}_2\text{O}_3) + 0.246 \times \ln(\text{MgO}) + 0.368 \times \ln(\text{CaO}^*) + 0.073 \times \ln(\text{Na}_2\text{O}) - 0.342 \times \ln(\text{K}_2\text{O}) + 2.266$; $F = 0.191 \times \ln(\text{SiO}_2) - 0.397 \times \ln(\text{TiO}_2) + 0.020 \times \ln(\text{Al}_2\text{O}_3) - 0.375 \times \ln(\text{Fe}_2\text{O}_3) - 0.243 \times \ln(\text{MgO}) + 0.079 \times \ln(\text{CaO}^*) + 0.392 \times \ln(\text{Na}_2\text{O}) + 0.333 \times \ln(\text{K}_2\text{O}) - 0.892$; $W = 0.203 \times \ln(\text{SiO}_2) + 0.191 \times \ln(\text{TiO}_2) + 0.296 \times \ln(\text{Al}_2\text{O}_3) + 0.215 \times \ln(\text{Fe}_2\text{O}_3) - 0.002 \times \ln(\text{MgO}) - 0.448 \times \ln(\text{CaO}^*) - 0.464 \times \ln(\text{Na}_2\text{O}) + 0.008 \times \ln(\text{K}_2\text{O}) - 1.374$. Symbols as in Figure 9.

The Total Alkali-Silica (TAS) diagram (*Figure 9a*) shows that all samples could belong to roughly the same sub-alkaline series, with only minor paucity in SiO_2 contents between (1) more *andesitic* lower bio-hbl schists, (2) more *dacitic* upper bio-hbl schists, and (3) *rhyodacitic* TTG and aplitic veins. There is a small overlap between some amphibolites and

bio-hbl schists within the basaltic andesite field of *Figure 9(a)*, which may reflect compositional heterogeneity within such old, metamorphosed and deformed rocks. Some intrusive felsic sheets (not aplites, *sensu stricto*) within the amphibolites have compositions similar to – and could thereby be feeders to – either the lower or upper bio-hbl schists. It appears that bio-hbl schists from the upper part of the section are more dacitic than underlying bio-hbl schists, whereas only TTG and aplitic sheets are rhyodacitic. It also appears that some ‘enriched’ amphibolites – which will later be shown to have, e.g., more *enriched* rare earth element (REE) patterns ($La_N/Yb_N > 1$) – are also slightly more SiO_2 -rich andesitic basalts compared to ‘enriched’ amphibolites/basalts with, e.g., more LREE-depleted signatures (*Figure 22*).

Some andesitic bio-hbl schists show anomalously low values of what probably reflect leaching of mobile alkalis. This is supported by these samples having the highest Weathering Index as defined by Ohta and Arai (2007, W in *Figure 10*), whereas remarkably many of the other samples do not show any evidence of significant weathering. Thus, the consistently low alkalis for most serpentinite samples are presumably a pristine magmatic feature, whereas three ‘atypical’ serpentinites may have been alkali enriched; due to either contamination or fluid mobilization. A further classification on the basis of MgO (*Figure 9b*) shows that most serpentinites represent picritic protoliths and only one ‘atypical’ serpentinite is a komatiite with >18 wt% MgO.

A subdivision of subalkaline igneous rocks in an AFM-diagram reveals that most amphibolites and serpentinites lie on a tholeiitic trend pointing towards an Fe-enrichment, whereas most bio-hbl schists lie on a calc-alkaline trend characterised by no Fe-enrichment (*Figure 9c*). It is evident from this plot that the tholeiitic amphibolites and the calc-alkaline bio-hbl schists are petrogenetically unrelated through crystal fractionation. The serpentinites also define a slightly separate tholeiitic trend, suggesting that the three main petrological/magmatic rock groups along this meta-volcanic section evolved independently.

A subdivision into three different magmatic series becomes even more evident in *Figure 9(d)*, where the relatively low- Al_2O_3 serpentinites/meta-picrites define a *komatiitic* trend that is more clearly separated from the *tholeiitic* amphibolites, as well as the *calc-alkaline* bio-hbl schists, TTG’s and aplitic veins. The rhyodacitic TTG, and geochemically similar aplitic veins, are distinctly more ‘evolved’ than the andesitic-dacitic bio-hbl schists, defining two separate clusters along a common calc-alkaline trend.

Multi-elemental statistical analysis

Correspondence analysis is a very useful multi-elemental (or multivariate) statistical assistance (Clausen 1998) to traditional geochemical analysis of any data sets. Such elaborate data analysis allows one to (1) assess the extent to which samples are more or less similar in terms of their overall elemental budgets, (2) identify elements that behave similarly, and (3) estimate the importance of certain element groups in relation to variations among sample groups. When the statistical results are plotted as in *Figure 11*, it becomes much like analysing other bivariate plots, with the exception that all elements are taken into consideration at the same time. Thus, the strength of such a statistical approach is to enhance the general patterns in a data set, thereby providing more confident constraints on the relative importance of different elements. In return, some details in the data may be reduced or lost during this exercise.

The two most significant principal statistical components are recorded along factor axes 1 and 2 (F1 and F2 in *Figure 11*), respectively. These results indicate that most com-

positional variation along the F1-axis is controlled by differences between incompatible and compatible elements (this is typically the case for most igneous data sets), and thereby separate the serpentinites, amphibolites and more felsic units into three arrays that radiate from a common centre close to the diagram's origin. Coincidences with certain elements indicate that (1) serpentinites are richer in compatible elements (Cr, Ni, Mg and Co), (2) amphibolites are richer in transitional metals (Fe, Mn, Cu, Sc, V and Ti) and heavy rare earth elements (HREE), whereas (3) schists are richer in the traditionally more incompatible large ionic lithophile (LIL) and most high field strength (HFS) elements (especially U and Th), except the HREE.

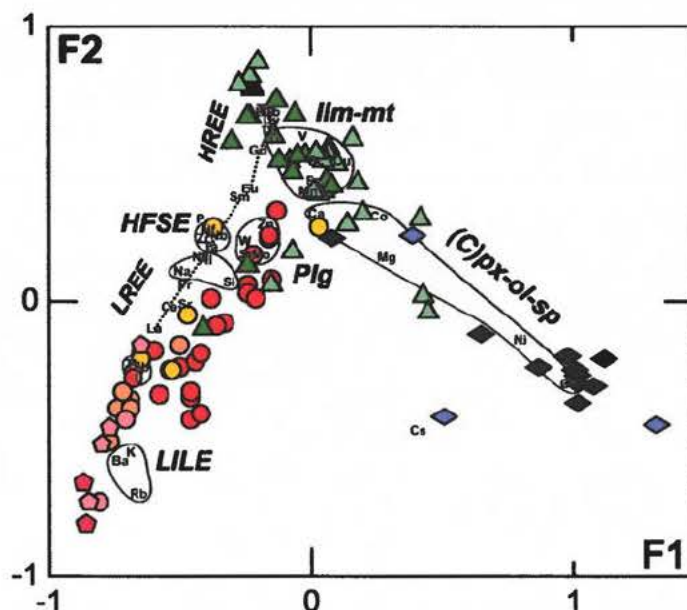


Figure 11: Factor 1 and 2 (F1 and F2) values resulting from a correspondence analysis on a two-way contingency table consisting of 99 samples and 46 elements (major oxide wt% and trace element ppm). 53.70% and 23.24% of inertia, or variations, from this multivariate principal component analysis is expressed as differences along the F1 and F2 axis, respectively. See Clausen (1998) for simple explanations on this statistical method. LILE = Large Ionic Lithophile Elements. LREE and HREE = Light and Heavy Rare Earth Elements, respectively. HFSE = High Field Strength Elements. Plg = plagioclase. Ilm-mt = ilmenite-magnetite. (C)px-ol-sp = (clino)pyroxene-olivine-spinel. Symbols as in Figure 9.

Most of the more depleted and basaltic amphibolites have higher F1-values (Figure 11) than the more enriched amphibolites, consistent with a typical tholeiitic differentiation trend. One could argue that most serpentinites lie on the same trend, either as ultramafic parental melts or as cumulates, but that does not necessarily mean that they are petrogenetically related to the amphibolites. Some amphibolites overlap an oblique trend defined by lower bio-hbl schists, and these samples are marked as possibly mixed.

Most of the bio-hbl schists in the upper (western) part of the Nigerlikasik section define a more evolved trend, together with the rhyodacitic TTG and aplitic sheets that are slightly offset from most of the lower bio-hbl schists. This indicates that the upper bio-hbl schists are geochemically more similar to these rhyodacitic intrusions than the lower bio-hbl schists. It is evident that LILE (Rb-Ba-K), in unison, become more enriched during the 'evolution' of felsic samples than Th-U-Pb and the HFSE (Zr-Hf-Nb-Ta-P), respectively. This behaviour is also indicated by the lighter REE becoming systematically more enriched

within more evolved bio-hbl schists than the heavier REE. Remaining elements cluster into an albite group (Si-Al-Na-Sr) and a base metal group (Sn-Mo-W-Zn). From such correspondence analysis results it is now easier to relate these groups to the behaviour of selected elements in the following traditional diagrams for geochemical descriptions and analyses. *Figure 10* suggests that very little of this variation is the result of weathering.

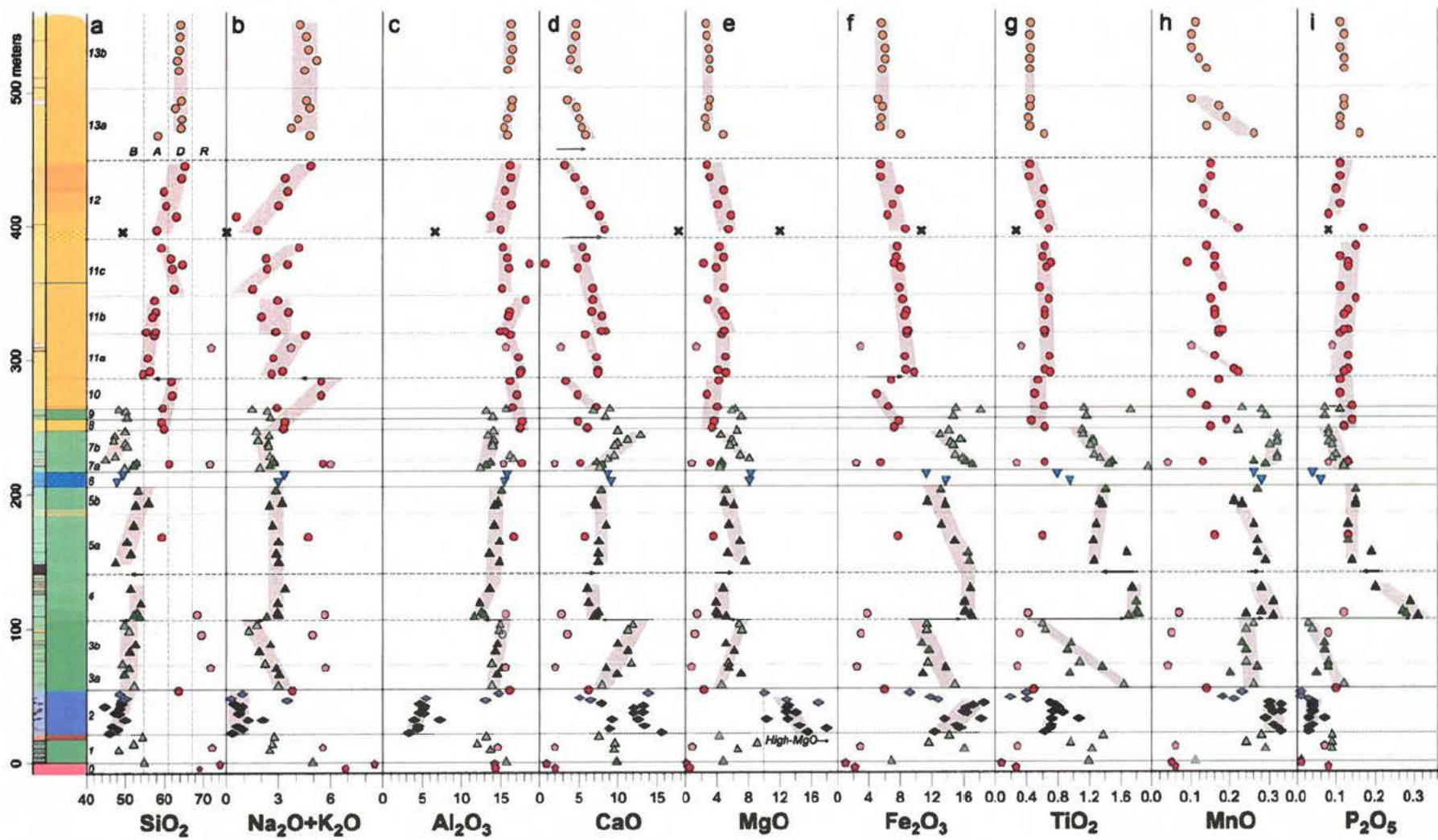
Stratigraphic variations

Stratigraphic variations in major elements (*Figure 12*) confirm an overall geochemical change from east to west through the supracrustal sequence in *Figure 6*, from the TTG 'base' and up through a relict pile of picrites, *tholeiitic* basalts-basaltic andesites and *calc-alkaline* andesites-dacites, respectively (cf., SiO₂). With increasing stratigraphic height there are also overall corresponding decreases in CaO, MgO, MnO, Fe₂O₃ and TiO₂ contents. Geochemical shifts between these three major groups are in some cases abrupt, in accordance with the fact that each group was derived from a unique primary melt and not derived from an underlying group through simple crystal fractionation (e.g., *Figure 9c-d*). Dashed stratigraphical subdivisions between sample sequences of consistent major element variations within both the calc-alkaline bio-hbl schists and the tholeiitic amphibolites, on the other hand, may delineate six(-nine) sub-units within each of these groups. Some of these sub-units may, however, have been arbitrarily split by intrusive units, such as the gabbroic unit #6 and the inter-bedded bio-hbl schist unit #8.

The serpentinites seem to make up a single unit, up through which MgO (and possibly CaO) systematically decreases, whereas SiO₂, Al₂O₃, Fe₂O₃, TiO₂ and P₂O₅ increase. If this fine grained unit is a picritic lava pile, then these geochemical variations up through it are consistent with the progressive tapping from a sub-volcanic magma chamber that underwent fractionation of Mg-rich olivine, Cr-spinel and/or pyroxene. Based on a single sample, the ultramafic boudins within the bio-hbl schists appear to have higher CaO, P₂O₅ and lower Fe₂O₃ and TiO₂ than the serpentinites in unit #2.

The amphibolites may be composed of the following four cyclic units, separated by more abrupt geochemical resets: (1) CaO, Al₂O₃ and MgO increases gradually up through the massive grey amphibolites in unit #3, whereas total alkalis, Fe₂O₃, TiO₂ and P₂O₅ all decrease. Abrupt geochemical changes occur between the massive-banded amphibolite units #3 and #4 (cf., horizontal arrows in *Figure 12*), shifting towards higher SiO₂, total alkalis, Fe₂O₃, TiO₂, MnO and P₂O₅, as well as lower Al₂O₃, CaO and MgO. (2) Most major element concentrations remain relatively constant up through the lower part of the banded amphibolites (unit #4), at the top of which there is another, less abrupt, shift towards more MgO and less SiO₂, TiO₂ and P₂O₅. (3) SiO₂ and TiO₂ increases, whereas MgO, Fe₂O₃ and MnO decrease up through unit #5, on top of which there is a third geochemical shift across the meta-gabbroic intrusion (unit #6). (4) Finally, SiO₂, Al₂O₃ and CaO increase, whereas MgO, Fe₂O₃, TiO₂ and P₂O₅ all decrease up through the uppermost part of the banded amphibolites (unit #7).

Figure 12 (next page): Major element variations from east to west through the section in *Figures 5 and 6*, assuming the easternmost serpentinites to be the base of this supracrustal ultramafic-mafic-felsic sequence. Grey backgrounds emphasize possible trends across possible cyclic units, numbered between the log and the chemical plots. B = Basalts to basaltic andesites. A = Andesites. D = Dacites. R = Rhyolites. Lithological log as in *Figure 6*, with minor veins and intrusions separated to the left. Symbols as in *Figure 9*.



Overall – and provided that the Nigerlikasik log is orientated the right way up – it may be generalized that the amphibolites most consistently exhibit cyclic increases in SiO_2 , Al_2O_3 and CaO , whereas Fe_2O_3 , MgO , TiO_2 and P_2O_5 tend to decrease, in between more abrupt partial resets. Such variation could simply be explained by the fractionation of (Fe,Mg)-silicates, (Fe,Ti)-oxides and apatite within a sub-volcanic magma chamber, which after each differentiation cycle is replenished by more undifferentiated (Mg+Al+Ca rich and Fe+Ti+P poor) partial mantle melts. It is, on the other hand, also possible to argue that the inconsistent geochemical variation up through the amphibolite units reflect (1) syn-eruptive replenishments of more Mg-rich melts up through the enriched tholeiite unit #3, (2) an equilibrium transition of both replenishment and fractionation up through the enriched tholeiite units #4-5, followed by (3) eruptions during 'normal' tholeiitic differentiation up through the depleted tholeiite unit #6. However, other processes, such as magma mixing, probably also need to be considered, in order to explain all of the geochemical variations.

Geochemical variations up through the bio-hbl schists tend to be more consistent and rhythmic than up through the amphibolites. Many cyclic units tend to exhibit upward increasing to constant SiO_2 , total alkalis (and to a lesser extent P_2O_5), whereas CaO (and to a lesser extent Fe_2O_3 , TiO_2 , and MgO) tend to decrease. Systematic decreases in CaO (and roughly parallel increases in alkalis) are particularly sensitive in identifying up to six, more or less rhythmic differentiation cycles. Al_2O_3 predominantly increases up through most cycles and thereby suggest that clinopyroxene or amphibole was fractionating, whereas plagioclase or garnet could also be involved whenever there is a parallel decrease in both Al_2O_3 and CaO (sub-units #11a+c). Fe_2O_3 and TiO_2 do not conform as well to the six cycles inferred from CaO , but generally exhibit sub-trends that more often are consistent with an occasional and additional fractionation of ilmenite. Thus, the major element variation up through the Nigerlikasik section suggests that the calc-alkaline andesitic-dacitic suite could have erupted from a cyclically replenished magma chamber where plagioclase/garnet, clinopyroxene/amphibole and ilmenite fractionated. Both the overall and cyclic upward changes toward more 'evolved' calc-alkaline compositions argue against any eruptions from a compositionally stratified magma chamber (e.g., Hildreth 1981).

Apart from an abrupt shift towards higher CaO concentrations, the major element concentrations in the upper bio-hbl schists in unit #13 appear to be relatively constant continuations of the most 'evolved' lower bio-hbl schists in the uppermost part of unit #12. The relatively constant major and minor element trends through the upper bio-hbl schists may be inferred to have been maintained up through any missing parts of the stratigraphy, and thereby represent the most 'evolved' volcanics in the sequence – yet not as 'evolved' as the rhyolitic aplites and TTG's.

The stratigraphic variations are in *Figures 13 and 15-16* shown for a selection of nine trace elements, including at least one element from each of the six trace elemental clusters that were identified and outlined in *Figure 12*.

Of the three compatible metals (*Figure 13*), Cr is readily incorporated – together with Ni and to a lesser extent Co – into the earliest fractionating spinel, olivine and pyroxene crystals, respectively. Both Cr and Ni are relatively high in most of the picritic samples (up to 800 ppm Ni, not shown), reaching values typical for primary mantle melts. Especially, one sub-group of picrites with c. 600-800 ppm Ni may be regarded as having been either primary mantle melts or lavas with accumulated olivine. It is also noted that the Mg-rich boudin within the lower bio-hbl schists has too low Ni and Cr to be regarded as a picrite. As indicated by relatively low Cr-contents for our most quartz-rich TTG's (12-13 ppm Cr), it seems implausible that samples were seriously contaminated during steel milling by either Cr or Ni (cf., Appendix Table 2b), least significantly of all the softer and Cr+Ni rich picrites.

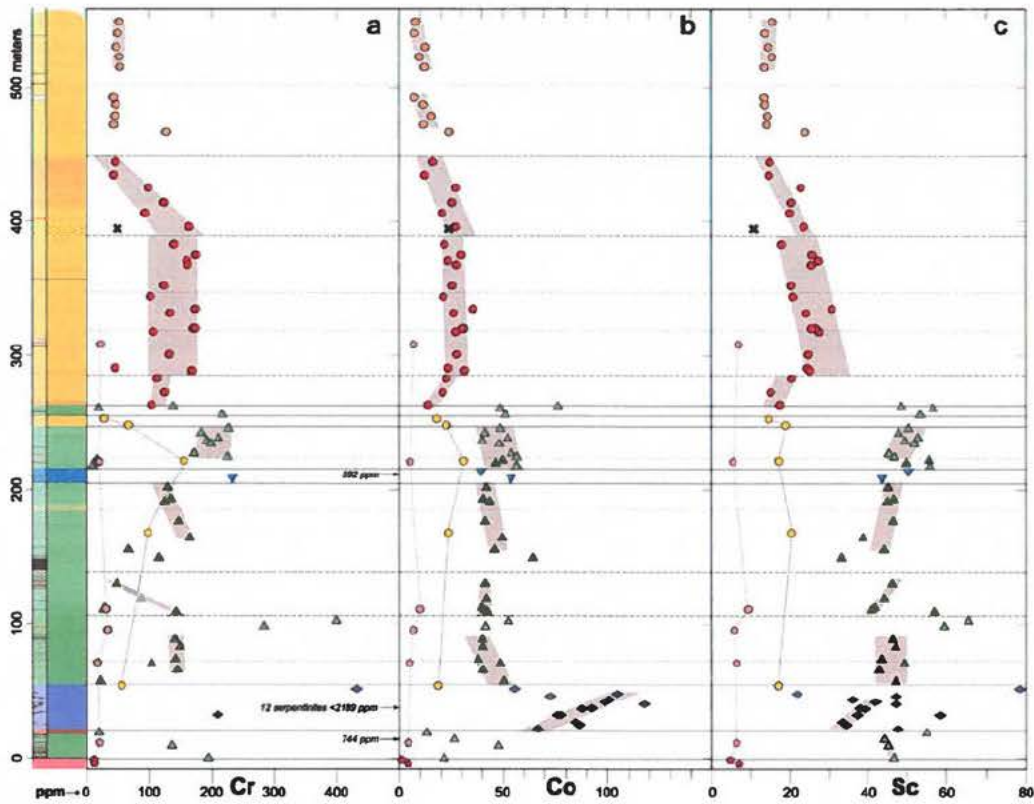


Figure 13: Stratigraphic variations in the more compatible metals Cr, Co and Sc. Grey background trends and stratigraphical subdivisions as in Figure 12. Tie lines connect intrusive bio-hbl schist and aplite sheets, respectively. Lithological log as in Figure 6, with minor veins and intrusions separated to the left. Symbols as in Figure 9.

Most other samples have Cr-contents below 250 ppm (and <200 ppm Ni) – reflecting that these magmas have experienced olivine + spinel fractionation – with the possibility of 3 amphibolite samples with >400 ppm Cr having been more contaminated by the milling. The lower bio-hbl schists do, however, still have relatively high Cr, which on the basis of the above discussion are believed to be true values.

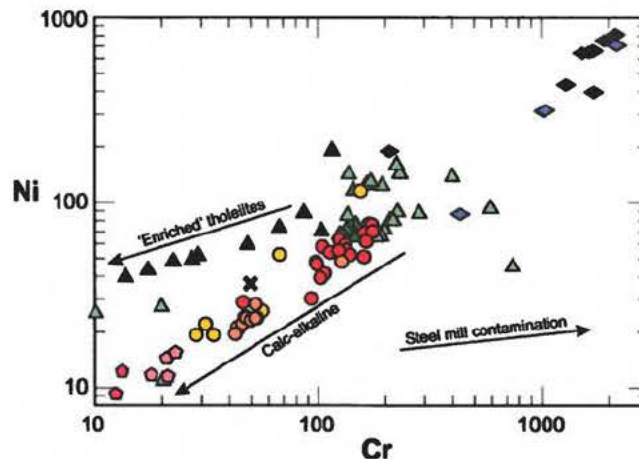


Figure 14: Log Cr versus log Ni plot for all Nigerlikasik samples, showing two different, but merging, trends for some 'Enriched' tholeiites and the entire calc-alkaline suite.

Our interpretation that the stratigraphical Cr-variations reflect pristine compositions is strengthened by two different trends in *Figure 14*, both of which would not be expected if the high Cr contents of the lower bio-hbl schists were due to steel mill contamination. With the exception of (1) decreasing Cr up through the amphibolites, below the metagabbro, and (2) the upper part of the lower bio-hbl schists (above the ultramafic boudins), the stratigraphical variation in MgO, Cr and Ni do not, however, show as clear a correlation as would be expected from olivine + spinel fractionation.

Increasing Co and decreasing MgO up through the ultramafic unit suggests that $D_{Co} < 1$ for its fractionating assemblage, becoming more compatible higher in the sequence. There is also a clearer separation between serpentinites (~60-120 ppm Co), amphibolites (~35-60 ppm Co), lower bio-hbl schists and associated felsic sheets (~15-30 ppm Co) and upper bio-hbl schists and rhyodacitic intrusions (<20 ppm Co), which is not observed for either Cr or Sc. This is consistent with amphibole and/or ilmenite fractionation within calc-alkaline andesite-dacite suite.

Sc behaves incompatibly up through both the serpentines and amphibolites (> 30 ppm), but then becomes markedly lower (< 30 ppm) and starts behaving more compatibly halfway up through the lower bio-hbl schists. This is consistent with clinopyroxene, amphibole and/or garnet fractionation within this suite. The intrusive bio-hbl schists have Sc concentrations within the range of the extrusive bio-hbl schists (~15-25 ppm), whereas rhyodacitic intrusions have concentrations (<10 ppm) below that of upper bio-hbl schists.

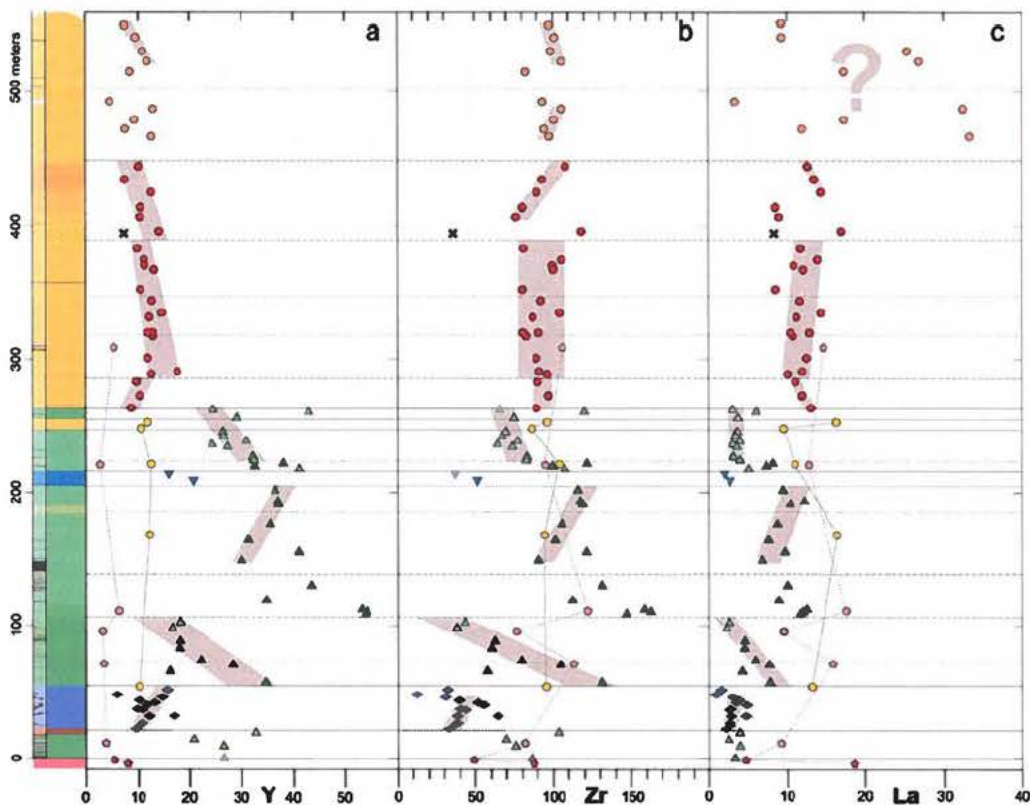


Figure 15: Stratigraphical variations in the more incompatible HFS elements Y, Zr and La. Grey background trends and stratigraphical subdivisions as in Figure 12. Tie lines connect intrusive bio-hbl schist and aplite sheets, respectively. Lithological log as in Figure 6, with minor veins and intrusions separated to the left. Symbols as in Figure 9.

Of the three selected elements within the range of incompatible trace elements in *Figure 15*, it can be deduced from *Figure 11* that Y behaves as a HREE (Ho), Zr as a MREE, whereas La is a LREE. As can be further deduced from *Figure 11*, HREEs act more incompatible within the tholeiitic (ultra)mafic suite, as reflected by lower and decreasing Y through the bio-hbl schists (*Figure 15a*), whereas LREEs are more incompatible in the calc-alkaline felsic suite, as reflected by somewhat higher and increasing La up through the bio-hbl schists (*Figure 15c*). Within the tholeiitic suite, however, all incompatible HFSEs mirror the trend of MgO, and thereby confirming a control by the differentiation and/or replenishment cycles in *Figure 12(e)*. Y (and other HREEs), on the other hand, conforms more to CaO's differentiation cycles amongst the bio-hbl schists (*Figure 12d*) and is thereby consistent with garnet fractionation. It is also noted that HFSE concentrations in likely intrusive bio-hbl schists all lie within the range of the presumed extrusive counterparts, whereas most rhyodacitic intrusions register the lowest HREE-concentrations.

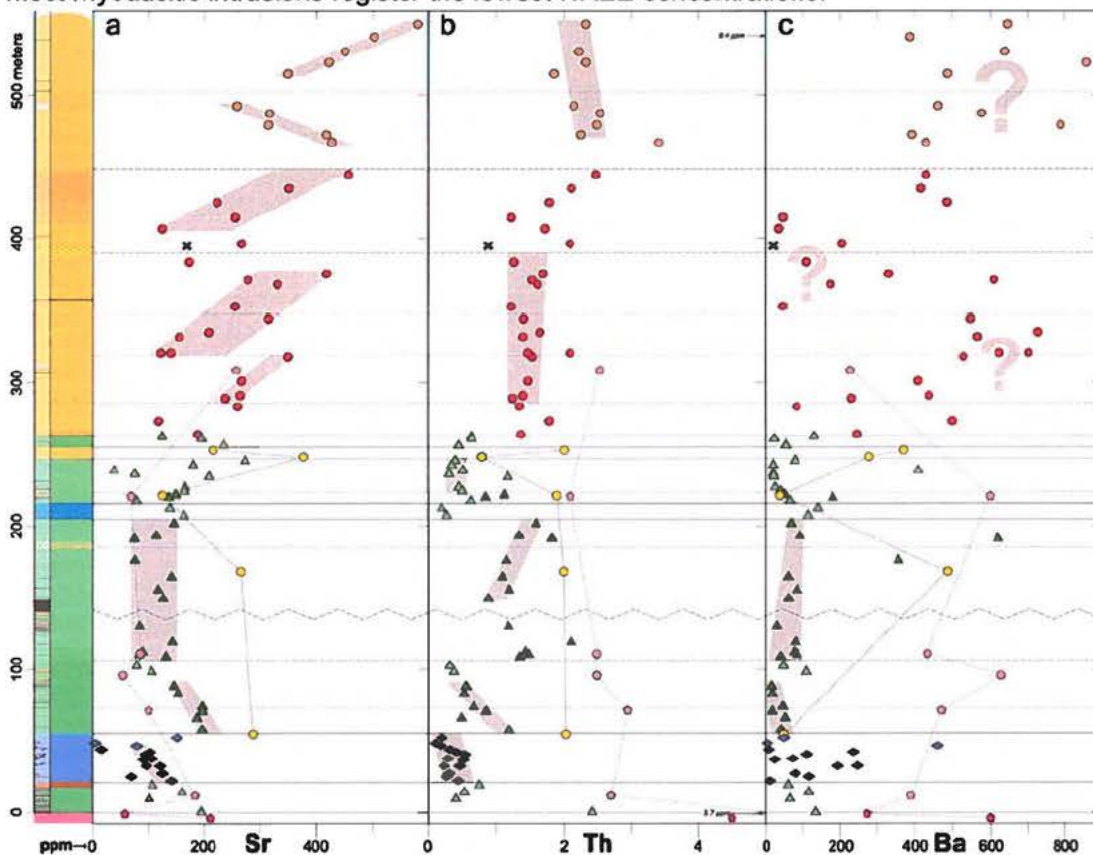


Figure 16: Stratigraphical variations in the most incompatible LIL elements Sr, Th and Ba. Grey background trends and stratigraphical subdivisions as in *Figure 12*. Tie lines connect intrusive bio-hbl schist and aplite sheets, respectively. Lithological log as in *Figure 6*, with minor veins and intrusions separated to the left. Symbols as in *Figure 9*.

In *Figure 16(a)*, Sr decreases in two cycles up through the picrites and the overlying massive amphibolites, but there is only a weak correlation with CaO (and not Al_2O_3) to support the fractionation of plagioclase up through the picrites. Sr remains chaotically constant up through the banded amphibolites, without any clear correlation with either CaO or Al_2O_3 to support any plagioclase fractionation. Some weak cyclic Sr-increases are, furthermore, opposite to the better defined cyclic decreases in CaO up through the lower bio-hbl schists,

suggesting that some other processes than plagioclase fractionation controlled Sr-concentrations. Up through the upper bio-hbl schists, there is first a Sr-decline that is mimicked by CaO (but not Al₂O₃), but this is then followed by a rapid increase to the log's highest concentrations of nearly 500 ppm Sr. It is also noted that concentrations of Sr in the rhyodacitic intrusions (sheets) are generally lower than that of the upper bio-hbl schists, and most other bio-hbl schists in general.

Th (as well as U and Pb) increases more systematically up through the sequence, with the intrusive bio-hbl schists having similar Th concentrations as the lower bio-hbl schists, and the rhyodacitic intrusions matching the Th enrichment observed in the upper bio-hbl schists (*Figure 16b*). These elements thereby exclusively behave incompatibly.

Even if LREEs are more enriched within the bio-hbl schists than HREEs, increases in, e.g., La (*Figure 15c*) starts to become relatively chaotic in upper parts of the sequence. A similar tendency is recorded by the most incompatible LILE (e.g., Ba in *Figure 16c*), yet without any distinct positive correlation between either LREE or LILEs (not shown). Such an irregular variation is remarkable, considering the uniform major element variations in *Figure 12* and small Weathering Index in *Figure 10*, but may, nevertheless, tentatively be attributed to post-magmatic disturbance by fluids and/or later metamorphic remobilization.

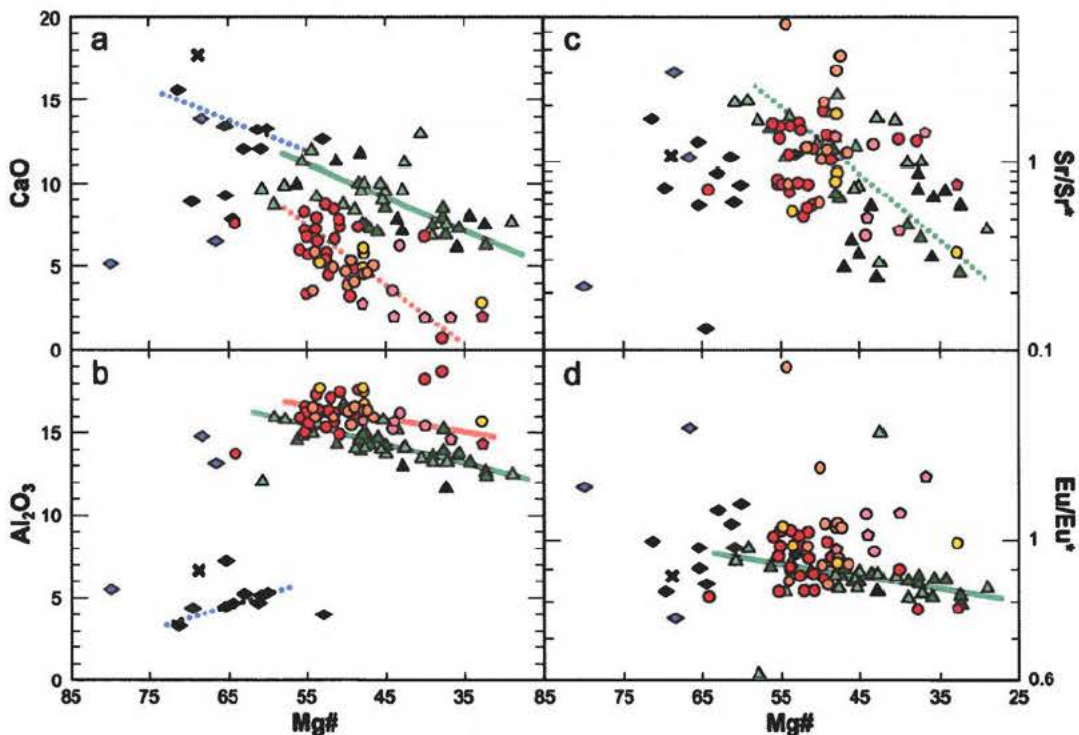


Figure 17: Using Mg# [=100×Mg/(Mg+Fe)] as a differentiation index for more mafic amphibolites and serpentinites. The y-axis values in (c) and (d) express pyrolite and chondrite normalized Sr- and Eu-anomalies, respectively [$Sr/Sr^* = (Sr/19.9) / \sqrt{((Pr/0.254) \times (Nd/1.25))}$]; $Eu/Eu^* = (Eu/0.0563) / \sqrt{((Gd/0.199) \times (Sm/0.148))}$]. Symbols as in *Figure 9*.

Possible fractionating phases

Decreasing Mg# against the only two other major oxides that behave compatibly (i.e., CaO and Al₂O₃ in *Figure 17a-b*) are all consistent with the fractionation of (Mg,Fe)-silicates and plagioclase, during the differentiation of the amphibolites. This is supported by increasingly

more negative Sr and Eu anomalies (Figure 17c-d), which are both typically produced through their partitioning into fractionating plagioclase. Note that the calc-alkaline suite does not exhibit similar systematic changes in these anomalies, however, even if CaO and Al₂O₃ decreases in Figures 17-19 are consistent with plagioclase fractionation.

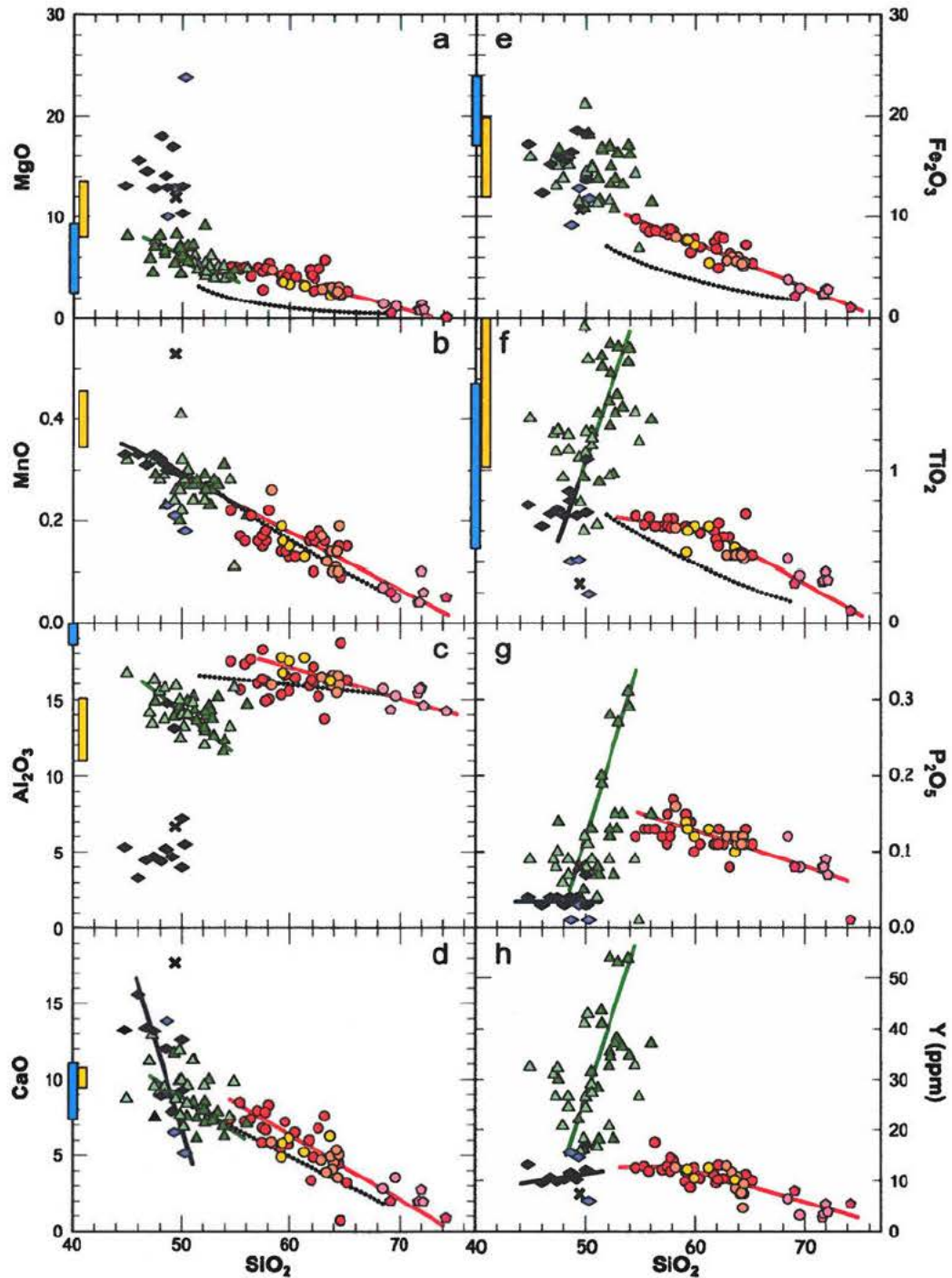


Figure 18: Harker diagrams with systematic negative trends for calc-alkaline andesites, dacites and rhyolites. Purple, green and red lines are manually fitted trends through the picritic, tholeiitic and calc-alkaline suites, respectively. Blue and yellow boxes indicate garnet and amphibole phenocryst ranges from Alonso-Perez et al's (2009) high-P experiments, with coexisting glasses along dotted lines. Symbols as in Figure 9.

The many disconnected trends within *Figure 18* emphasize that the calc-alkaline bio-hbl schists, the tholeiitic amphibolites and the picrites are not related through fractional crystallization. Possible model explanations for this juxtaposition of three distinctly different igneous suites will be discussed later. For now, using SiO_2 as a differentiation index, we just note that the tholeiitic amphibolites exhibit much more marked increases in HFSE (e.g., TiO_2 , P_2O_5 and Y in *Figure 18*) compared to the calc-alkaline suite, which indicate a 2-3 fold enrichment factor. In contrast, the calc-alkaline bio-hbl schists, aplites and TTGs (*Figure 18*) show systematic decreases for all major and minor oxides, except the alkalis. As illustrated by Y in *Figure 18(h)* and exemplified in *Figure 15*, it is mainly HREEs that decrease with increasing SiO_2 . As the Y-decrease coincides with the fractionation of a Ca-rich phase (cf., *Figure 12d*), it suggests that a HREE-rich phase may also have been fractionating. It cannot be zircon, because Zr does not decrease sufficiently, and can therefore only be garnet, which also offers an explanation for the synchronic decreases in CaO and Al_2O_3 without the need of plagioclase fractionation.

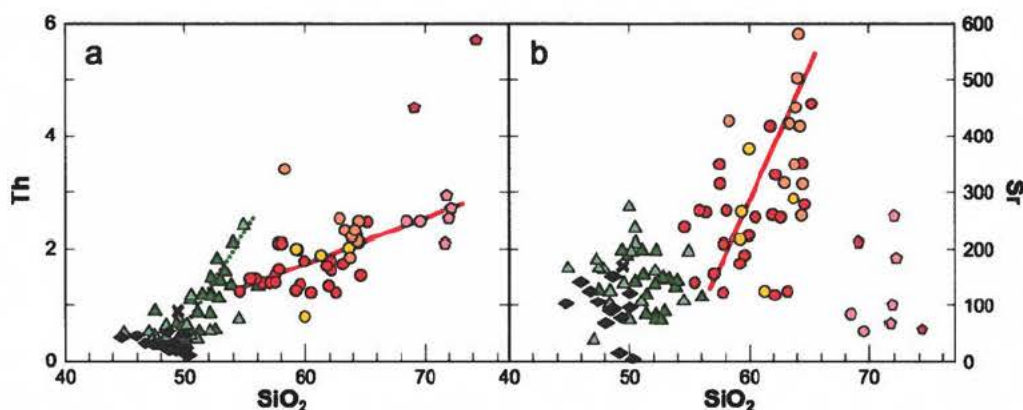


Figure 19: Harker diagrams with systematic positive trends for calc-alkaline andesitic to dacitic bio-hbl schists. Symbols as in *Figure 9*.

Most other incompatible trace elements remain nearly constant, reflecting a bulk partitioning coefficient close to 1, and only U and Th increases two-fold (*Figure 19a*) with increasing SiO_2 through the entire calc-alkaline suite. Sr only behaves incompatibly through the presumed extrusive bio-hbl schists, whereas the intrusive rhyo-dacites have relatively low Sr (*Figure 19b*), confirming that plagioclase never fractionated during the differentiation of the calc-alkaline andesite-dacite suite. The relatively low Sr-concentrations in the intrusive rhyo-dacites are unlike typical TTGs and do suggest that these intrusions did experience some plagioclase fractionation or was derived through the partial melting of a plagioclase-bearing crustal source rock.

Overall, the trends for the calc-alkaline andesite-dacite suite are most consistent with the fractionation of garnet and amphibole, as exemplified by Alonso-Perez et al's (2009) experimental high-P phenocrysts and associated glasses on andesitic starting materials, added to *Figure 18*. This necessitates fractionation within a relatively deep (>30 km) and hydrous sub-crustal magma chamber (Bernstein 1994, Alonso-Perez et al. 2009). In comparison, the ultramafic suite appears to have experienced some olivine, orthopyroxene and spinel fractionation, followed by a more pervasive gabbroic fractionating assemblage for the mafic suite, which both must have occurred within much shallower magma chambers within a younger and thinner island arc crust. Dislocated trends (especially in Al_2O_3) argue against the tholeiitic basalt suite to have been derived from the picritic suite.

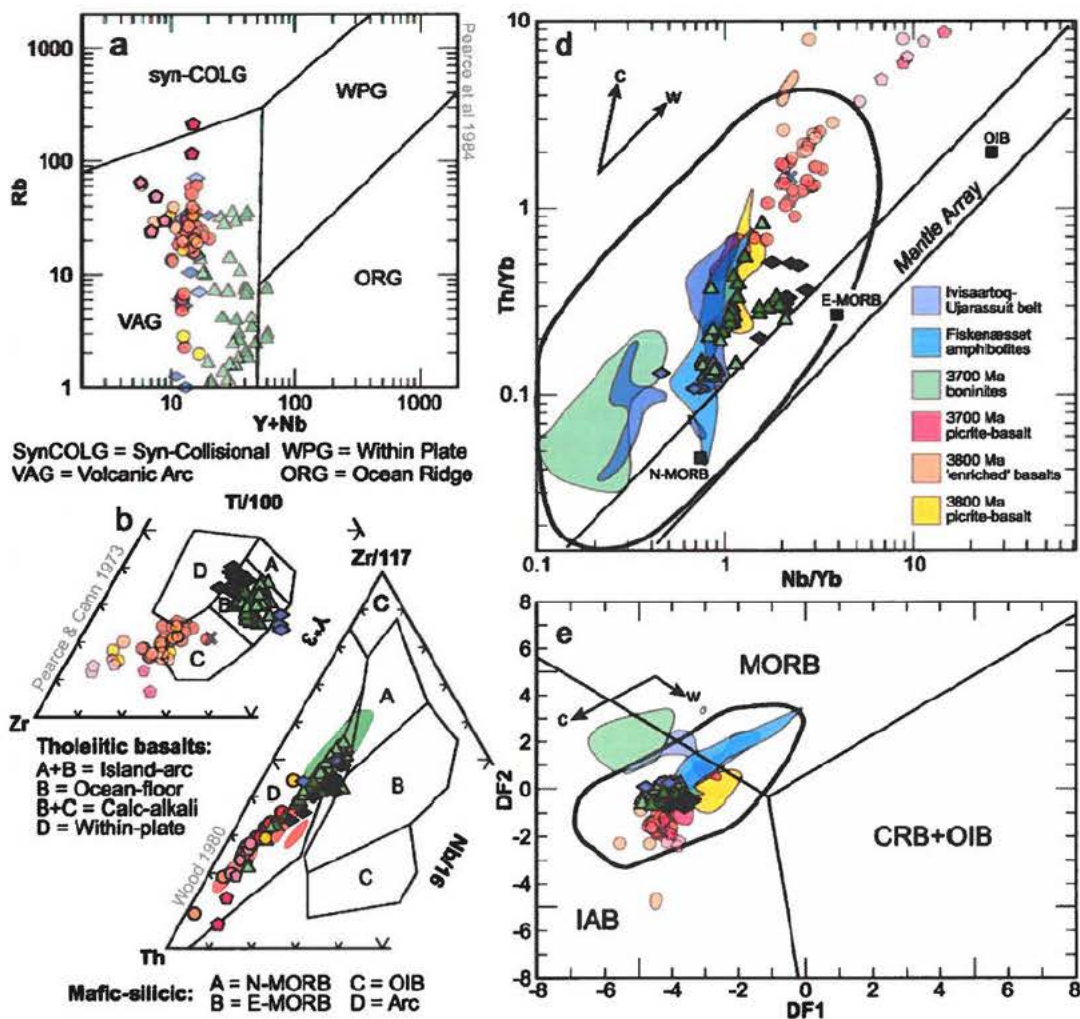


Figure 20: Geochemical discrimination diagrams. (a) Pearce et al.'s (1984) diagram for granitic rocks, where Nigerlikasik's TTGs and aplites are highlighted. (b) Pearce and Cann's (1973) diagram for tholeiitic basalts with $\text{CaO}+\text{MgO} = 12\text{-}20\%$, where Nigerlikasik's tholeiitic suite is highlighted. (c) One of few traditional discrimination diagrams for modern tectono-magmatic settings (Wood 1980) that allows the plotting of mafic to silicic rocks. Most of Nigerlikasik's samples lie within the Arc field, with tholeiitic basalts extending from a transitional MORB field. The extent of Szilas et al.'s (2011a, b, 2012a, b) densest calc-alkaline (orange) and tholeiitic (green) clusters are shown for comparisons. (d) Pearce (2008) 'mantle array' diagram and (e) Agrawal et al. (2008) log-transformed trace element ratio CRB–OIB–MORB tectonomagmatic discrimination diagram, both for basaltic rocks. Coloured fields of older South-West Greenlandic supracrustal belts (Polat et al. 2011) are provided for comparison, as well as their compiled field for > 700 Cenozoic island arc basalts (field bounded by thick black line). IAB = Island Arc Basalts. MORB = Mid-Ocean Ridge Basalts (N- = Normal and E- = Enriched), OIB = Ocean Island basalts, CRB = Continental Rift Basalts. Arrows labelled c (crustal) and w (wedge) indicate geochemical changes due to the enrichment of these components. $DF1 = 0.3518 \times \log(\text{La}/\text{Th}) + 0.6013 \times \log(\text{Sm}/\text{Th}) - 1.3450 \times \log(\text{Yb}/\text{Th}) + 2.1056 \times \log(\text{Nb}/\text{Th}) - 5.4763$. $DF2 = -0.3050 \times \log(\text{La}/\text{Th}) - 1.1801 \times \log(\text{Sm}/\text{Th}) + 1.6189 \times \log(\text{Yb}/\text{Th}) + 1.2260 \times \log(\text{Nb}/\text{Th}) - 0.9944$. Symbols as in Figure 9.

Geochemical discrimination

When resorting to established discrimination diagrams (e.g., Rollinson 1993), it is difficult to single out a diagram that can discriminate between such a diverse suite of meta-igneous rock types as those described here from the Nigerlikasik section; i.e. Archaean serpentinites, amphibolites, bio-hbl schists and rhyodacites. Most discrimination diagrams are customized for either felsic (*Figure 20a*) or mafic (*Figure 20b*) rocks. One exception encompassing mafic to silicic igneous rocks is produced by Wood (1980, *Figure 20c*), in which all Nigerlikasik samples lie on the same trend within the field for island arc rocks, and where the end of the tholeiitic suite touches the transitional MORB field. This variation overlaps the more extensive regional dataset on supracrustal rocks from South-West Greenland (Szilas *et al.* 2011a, b, 2012a, b), where tholeiites extend into the N-MORB field.

Pearce (2008) and Agrawal *et al.* (2008) have proposed alternative tectonomagmatic discrimination diagrams for basaltic rocks (*Figure 20d-e*), and in both of these diagrams the Nigerlikasik rock suite shows geochemical affinity closer to island arc basalt than MORB. Like most of the supracrustal rocks of southern West and South-West Greenland, the rocks from the >2.9 Ga Nigerlikasik section fall within the field defined by Cenozoic island arc basalts or rocks with an inferred crustal or mantle wedge input, and thus it seems likely that they all share a common, presumably island arc related, origin (Polat *et al.* 2011).

Multi-elemental 'spider' diagrams are also useful as a petro-tectonic discrimination tool in that a broader spectrum of elements can be compared for samples and using different normalizing rock types. Thus, amphibolites of the Nigerlikasik profile bear the closest resemblance to typical EMORB by Sun and McDonough (1989), with most of the pattern's incompatible trace elements – except negative Nb and P anomalies and positive Pb-anomalies – normalized to around 1 (not shown). The negative Nb anomalies and positive Pb anomalies are most consistent with these amphibolites having been island arc tholeiites (e.g., Saunders *et al.* 1991), which commonly originate as hydrated mantle-wedge-derived melts in relatively hot (young and/or fast spreading) subduction zones (Baier *et al.* 2008). One way to circumvent these diagnostic island arc anomalies is to suppose that these rocks have been pervasively enriched by mobilized Pb during a later metamorphic stage and that the negative Nb anomalies are an artefact of normalizing to a Phanerozoic MORB composition that in most incompatible elements except Nb (Moyen *pers. comm.*) is considerably more depleted than an Archaean MORB. However, such reasoning is invalidated by the fact that negative Nb-anomalies persist even in chondrite normalised spider diagrams (*Figure 21*). In greater detail, we also find that amphibolites separate into more 'enriched' and 'depleted' subgroups (*Figure 21b, e-f*), where more 'enriched' types exhibit the least erratic spider patterns, including relatively lower Pb, K, Rb and Sr. This suggests that 'depleted' yet LILE-enriched amphibolites are more like island arc basalts than the 'enriched' types, or perhaps more hydrothermally affected.

In the pyrolite normalized spider diagrams (McDonough and Sun 1995), serpentinites (*Figure 21a*) and amphibolites (*Figure 21b*) have overall flat patterns, with distinctly negative P and Nb-Ta anomalies and more elevated LILE, which, as mentioned, characterize island arc basalts. A progression towards more negative Ti anomalies within more elevated incompatible element patterns is also more typical for subduction zone suites experiencing an earlier onset of ilmenite fractionation. In greater detail, we also find that four serpentines are extremely Cs-enriched (36-59 ppm) and may even have weakly negative Zr anomalies that are not as distinct in the amphibolites. Cs is a highly mobile LILE that could locally have been preferentially 'trapped' during the serpentinization of the picrites. Both negative

Zr and P anomalies, which is most distinct for the serpentinites (Figure 21a) and will be discussed later, may be diagnostic for residual majorite garnets in a deep and dry mantle source to primary komatiitic melts (e.g., McCuaig et al. 1994).

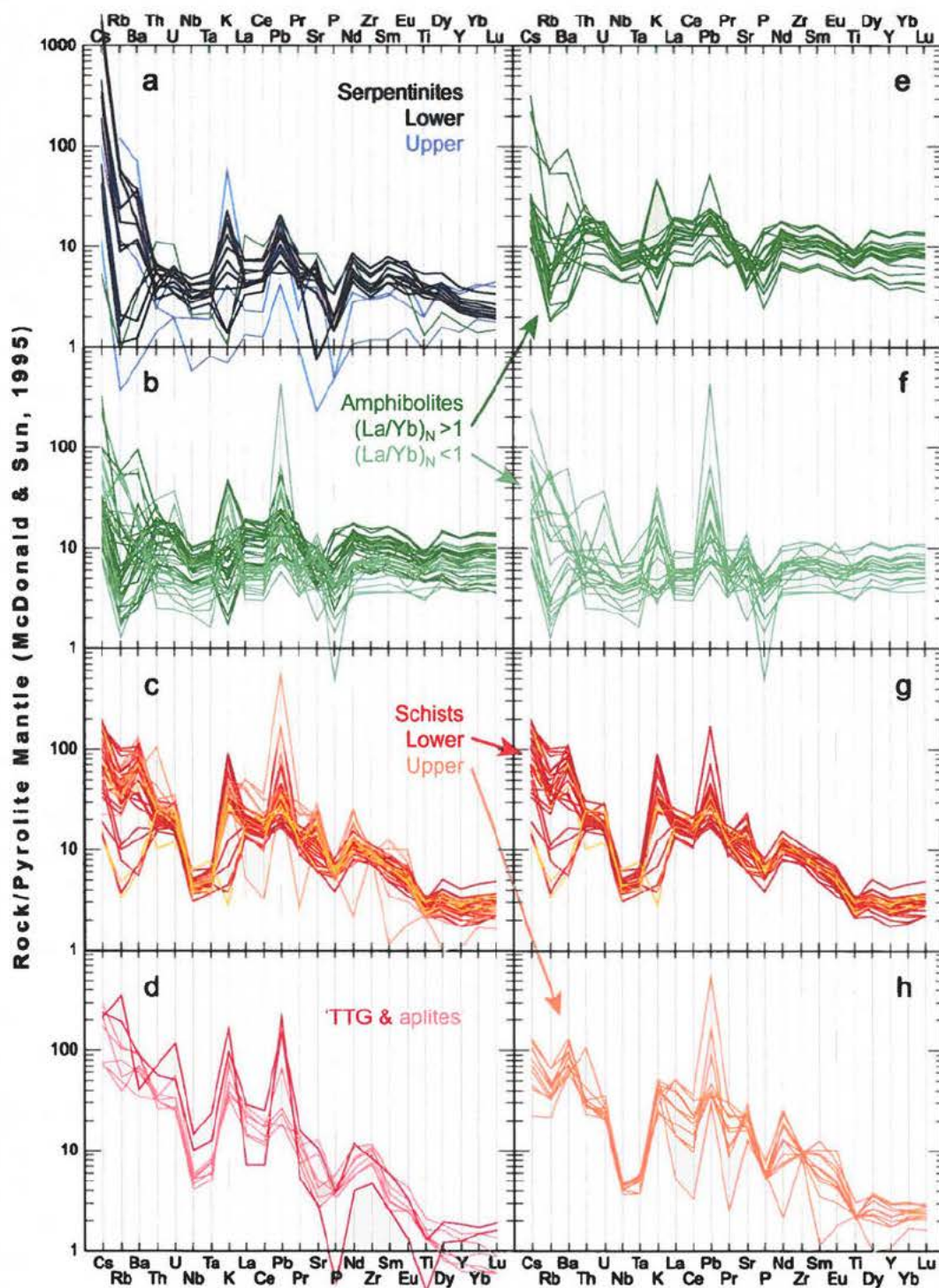


Figure 21. Multi-elemental variation diagrams for (a) serpentinites, (b) amphibolites, (c) bio-hbl schists, and (d) 'TTG/aplites'. The amphibolites are further subdivided into (e) high- $(La/Sm)_N$ and (f) low- $(La/Sm)_N$ types, whereas bio-hbl schists are further subdivided into stratigraphically (g) lower and (h) upper units.

Bio-hbl schists (*Figure 21c*) and rhyodacitic intrusions (*Figure 21d*) have steeper overall patterns (lower HREE), even more negative Nb-Ta anomalies and much more positive Pb-spikes than the serpentinites and amphibolites, in addition to negative Ti anomalies that are consistent with the ilmenite fractionation or residual rutile. Again, such distinctly different tholeiitic and calc-alkaline characteristics are recognized for similar supracrustal rock suites across most parts of the Archaean craton in Greenland, to which the simplest explanation invokes different petrogenetic processes during the evolution of a single subduction zone system (Szilas 2012, Szilas et al. 2011a, b, 2012a, b). If the Nigerlikasik section represents a continuous meta-volcanic sequence, it also suggests a linked temporal shift existed, from the generation of the tholeiitic to the calc-alkaline suite.

We also find that the spider patterns for intrusive bio-hbl schists within the calc-alkaline suite bear a closer resemblance to stratigraphically lower bio-hbl schists (*Figure 21g*) than the uppermost bio-hbl schists (*Figure 21h*), suggesting that these were feeders to that particular volcanic sequence. It is also noted that the aplitic sheets have lower LILE, U, Th, Nb, Ta, Pb and HREE than the TTG, but otherwise overlapping patterns (*Figure 21d*).

Results from the correspondence analysis (*Figure 11*) suggested that REE patterns may be good discriminators for distinguishing a HREE-rich tholeiitic suite from a LREE-rich calc-alkaline suite. This REE-discrimination is verified in *Figure 22*, where it is shown that REE-patterns for Nigerlikasik's serpentinites, amphibolites, bio-hbl schists and rhyodacitic intrusions all differ significantly from each other, including a subtler subdivision between more 'enriched' and 'depleted' amphibolites, as well as stratigraphically lower and upper bio-hbl schists. Variations are even better constrained by plotting chondrite normalized LREE (La_N/Sm_N in *Figure 22e*), REE (La_N/Yb_N in *Figure 22f*) and HREE (Gd_N/Yb_N in *Figure 22g*) ratios against stratigraphic positions, where it is observed that corresponding REE pattern slopes are constant within units that most likely differentiated from discrete parental melts.

The results in *Figure 22* lead to an improvement of the field based stratigraphic log, after subdividing it into petrogenetically related units with similar La_N/Sm_N and La_N/Yb_N . Slightly more 'depleted' amphibolites, with $La_N/Sm_N < 1$ and $La_N/Yb_N < 1$, occur more scattered within the lower and the upper parts of the amphibolite section, and could have erupted coeval to the more 'enriched' amphibolites, with $La_N/Sm_N > 1$ and $La_N/Yb_N > 1$. However, given the difficulty of tapping a more depleted and enriched magma source within the same space and time, and the fact that the two metagabbroic samples are 'depleted', we favour a scenario where more 'depleted' basalts were emplaced after the slightly more 'enriched' basalts. In such a case, all 'depleted' basalts below the metagabbro must have *intruded* into the pre-existing 'enriched' basalts, whereas 'depleted' basalts above the metagabbro probably *erupted* onto its pre-existing surface (i.e., before the calc-alkaline suite was emplaced). Thus, even if all amphibolites must have experienced some crystal fractionation (e.g., *Figure 17*) such an inter-bedded lava/sill pile invariably upsets any replenishment or differentiation cycle trends up through the amphibolites, as was previously discussed during our description of *Figure 12*.

Rock/Chondrite (Sun & McDonald, 1989)

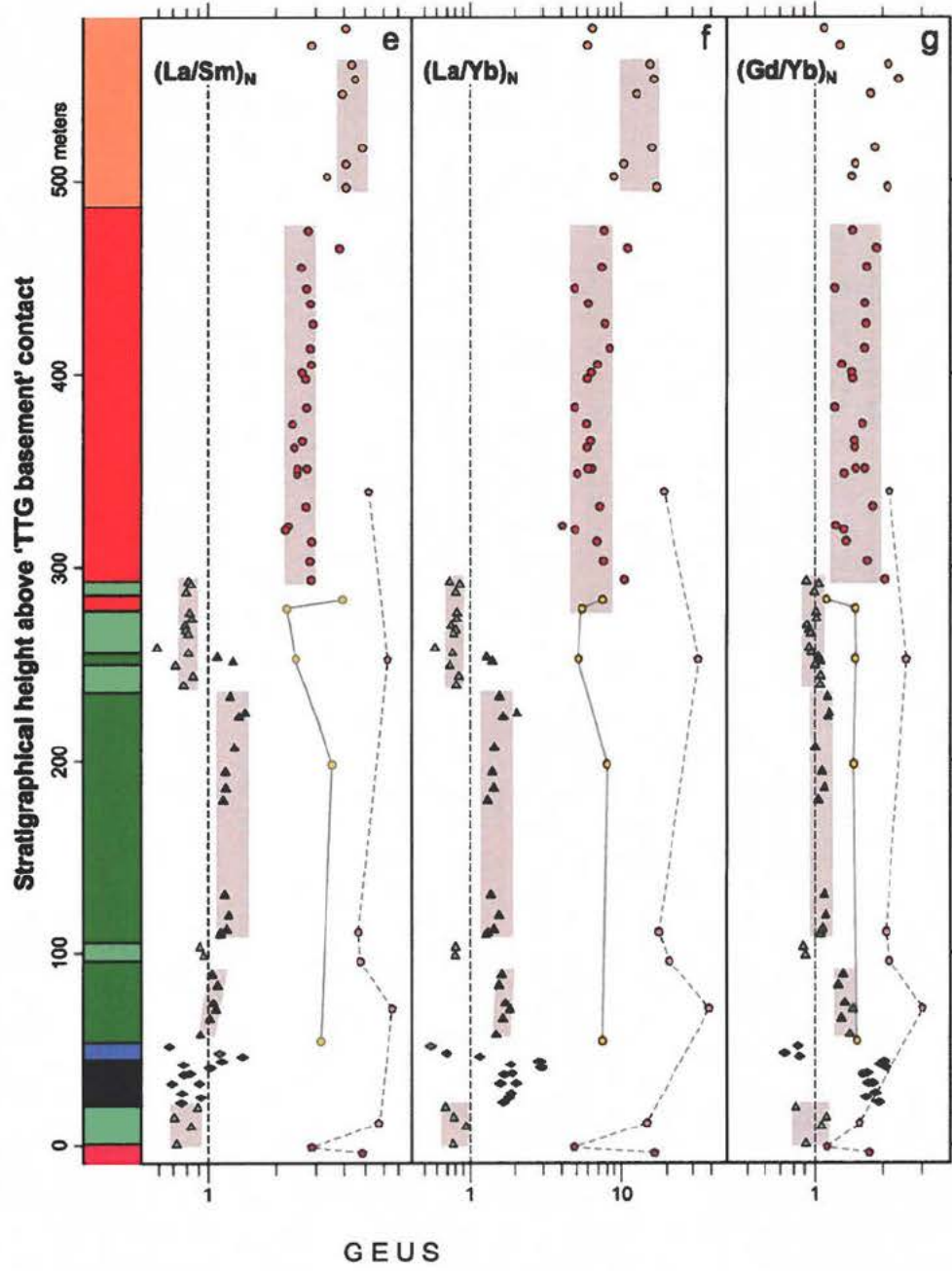
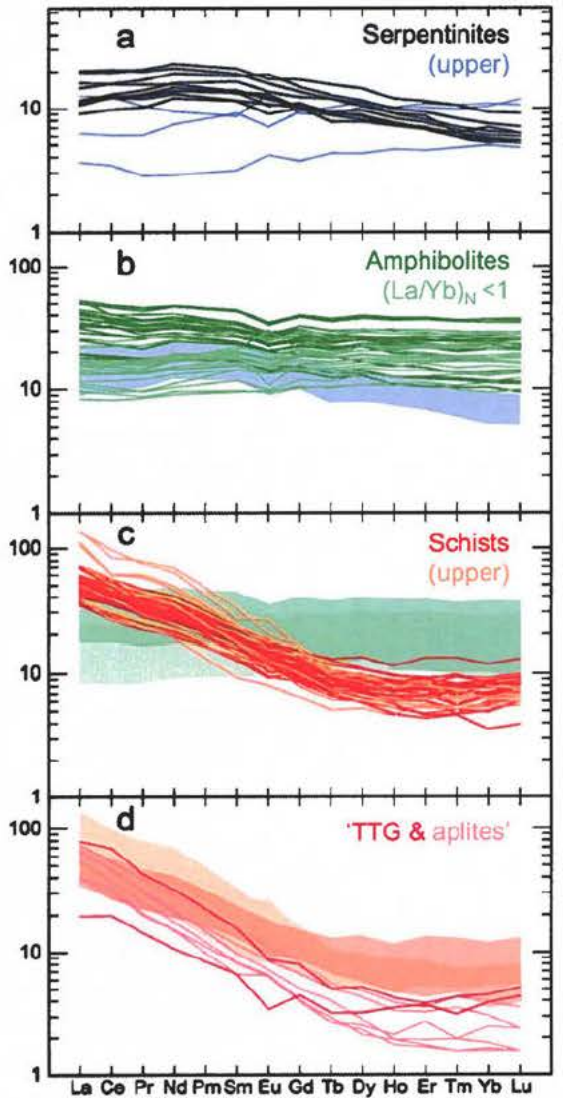


Figure 22: (previous page): Rare Earth diagrams for (a) serpentinites, (b) amphibolites, (c) bio-hbl schists, and (d) 'TTG/aplites', and stratigraphical variations in REE slopes, shown by chondrite normalized (e) LREE $(La/Sm)_N$, (f) REE $(La/Yb)_N$ and (g) HREE $(Gd/Yb)_N$ ratios. Coloured background REE-pattern ranges for other rock units are shown for comparison. Grey backgrounds emphasize stratigraphical sequences with roughly similar ratios. Stratigraphical log is primarily subdivided on the basis of similar $(La/Yb)_N$, into dark pink TTG; dark and pale purple 'typical' and 'atypical' serpentinites, respectively; dark and pale green 'enriched' and 'depleted' amphibolites, respectively; blue meta-gabbros; red and orange 'lower andesitic' and 'upper dacitic' bio-hbl schists, respectively; Other symbols as in Figure 9.

Only the 'typically' picritic serpentinites have Mg# values (up to 70), Cr (up to 2100 ppm) and Ni (up to 800 ppm) like typical mantle derived basaltic primary magmas (cf., suggested Mg# range of 66-75 by Roeder and Emslie 1970 and Green 1971), but are nevertheless viewed as unlikely direct parents to any of the amphibolitic subunits because of the dislocated geochemical trends between these groups; especially Al_2O_3 . As long as olivine accumulation can be ruled out, the serpentinites must therefore represent primary picrites that were generated as relatively high-degree partial mantle melts (both Cr and Ni conspicuously reach nearly twice the minimum concentrations suggested for present-day basaltic primary mantle melts). At similar MgO, the serpentinite samples, furthermore, have similarly low Al_2O_3 like the better preserved spinifex textured komatiitic basalts within the Barberton Greenstone Belt (Byerley 1999, Jahn et al. 1982, Lahaye et al. 1995), whereas their moderately higher TiO_2 (~0.8 wt% at ~15 wt% MgO) bears a greater resemblance to Karasjok-type komatiites (Puchtel et al. 1998, Hanskie et al. 2001). This is perhaps better illustrated by Al_2O_3/TiO_2 (5-7) and $(Gd/Yb)_N$ (~1.6-2.0) in Figure 23, where the ten Al-depleted (and 'typical') serpentinites partially overlap the two above mentioned komatiite types; first recognized as such by Scherstén and Stendal (2008).

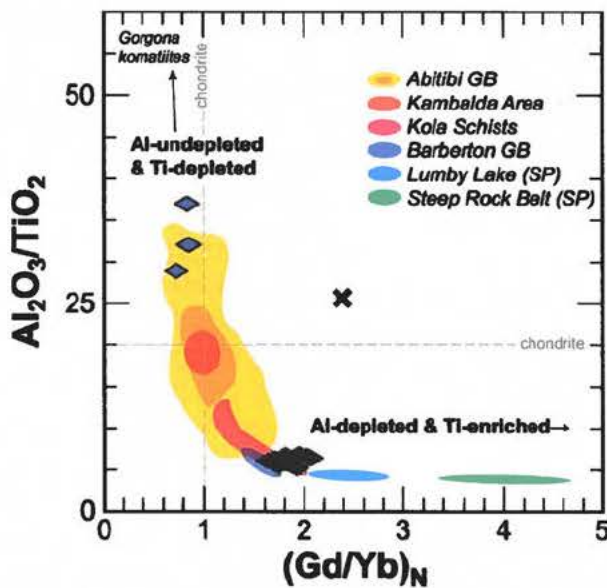


Figure 23: Al_2O_3/TiO_2 versus chondrite normalized $(Gd/Yb)_N$ for all rock types from the Nigerikasik section, compared to komatiite data from Gorgona (Aitken and Echeverria 1984, Arndt et al. 1997), Abitibi Greenstone Belt (Sproule et al. 2002), the Kambalda Area (Leshner et al. 2001), Kola Bio-hbl schist Belt (Puchtel et al. 1998), Barberton Greenstone Belt (Byerley 1999, Jahn et al. 1982, Lahaye et al. 1995), and the Lumby Lake and Steep Rock Belts in the Superior Province (Tomlinson et al. 1999). Symbols as in Figure 9.

Relatively steep REE patterns distinguish bio-hbl schists from the tholeiitic suite, but bear conspicuous resemblances to more silica-rich TTGs. Rapp et al. (1991) and Springer and Seck (1997) have shown that similar steep REE-patterns for TTGs can be reproduced through the partial melting of amphibolitized MORB rocks (i.e., garnet amphibolite; Figure 24), where progressively higher degrees of partial melting is expected to produce more

intermediate (i.e., dacitic-andesitic) melts with correspondingly more elevated HREE, as indicated by the Nigerlikasik bio-hbl schists in *Figure 22(d)*. These geochemical characteristics suggest that the calc-alkaline suite could have been derived through variable degrees of partial melting of subducted basaltic crust, instead of through high-P garnet and amphibole fractionation, as considered above. It is practically impossible, however, to differentiate between these two radically different petrogenetic models, because melts are in both cases being separated from the same minerals (garnet and amphibole). Both model interpretations will be discussed in more detail below.

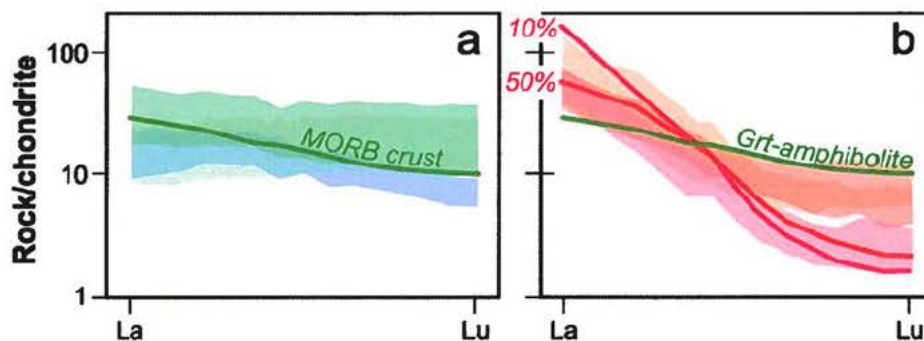


Figure 24: (a) Typical REE-pattern of an EMORB superimposed on a field of serpentinites (purple) as well as the 'enriched' (darker green) and 'depleted' (paler green) amphibolites. (b) Typical steep patterns of 10% and 50% partial melts of a garnet amphibolite with the same EMORB pattern as in (a), superimposed on a field of TTGs (pink) and the dacitic (paler orange) and andesitic (darker orange) bio-hbl schists. Fields as in *Figure 22(a-d)*.

Petrogenesis and differentiation

The tholeiitic suite includes mantle derived picrites to basaltic andesites, which exhibit geochemical island arc signatures (*Figure 20*), including negative Nb-anomalies (expressed as Nb_N/La_N in *Figure 25*). If the 'typical' serpentinites from the Nigerlikasik section represent primary picritic melts, their high $(Gd/Yb)_N$ (>1 in *Figures 22-23*) would suggest an initial segregation within a garnet-bearing mantle source, where such a residual Al-phase also helps to explain their Al-depleted signatures (Arndt et al. 2008). As mentioned, the strongly negative P and slightly negative Zr(-Hf) anomalies in (a) may even record residual majoritic garnet in an even deeper dry mantle source, implying melt extraction depth of >270 km (Xie and Kerrich, 1994). Since such a dry mantle model requires a hot rising deep mantle plume, however, it precludes a general subduction zone setting and thereby contradicts many of the other geochemical characteristics of the Nigerlikasik picrites. We therefore ask whether similar majoritic garnets may not also be stable at shallower depths within a hydrated mantle wedge, and thereby give rise to both subduction zone characteristics and the negative P, Zr and HREE characteristics?

In *Figure 23*, three 'atypical' serpentinites plot at the high Al_2O_3 -end of more Al-undepleted (Abitibi, Kambalda, Gorgona type) komatiites with near-chondritic $(Gd/Yb)_N$. Only two of Nigerlikasik's 'atypical' serpentinites, however, are truly Al-undepleted picrites whereas one is Al-depleted but also extremely low in TiO_2 . Such Al-undepleted komatiites may be produced through either shallower and/or larger degrees of (fractional) mantle melting, resulting in much less Al_2O_3 and HREE fractionation by residual garnets. Lower pressures are believed to have played a greater role during the formation of the less MgO-rich

Nigerlikasik picrites, as this is also consistent with their generally more depleted spider patterns in *Figure 21(a)* not exhibiting any Zr-anomalies. Provided that all of the deformed serpentinites represent melts the relatively high Ni and Cr of both 'typical' Al-depleted and 'atypical' Al-undepleted types (*Figure 14*) argue for these picrites to have been only slightly differentiated primary mantle melts.

A relatively variable $\text{Al}_2\text{O}_3/\text{TiO}_2$ amongst Nigerlikasik's amphibolites (6-25, not shown but ranging between the Al-depleted 'typical' and Al-undepleted 'atypical' picrites in *Figure 23*) is ascribed to these basalts' general tholeiitic differentiation (*Figure 18f*), where ilmenite never fractionated but plagioclase did, and thereby caused a progressive lowering in $\text{Al}_2\text{O}_3/\text{TiO}_2$. The amphibolites can clearly be subdivided into an earlier high- $(\text{La}/\text{Yb})_N$ group derived from a deeper and/or more 'enriched' mantle and a later low- $(\text{La}/\text{Yb})_N$ group derived from a shallower and/or more 'depleted' spinel lherzolite mantle (*Figure 20d*). The 'enriched' amphibolites do not exhibit as distinctly negative Zr-anomalies as the serpentinites to suggest these residual garnets to be high-P majorites. Given that the 'enriched' amphibolites also have the highest TiO_2 , then it seems likely that their greater apparent Nb anomalies (i.e., high La_N/Yb_N in *Figure 25b*) are artifacts of being derived from a more enriched mantle source. Considering that the tholeiitic lower part of the Nigerlikasik section likely records an emplacement history of picritic-basaltic lavas, which could have differentiated from a succession of primary batch melts that segregated from successively shallower depths, this could theoretically have occurred within the same progressively (through melting) more depleted, rising mantle plume (e.g., Campbell et al. 1989).

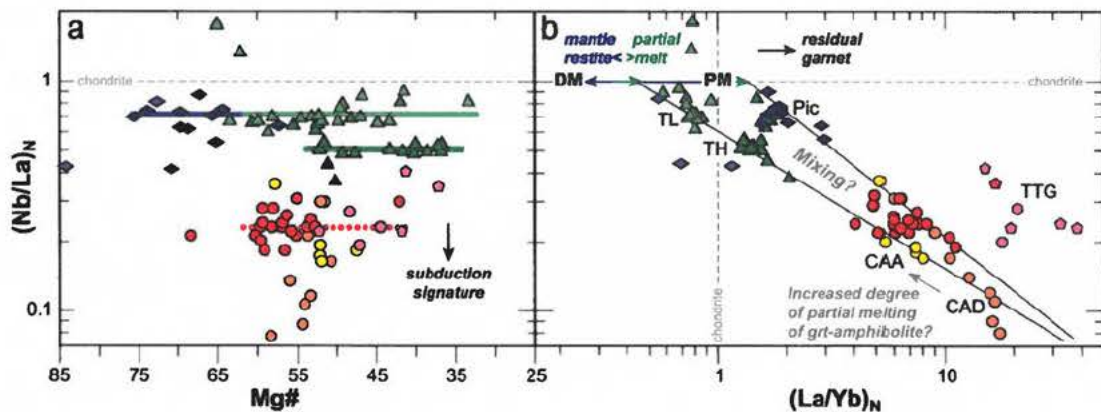


Figure 25: Chondrite normalized incompatible element ratio that describes the size of negative Nb-anomalies $[(\text{Nb}/\text{La})_N]$ are plotted against (a) Mg# and (b) chondrite normalized REE-slopes $[(\text{La}/\text{Yb})_N]$. Coloured lines in (a) represent visual best fits through progressively more differentiated samples, which could have been derived from the same parental melt. In (b), higher $(\text{La}/\text{Yb})_N$ reflect either a more fertile or garnet-bearing mantle source for the tholeiitic samples, with even higher $(\text{La}/\text{Yb})_N$ in the calc-alkaline suite reflect progressively more residual garnet in an amphibolite source. Solid lines outline a triangular area, within which any mixing between units (except TTGs and associated aplites) seem possible. DM = Depleted Mantle (senso lato); PM = Primordial Mantle; Pic = Picrites; TL = Tholeiitic basalts with low $(\text{La}/\text{Yb})_N (<1)$; TH = Tholeiitic basalts with high $(\text{La}/\text{Yb})_N (>1)$; CAA = Calc-alkaline Andesites; CAD = Calc-alkaline Dacites; TTG = Tonalite-Trondhjemite-Granodiorite gneiss. Symbols as in *Figure 9*.

As mentioned above, the calc-alkaline suite of more felsic (andesitic-dacitic) bio-hbl schists have, together with the youngest TTG and aplite intrusions, many of the geochemical characteristics (in particular high Sr+LREE and low Y+HREE) that characterize derivatives of primary high-Sr/Y melts derived through variable degrees of partially melted garnet

amphibolite sources (*Figure 24b*, Rapp et al. 1991, Springer and Seck 1997). Considering that the calc-alkaline part of the Nigerlikasik section records a likely emplacement history of first andesitic followed by dacitic pyroclastic flows, which were finally intruded by rhyodacitic aplites and TTG, we may then speculate on whether this entire calc-alkaline sequence reflects progressively lower degrees of partial melting of a progressively more refractory garnet amphibolite source. This interpretation is supported by decreasing HFSEs with decreasing degrees of partial melting, from andesites to dacites (*Figure 18*), which could have been retained in relatively refractory HFSE-rich minerals. Especially, elements that partition into more likely residual peritectic phases (e.g., HREE into garnet and Ti into rutile) that make up a progressively greater restite proportion during lower degrees of partial melting and consequent production of correspondingly more felsic magmas. One may even go so far as to regard the youngest (ca. 2.9 Ga) TTGs and associated aplites as representing the lowest degree of partially melted end-member in such a 'partial melting' trend, were it not that these rhyodacites' atypically low Sr (50-300ppm) do not extend a systematic Sr-increase (100-600 ppm) up through the andesite-dacite sequence (*Figure 16a*). Higher $(\text{Nb/La})_N$ and $(\text{La/Yb})_N$ also displace these TTGs and aplites in *Figure 25(b)* away from the possible 'partial melting' trend defined by the bio-hbl schists.

Despite having many of the geochemical characteristics of partial garnet amphibolites melts, it is unlikely that variable degrees of partial melting also is recorded by the cyclic variations up through the Nigerlikasik section (*Figures 12, 14-16*), which must instead have formed in closer proximity to later magma chamber processes. Thus, it is still possible that the calc-alkaline suite (in parts) was generated through either differentiation from a common andesitic parental melt, possibly during a combined crustal assimilation and fractional crystallization (AFC) process, and/or mixing between the calc-alkaline andesitic and (rhyo)dacitic end-member melts, discussed next.

As shown in parts by *Figure 18*, a bulk fractionating mineral assemblage would have had to have particularly high partitioning coefficients for (1) Mg, Fe, Mn, Sc, Co, Ni and Cr (e.g., olivine, orthopyroxene and amphibole), (2) Ti, Fe, V and Mn (e.g., ilmenite and rutile), and (3) HREE, Ca and to a lesser extent *al.* (e.g., garnet and clinopyroxene, but not plagioclase because Sr behaves incompatibly). The fractionation of other accessory phases, like apatite and zircon, can be ruled out because Th and U behave most incompatibly (*Figure 19a*), followed by LILEs and then some HFSEs (Nb, Ta, Zr, Hf) and metals (W, Zn, Mo and Sn). Amongst the possible fractionating phases, listed above, garnet+amphibole offers the most likely assemblage, because it can explain all of the observed variations and appears to be stable within >30 km-deep and hydrous magma chambers (Alonso-Perez et al. 2009). The increasing Sr (*Figure 19b*) argues against any andesitic parental melts having fractionated plagioclase within a shallow magma chamber.

Magma mixing cannot reconcile the picritic, tholeiitic and calc-alkaline suites, but may well explain many distinct and straight geochemical trends within each suite. As argued above, variations within the picritic and the tholeiitic suites can just as well be explained by simpler fractional crystallization, whereas models indicate that the calc-alkaline suite may well have been caused by mixing of an andesitic and a (rhyo)dacitic end-member. These mixing models do not, however, necessarily require two melts of different compositions because a differentiating magma reservoir filled by an andesitic end-member may also have been assimilating the lower island arc crust (i.e., typical AFC process). A closer scrutiny of the latter hypothesis provides many supporting AFC trends but also one disconcerting lack of an equally continuous Sr-trend between the bio-hbl schists and the rhyodacitic aplites and TTG (*Figure 19b*). Thus, magma mixing only seems to have been possible between an andesitic and a dacitic end-member.

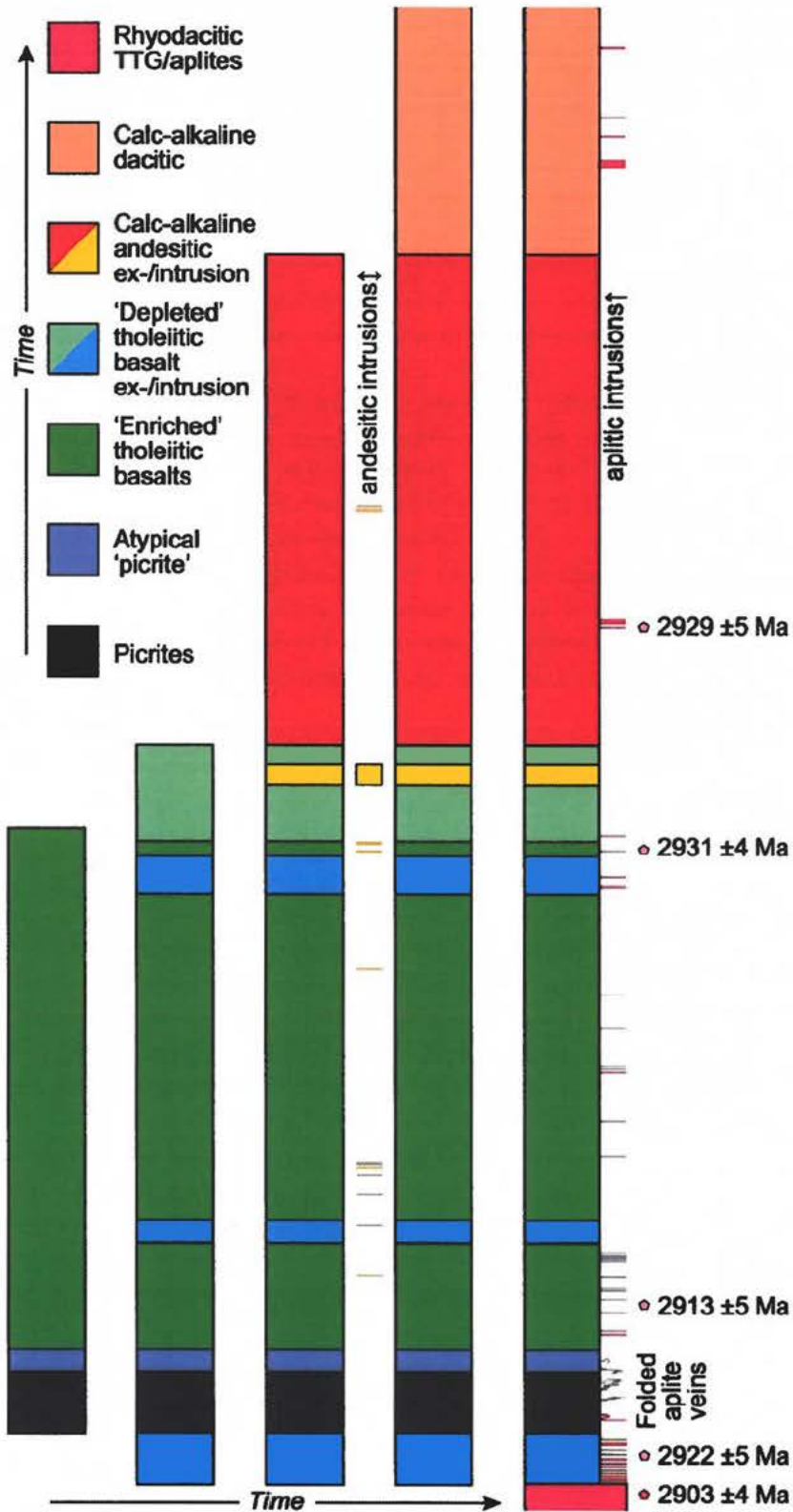


Figure 26: Stratigraphical evolution of the Nigerlikasik meta-volcanic section shown as schematic profiles at consecutive time slices (Time; based on field evidence and geochemistry, and progressing towards the right). Absolute ages shown to the right-hand side are zircon U-Pb ages (see Figure 7).

Model implications

Presented field evidence and geochemistry suggest that the Nigerlikasik section is a composite tholeiitic and calc-alkaline meta-volcanic sequence, which most likely was emplaced as shown in the sequence depicted in *Figure 26*. This interpretation is similar to the komatiitic-basaltic Onverwacht Group and overlying Fig Tree with felsic volcanic (Brandl et al. 2006), but opposite to Dostal and Mueller's (1997) report of the Abtibi Greenstone Belt, where the Archaean mafic-ultramafic Stoughton-Roquemaure Group conformably *overlies* the 2.73 Ga calc-alkaline felsic Hunter Mine Group sequence. However, the Nigerlikasik sequence is probably orientated the right way up because there is no evidence of it being significantly disrupted after its emplacement (e.g., no dislocations along major faults nor larger overturned isoclinal folds). Moreover, it seems overwhelmingly likely that the section was simply rotated and stretched within the flank zone of a single, tight, and upright syncline. Hollings et al. (1999), furthermore, describe other komatiite–basalt occurrences along many other parts of the Northern Superior Province greenstone belts, which contain intercalated (and thereby coeval) intermediate–felsic metavolcanics. Thus, such stratigraphical records through Archaean supracrustal/greenstone belts, as presented by the Nigerlikasik meta-volcanic section, adds additional temporal constraints on both the petrogenesis and tectonic setting of Archaean tholeiitic mafic and calc-alkaline felsic volcanic rocks, which are consistent with four different models presented below.

Combined island arc and backarc

Given that the early tholeiitic suite bears many resemblances to MORB type crust, whereas the calc-alkaline suite could have been produced through partial melting of the same MORB type crust (e.g., *Figure 24*), the bimodal Nigerlikasik meta-volcanic sequence may be explained by a combined island back-arc model, as depicted in *Figure 27*. In this model, the Nigerlikasik serpentinites and amphibolites represent the metamorphosed upper parts of an oceanic crust that was generated along a (back-arc) spreading centre, whereas the hbl-bio schists were emplaced as andesite-dacite pyroclastic flows on top of such a crust within an island arc and after a dense (old) slab started subducting into the hot Archaean mantle (*Figure 27*).

Mantle upwelling below a back-arc spreading centre would partially melt to different degrees and at different depths, with the earliest picrites being derived through high degrees of partial melting of a relatively enriched mantle (\pm plume) source, at relatively greater depths (>270 km) where majoritic garnet was stable (Arndt et al. 2008). The subsequent tholeiitic suite differentiated from primary melts that segregated from a progressively more depleted and shallower mantle source (Campbell et al. 1989), with the 'depleted' basalts being in equilibrium with a spinel-bearing mantle at <60 km depth (cf., previous section of petrogenesis). While many MORB-like geochemical characteristics of the tholeiitic suite support an origin from a spreading centre environment, the subduction-like geochemistry in the calc-alkaline rocks (*Figures 20-21* and Nb_N/La_N in *Figure 25*) also seems to require some hydrated mantle wedge involvement, which, in this model, argues for a more compact back-arc spreading centre setting. This mantle wedge entrainment may have been locally variable, since the earliest picrites and the latest 'depleted' amphibolites share similar (small) subduction signatures, whereas the 'enriched' amphibolites, of intermediate age, have more marked subduction signatures. Thus, one possibility is that the tholeiitic picrite

→ 'enriched' basaltic andesite → 'depleted' basalt suite could reflect the tapping of a rising mantle (plume) that also becomes progressively more depleted in residual garnet as well as incompatible elements in general (e.g., Campbell et al. 1989).

The calc-alkaline suite is characterised by high LILE/HFSE, high LREE/HREE as well as negative Nb-Ta anomalies which, taken together, represents a stronger geochemical argument for a subduction zone setting for these rocks. One obvious model is therefore that these andesites-dacites were emplaced within an island arc that was instigated above an older overriding MORB plate, which, in turn, may have been generated along a spreading centre, as suggested in the left side of *Figure 27* (Martin et al. 2005). Rather than representing differentiated mantle wedge melts, it was argued above that the calc-alkaline andesites-dacites were generated through varying degrees of partial melting of a garnet amphibolitized subducting slab, as suggested in the right side of *Figure 27*.

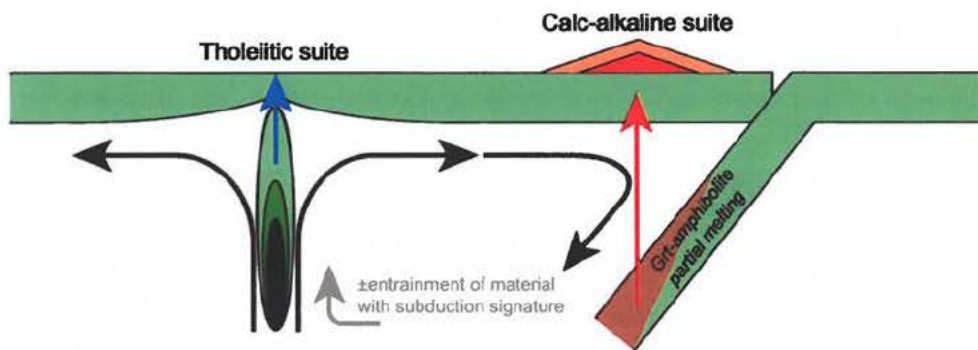


Figure 27: Combined island back-arc model with a tholeiitic (back-arc) spreading centre and a juvenile island arc setting where the subducted slab undergoes partial melting. A progressively shallower depth of partial melting and primary melt segregation for the picritic serpentinites (dark blue), the 'enriched' (dark green) and the 'depleted' (pale green) basaltic amphibolites is tentatively indicated below the spreading centre, whereas the entrainment of mantle wedge material is required to explain their subduction zone signatures.

Even if a combined island back-arc may explain compositional and relative temporal variations within the Nigerlikasik sequence, it has the following major flaw: In order for hydrated mantle wedge material to become entrained in an asthenospheric mantle (plume) beneath the back-arc rift in *Figure 27*, some slab dehydration must have preceded the onset of slab melting, and such a sequence of events conflicts with the fact that subduction zones tend to cool with time (e.g., van Keken and King 2004). The only way to circumvent this problem is to allow both dehydration and partial hydrous melting of a subducting slab, which may be possible during even faster slab-subduction into an even hotter mantle, during the Archaean. As an alternative, this, in turn, opens up for a simpler model of generating both of Nigerlikasik's tholeiitic and calc-alkaline suites within the same, single island arc setting, discussed next (*Figure 28*).

Single island arc with slab melting

If an Archaean island arc setting is required for all samples to lie within various geochemical discrimination fields defined for Phanerozoic island arc basalts (*Figure 20*), we need to test whether the emplacement history recorded by the Nigerlikasik meta-volcanic section may somehow have been produced in the same island arc system; i.e., during a single

subduction zone cycle. It should be remembered that even Phanerozoic subduction zones are far from fully understood, with a number of physical parameters and phase transitions varying in both space (across, along and between arcs), during a subduction cycle, as well as between Phanerozoic and Archaean arc systems.

As indicated above, we would intuitively expect younger/faster slab-subduction into a hotter Archaean mantle to give rise to slab melting, rather than slab dehydration giving rise to a hydrated mantle wedge, which in turn gives rise to primary island arc type basalts. However, recent experiments have shown that a sufficiently fast subduction rate gives rise to early sub-solidus dehydration of the uppermost parts of the subducting slab, whereas lower, more protected parts of the slab subsequently dehydrate when the upper eclogitic parts of the slab have reached hydrous melting temperatures (Laurie and Stevens 2010, 2012); thus, enabling hydrous melting of both the subducting slab and the overlying hydrated mantle, which is dragged down with it (Figure 28). Such a scenario would be able to generate penecontemporaneous (ultra)mafic mantle-derived and more felsic crustally derived partial melts, where an intermittent stabilization of rutile in the subducting slab may help explain even greater negative Nb-Ta anomalies amongst the latter calc-alkaline suite.

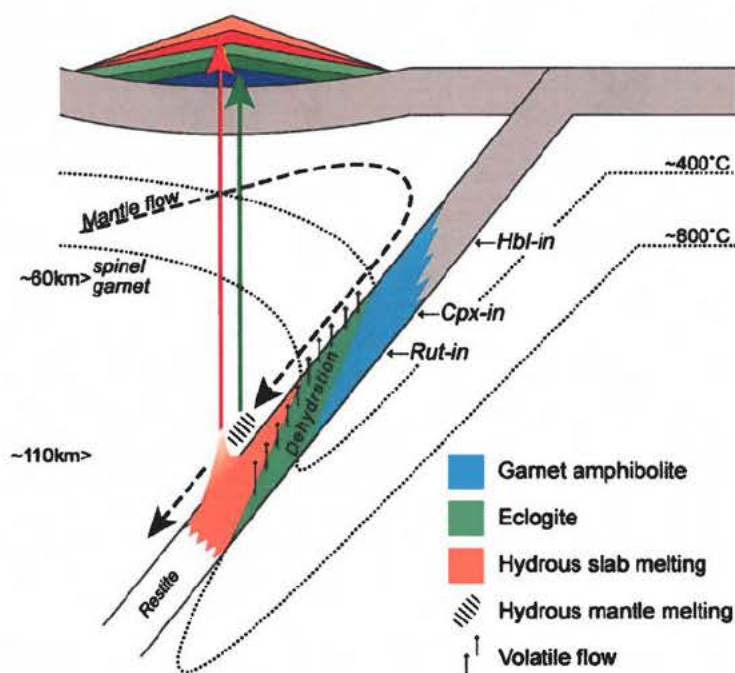


Figure 28: Both tholeiitic and calc-alkaline suites generated within one island arc. Subducting slab first gets metamorphosed to garnet amphibolite and then dehydrates into an eclogite, both before (upper part of slab) and after (lower part of slab) hydrous partial slab melting is initiated at $\sim 800^{\circ}\text{C}$. Higher up along the slab, this leads to mantle wedge hydration (e.g., pargasite), which, breaks down at 110 km depth, leading to hydrous mantle melting and generation of primary tholeiitic melts. During fast subduction, delayed (disequilibrium) dehydration along the base of the slab lead to hydrous partial melting of overlying eclogite, which in turn may lead to a coinciding calc-alkaline suite of andesitic-dacitic melts.

In the hypothetical model in Figure 28, it is possible for dehydration to set in when the slab reaches ca. 400°C , enabling the upper part of the slab to hydrate the mantle wedge from ca. 60 to 90 km depth, below which hydrous melting of the slab increases both into and down along the slab. It is also presumed that much of this slab melting roughly coincides with the common ~ 110 km depth of mantle pargasite breakdown and resulting hy-

drous partial mantle melting, leading to both of these primary melt types to roughly co-existing in the same part of the mantle.

It remains to be explained how two such different, yet roughly penecontemporaneous, primary melts may have segregated, risen, and finally become emplaced into/onto the upper parts of the overriding plate, in the relative tholeiite to calc-alkaline sequence observed across the Nigerlikasik section and without significant mixing to have occurred between these two units. One possibility is that (ultra)mafic mantle melts segregated and rose faster than the more viscous calc-alkaline felsic suite of crustal melts. However, until such important details within the complex and variable island arc setting are resolved, it is also worth considering other alternative model explanations for the generation of the bimodal meta-volcanic sequence at Nigerlikasik; namely including an hypothetical island arc's progression towards oceanic crustal accretion (*Figure 29*).

Progressive island arc to crustal accretion

Hydrous partial melting of garnet amphibolites need not be restricted to within subducting oceanic slabs, as indicated in *Figure 28*, but may also occur within any basaltic crust that is subjected to amphibolite facies P-T conditions. As it, furthermore, is more difficult for thicker – and thereby less dense – Archaean oceanic crust to cool sufficiently above a more vigorously convecting Archaean mantle, and thereby become dense enough to initiate subduction, it is expected that much Archaean oceanic crust accreted into thickened 'plateaus' (Davies 1992, Zegers and van Keken 2001, Bedard 2006, van Hunen *et al.* 2008), at the base of which garnet amphibolites may have partially melted (*Figure 29b*). Even if this adequately explains the generation of our calc-alkaline suite, it fails to explain the island arc character of our tholeiitic suite, which inevitably requires some initial subduction zone to have been operating at the time.

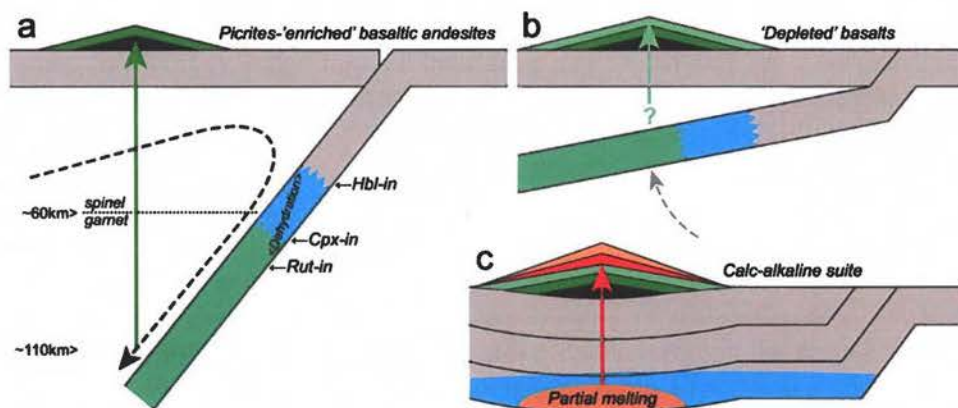


Figure 29: Progression towards an oceanic crustal accretion model. (a) Waning stages of island arc model in *Figure 28(b)*, where the latest phase of 'depleted' tholeiitic basalts (pale green) may have been 'squeezed' out of a compacting mantle wedge. (b) Calc-alkaline andesite-dacite (red-orange) suite through partial melting of slab-accreted crust (modified from Davis 1992, Zegers and van Keken 2001). (c) Sufficient thickening through imbrication, thrust-stacking and/or flat subduction of oceanic plates is necessary to lower the oceanic crust into the garnet amphibolite to eclogite stability field (~60 km), where hydrous partial melting will produce the characteristically HREE-depleted and relatively Sr-rich calc-alkaline andesite-dacite suite, as well as subsequent TTGs and associated rhyodacitic aplite sheets.

A model that first generated a tholeiitic suite within an island arc (*Figure 29a*) and then (gradually?) changed (*Figure 29b*) into a superimposed accreted system (*Figure 29c*) requires that (1) the island arc first initiated sufficiently far from a spreading centre, for a sufficiently dense and cold slab to be subducted, and that either (2) the spreading centre thereafter approached the subduction zone and/or (3) the slab broke off, so that the accretion of progressively younger, less dense and hotter oceanic crust could commence along the same island arc. It does, of course, not have to be such a related pair of magmatic events that coincided to produce the Nigerlikasik bimodal sequence; it is just the most eloquent option. The lateral extent of such thickened accreted crusts also offers a necessary explanation for widespread emplacement of roughly coeval TTGs across Archaean terranes, into which several generations of supracrustal sequences may have been in-folded during the final amalgamation of the South-West Greenland craton, at ca. 2.7 Ga.

A progression from island arc to accreted oceanic terranes is more consistent with most geological observations and geochemical characteristics presented in this paper. It fulfils the need for supracrustal serpentinites and amphibolites to have been generated within an island arc, where the lack of any residual garnet signature of the late phase of 'depleted' amphibolites, arguably, can be explained by shallow 'squeezed out' primary melts during the closure of mantle wedge (*Figure 29b*). It generates, with greater certainty, the calc-alkaline suite *after* the emplacement of the tholeiitic suite, as well as offers an explanation for widespread final intrusion of TTG plutons and associated aplitic sheets.

The above tectono-magmatic models all hinge on petrogenetic models, suggesting that the picritic serpentinites and basaltic amphibolites were generated as either deeper and drier mantle melts (Arndt et al. 2008) or shallower and more hydrous mantle wedge melts (Parman et al. 2004), whereas the calc-alkaline suite of andesitic-dacitic bio-hbl schists were derived from a crustal source (either a garnet amphibolite or hydrated eclogite). These petrogenetic models may be questioned, however, and thereby lead to alternative tectono-magmatic models, including the following, simpler, single island arc system *without* significant crustal melting (e.g., Szilas 2012, Szilas et al. 2011a, b, 2012a, b), where the calc-alkaline suite may have been generated through high-P (>1.0 GPa) garnet + amphibolite fractionation (Alonso-Perez et al. 2009) of mantle-derived melts.

Single island arc without significant crustal melting

Szilas (2012) and Szilas et al. (2012a) propose that their similar volcanic units, studied at three different and more fragmented localities across southern West and South West Greenland, could have been generated during the evolution of a single island arc system, following the temporal sequence of all units combined within a single composite section at Nigerlikasik: Basically, Szilas' model suggests (1) ultramafic-mafic partial melts were derived from a juvenile hydrous mantle wedge, which was variably enriched by small batches of adakitic crustal melts (producing the 'enriched' tholeiites), (2) calc-alkaline primary magmas were produced through mixing, crustal assimilation, storage and homogenization (i.e., MASH, Hildreth and Moorbath 1988) in an 'underplated' sub-crustal zone, as proposed for modern continental arcs, and (3) TTG melts (including aplites) formed as extensive partial lower crustal melts as the island arc system accreted and thickened into a proto-craton. We find this to be the most eloquent model option, which lends many of its petrogenetic processes to our current understandings of modern subduction zone systems, and our results from the Nigerlikasik section supports and adds to it the following ways.

The petrogenesis of the tholeiitic suite is very much as we envisage for both of our previous island arc models in *Figures 28-29*, with the possible mantle wedge enrichment by small batches of adakitic melts helping to explain slightly more negative Nb-anomalies, lower La_N/Yb_N -ratios (*Figure 25*) and other geochemical characteristics of our 'enriched' basaltic andesites; i.e., without the need for a more traditional enriched mantle (plume) component. Stratigraphical constraints at Nigerlikasik are consistent with this slab melting and mantle enrichment to have been restricted to the early stages of subduction, beneath a hot juvenile island arc, because subsequent 'depleted' basalts do not record this enrichment. Our early picrites are also consistent with a hotter juvenile island arc, wherein an initial greater degree of partial hydrous mantle melting could have generated picrites without the need of a mantle plume.

A model without primary partial crustal melting offers a simpler and radically different explanation for the petrogenesis of the calc-alkaline andesite-dacite suite. High-P (>1.0 GPa) garnet+amphibole fractionation, furthermore, may reduce the need for crustal assimilation of mantle-derived parental melts above a sub-crustal magma reservoir, or MASH zone, because high-P fractional crystallization helps explaining much of the geochemical variation within the calc-alkaline andesite-dacite suite. While it is still difficult to envisage how such differentiation trends may have been preserved after >30 km of melt propagation up through the island arc crust, in order to be recorded within the cyclic units (e.g., CaO in *Figure 12d*) of the Nigerlikasik section, these cycles would be practically impossible to relate to varying degrees of partial slab melting. It is possible that only the overall stratigraphical trend from more 'primitive' andesites to more 'evolved' dacites is determined by either crustal melting or high-P garnet+amphibole fractionation, whereas the cyclic trends are better explained by low-P fractionating assemblages, which may consist of clinopyroxene, plagioclase and ilmenite. The relatively constant La_N/Sm_N , La_N/Yb_N and Gd_N/Yb_N in *Figure 22(e-g)* argue for such correspondingly unique parental melts for each of the major groups; e.g., the tholeiitic picrites, 'enriched' basaltic andesites and 'depleted' basalts derived from different degrees of partial melting of variably enriched mantle wedge sources, and the calc-alkaline andesites, dacites and rhyodacites derived from either different degrees of partial melting of some garnet amphibolite crustal source (most likely a subducting slab) or parental mantle wedge melts that had experienced variable degrees of high-P garnet + amphibole fractionation.

The final petrogenesis of the TTGs and associated aplitic sheets in Szilas model, as derived through extensive, regional partial melting of the base of an accreted and thickened proto-craton, is also very much as we envisage it in *Figure 29(c)*. Apart from a few 'base' samples and aplitic sheets, however, our data from the Nigerlikasik section do not really address this regional TTG-event, which seems to be a typical closure to the evolution of most supracrustal (or greenstone) belts within Archaean cratons.

Summary and conclusions

Field observations and the geochemistry of 99 samples from a ~550 m wide supracrustal sequence of serpentinite → amphibolites → bio-hbl schist at Nigerlikasik (South-West Greenland) are consistent with a composite meta-volcanic picrite → tholeiitic basalt-basaltic andesite → calc-alkaline andesite-dacite section, recording the following:

- 1) Picrites erupted onto the surface of something that no longer appears to be in direct contact with. Their geochemical resemblance to low- Al_2O_3/TiO_2 , Ti-enriched Karasjok-

type komatiites argues for a similar origin, which in our case can be any large degree partial melting of any enriched (E-MORB type) and majoritic garnet-bearing mantle source, followed by some (Mg,Fe)-silicate + Cr-spinel fractionation during ascent.

- 2) Tholeiitic basalts to basaltic andesites erupted onto the picrites. These more typical primary mantle melts segregated from a lower pressure garnet-bearing but perhaps more transitional (T-MORB type) source, and most likely followed by plagioclase + (Mg,Fe)-silicate + Cr-spinel fractionation during ascent.
- 3) A slightly more 'depleted' sequence of tholeiitic basalts mainly intruded into the pre-existing lava pile, as well as erupted onto its surface. These primary melts segregated from a more depleted and garnet-free (spinel) mantle, followed by fractionation of a similar mineral assemblage as the previously more 'enriched' tholeiites.
- 4) A calc-alkaline sequence of andesitic to dacitic melts both intruded into and erupted as pyroclastic flows onto the tholeiitic pile. The more HREE-depleted, LILE+Sr-enriched and evolved (felsic) character of these meta-volcanic rocks, compared to the petrogenetically unrelated tholeiitic suite, is consistent with either a primary garnet amphibolite crustal source or primary mantle melts that underwent high-P garnet+amphibole fractionation. The similar phases in each model interpretation make it difficult to distinguish between the two. Cyclic 'differentiation' trends up through the stratigraphy are more easily attributed to high-P fractionation but could also be related to subsequent low-P fractionation of parental melts derived either from the garnet amphibolite source or through garnet+amphibole fractionation.
- 5) During ~2930-2900 Ma, rhyodacitic intrusions finally intruded the base of the sequence (forming the TTG 'basement') and as aplitic sheets into the composite tholeiitic and calc-alkaline meta-volcanic sequence. These rhyodacites are probably part of a regional suite of widely distributed and roughly coeval rocks of similar compositions, which may overall have been generated through even low degrees of partial melting at the base of an accreted and substantially thickened proto-craton.

The calc-alkaline suite cannot be derived from the tholeiitic suite through crystal fractionation and the two suites are furthermore derived from completely different sources. Several tectonomagmatic models have been proposed in order to explain the petrogenesis of each suite, but this report may be the first to review three combined models that satisfy the successive emplacement of a mantle-derived tholeiitic suite followed by a crustally derived calc-alkaline suite. Crustal melting models are seriously challenged by possibility of the calc-alkaline suite being derived through high-P fractionation of garnet+amphibole within a magma reservoir at the base of a thickened island arc crust. Before this alternative is properly evaluated, however, it currently seems more likely that:

- 1) The tholeiitic suite was generated within an island arc, through current-day processes of hydrous partial melting of a mantle wedge that may have been enriched by small quantities of adakitic crustal melts. Primary melts to the last phase of 'depleted' basalts were either 'squeezed out' of a compacting mantle wedge, as the slab for some reason (e.g., slab break-off, roll-off or decreased age of subducting slab) rose upwards, or derived from a less enriched mantle wedge.
- 2) Continued slab buoyancy maintained shallow subduction and/or other forms of slab accretion, resulting in a thickened oceanic 'plateau', at the base of which first high then decreased degrees of partial hydrous melting of garnet amphibolites gave rise to the calc-alkaline andesitic-dacitic sequence.

Acknowledgements

The University of Stellenbosch gave MBK leave of absence for his field work in 2010. We thank all members of the GEUS 2010 expedition to South-West Greenland for contributing towards its success; especially Jochen Kolb and Sam Weatherley for discovering and inviting us to investigate the Nigerlikasik section. A thorough review of this report was made by Jochen Kolb.

References

- Aftalion, M., Bowes, D.R., Vrána, S., 1989. Early Carboniferous U–Pb zircon age of garnetiferous, perpotassic granulites, Blanský les massif, Czechoslovakia. *Neues Jahrbuch für Mineralogie, Monatshefte* **4**, 145–152.
- Aitken, B.G. and Echeverria, L.M., 1984. Petrology and geochemistry of komatiites and tholeiites from Gorgona Island, Colombia: *Contributions to Mineralogy and Petrology* **86**, 94–105.
- Alonso-Perez, R., Müntener, O. and Ulmer, P., 2009. Igneous garnet and amphibole fractionation in the roots of island arcs: experimental constraints on andesitic liquids. *Contributions to Mineralogy and Petrology* **157**, 541–558.
- Arndt, N.T., Kerr, A.C. and Tarney, J., 1997. Dynamic melting in plume heads: the formation of Gorgona komatiites and basalts. *Earth and Planetary Science Letters* **146**, 289–301.
- Arndt, N., Leshner, C.M. and Barnes, S.J., 2008. *Komatiite*, Cambridge University Press, Cambridge, 488 pp.
- Baier, J., Audetat, A. and Keppler, H., 2008. The origin of the negative niobium tantalum anomaly in subduction zone magmas. *Earth and Planetary Science Letters* **267**, 290–300.
- Bedard, J.H. 2006. A catalytic delamination-driven model for coupled genesis of Archaean crust and sub-continental lithospheric mantle. *Geochimica et Cosmochimica Acta* **70**, 1188–1214.
- Bernstein, S.B. 1994. High-pressure fractionation in rift-related basaltic magmatism: Faeroe plateau basalts. *Geology* **22**, 815–818.
- Bickle, M.J., Nisbet, E.G. and Martin, A. 1994. Archean greenstone belts are not oceanic crust. *Journal of Geology* **102**, 121–138.
- Brandl, G., Cloete, M. and Anhaeusser, C.R., 2006. Archaean Greenstone belts. In: Johnson, M.R., Anhaeusser, C.R. and Thomas, R.J. (eds). *The Geology of South Africa*. Geological Society of South Africa, Johannesburg/Council of Geosciences, Pretoria, 691 pp.
- Bridgewater, D., McGregor, V.R. and Myers, J.S., 1974. A horizontal tectonic regime in the Archaean of Greenland and its implications for early crustal thickening. *Precambrian Research* **1**, 179–197.
- Bridgewater, D., Keto, L., McGregor, V.R. and Myers, J.S., 1976. Archaean gneiss complex of Greenland. In: Escher, A., Watt, W.S. (eds.). *Geology of Greenland*, Grønlands Geologiske Undersøgelse, Copenhagen, 18–75.
- Byerly, G.R., 1999. Komatiites of the Mendon Formation: Late-stage ultramafic volcanism in the Barberton Greenstone Belt. In: Lowe, D.R. and Byerly, G.R. (eds.). *Geological Evolution of the Barberton Greenstone Belt, South Africa*. Boulder, Colorado, *Geological Society of America Special Paper* **329**, 189–211.
- Campbell, I.H., Griffiths, R.W. and Hill, R.I. 1989. Melting in an Archaean mantle plume: heads it's basalts, tails it's komatiites. *Nature* **369**, 697–699.
- Clausen, S.E. 1998. *Applied Correspondence Analysis: An Introduction (Quantitative Applications in the Social Sciences)*. SAGE University Paper **121**, 50 p.
- Condie, K.C., 1981. *Archaean Greenstone Belts*. Elsevier, Amsterdam, 435 pp.
- Coney, P.J., Jones, D.L. and Monger, J.W.H. 1980. Cordilleran suspect terranes. *Nature* **288**, 329–333.
- Davies, G.F. 1992. On the emergence of plate tectonics. *Geology* **20**, 963–966.
- de Wit, M.J., 2004. Archaean Greenstone Belts do Contain Fragments of Ophiolites. *Developments in Precambrian Geology* **13**, 599–614.

- Dostal, J. and Mueller, W.U., 1997. Komatiite Flooding of A Rifted Archean Rhyolitic Arc Complex: Geochemical Signature and Tectonic Significance of the Stoughton Roquemaure Group, Abitibi Greenstone Belt, Canada. *Journal of Geology* **105**, 545-564.
- Donaldson, C.H. 1982. Spinifex-textured komatiites: a review of textures, composition and layering. In: Arndt, N.T. and Nisbet, E.G. (Eds.), *Komatiites*. George Allen and Unwin, London. 213-244.
- Escartín, J. Hirth, G. and Evans, B. 2001. Strength of slightly serpentinized peridotites: Implications for the tectonics of oceanic lithosphere. *Geology* **29**, 1023–1026.
- Escartín, J. Andreani, M., Hirth, G. and Evans, B. 2008. Relationships between the microstructural evolution and the rheology of talc at elevated pressures and temperatures. *Earth and Planetary Science Letters* **268**, 463-475.
- Escher, J.C., 1971. *The geology of Akuliaq with particular bearing on the origin and evolution of the supracrustal Kvanefjord belt, Frederikshåb area, South-West Greenland*. Unpublished thesis, University of Lausanne.
- Evans, B., Frederich, J.F. and Wong, T.-F. 1990. The brittle-ductile transition in rock: recent experimental and theoretical progress. In: Duba, A.G., Durham, W.B., Handin, J.W. and Wang, H.F. (ed.) *The brittle-ductile transition in rocks: the Heard volume. Geophysical Monographs* **56**, 1-20.
- Friend, C.R.L. and Nutman, A.P. 2001. U-Pb zircon study of tectonically-bounded blocks of 2940-2840 Ma crust with different metamorphic histories, Paamiut region, South-West Greenland: Implications for the tectonic assembly of the North Atlantic craton. *Precambrian Research* **105**, 143-164.
- Friend, C.R.L. and Nutman, A.P. 2005. New pieces to the Archaean jigsaw puzzle in the Nuuk region, southern West Greenland: steps in transforming a simple insight into a complex regional tectonothermal model. *Journal of the Geological Society of London* **162**, 147-162.
- Friend, C.R.L., Nutman, A.P. and McGregor, V.R., 1987. Late-Archaean tectonics in the Færingehavn-Tre Brødre area, south of Buksefjorden, southern West Greenland. *Journal of the Geological Society of London* **144**, 369-376.
- Friend, C.R.L., Nutman, A. P. and McGregor, V. R. 1988. Late Archaean terrane accretion in the Godthåb region, southern West Greenland. *Nature* **335**, 535-538.
- Friend, C.R.L., Nutman, A.P., Baadsgaard, H., Kinny, P.D. and McGregor, V.R., 1996. Timing of late Archaean terrane assembly, crustal thickening and granite emplacement in the Nuuk region, southern West Greenland, *Earth and Planetary Science Letters*, **142**, 353-365.
- Furnes, H., de Wit, M., Staudigel, H., Rosing, M., and Muehlenbachs, K. 2007. A vestige of Earth's oldest ophiolite. *Science* **315**, 1704-1707.
- Furnes, H. Rosing, M., Dielk, Y. and de Wit, M. 2009. Isua supracrustal belt (Greenland) – A vestige of a 3.8 Ga suprasubduction zone ophiolite, and the implications for Archean geology. *Lithos* **113**, 115-132.
- Green, D.H. 1971. Compositions of basaltic and nephelinitic magmas in the Earth's mantle. *Tectonophysics* **13**, 42-71.
- Hanski, E., Huhma, H., Rastas, P. and Kamenetsky, V.S., 2001. The Palaeoproterozoic Komatiite-Picrite Association of Finnish Lapland. *Journal of Petrology* **42**, 855-876.
- Hildreth, W., 1981. Gradients in silicic magma chambers: implications for lithospheric magmatism. *Journal of Geophysical Research* **86**, 10153-10192.
- Hildreth, W. and Moorbath, S., 1988. Crustal contribution to arc magmatism in the Andes of Central Chile. *Contributions to Mineralogy and Petrology* **98**, 455-489.
- Hollings, P., Wyman, D. and Kerrich, R., 1999. Komatiite–basalt–rhyolite volcanic associations in Northern Superior Province greenstone belts: significance of plume-arc interaction in the generation of the proto continental Superior Province *Lithos* **46**, 137-162.
- Jahn, B.-M., Gruau, G., Glickson, A.Y., 1982. Komatiites of the Onverwacht Group, South Africa: REE chemistry, Sm Nd age and mantle evolution. *Contributions to Mineralogy and Petrology* **80**, 25-40.
- Irvine, T.N. and Baragar, W.R.A. 1971. A guide to the chemical classification of the common volcanic rocks. *Canadian Journal of Earth Sciences* **8**, 523–548.
- Jensen, L.S. 1976. A New Cation Plot for Classifying Subalkalic Volcanic Rocks. *Ontario Geological Survey Miscellaneous Paper* **66**.
- Kalsbeek, F. and Taylor, P.N. 1985. Age and origin of early Proterozoic dykes in South-West Greenland. *Contributions to Mineralogy and Petrology*. **89**, 307-316.

- Keulen, N, Schumacher, J.C. and Kokfelt, T.F. 2011. Notes on established structural profiles related to the 1:100 000 digital geological map of southern West and South-West Greenland, 61°30' - 64°N. *Geological Survey of Denmark and Greenland Report 2011/13*, 68 pp.
- Kohlstedt, D.L., Evans, B. and Mackwell, S.J. 1995. Strength of the lithosphere: Constraints imposed by laboratory experiments. *Journal of Geophysical Research* **100**, 17587-17602.
- Kolb, J., 2011. *Metamorphosed and orogenic gold-quartz veins of the Paamiut gold province, South-West Greenland: a genetic model for prograde metamorphism of orogenic gold deposits*. 11th SGA Biennial Meeting, Antofagasta, Chile, September 2011. Extended abstract.
- Kokfelt, T.F., Keulen, N., Næraa, T., Scherstén, A. and Heijboer, T., 2011. New zircon U/Pb age data from the Archaean craton, South-West and southern West Greenland (61°30'N - 64°00'N) EGU2011-14038.
- Kusky, T.M. and Polat, A. 1999. Growth of granite-greenstone terranes at convergent margins, and stabilization of Archean cratons. *Tectonophysics* **305**, 43-73.
- Lahaye, Y., Arndt, N.T., Byerly, G., Gruau, G., Fourcade S. and Chauvel, C., 1995. The influence of alteration on the trace-element and Nd isotope compositions of komatiites. *Chemical Geology* **126**, 43-64.
- Laurie, A., Stevens, G., 2010. *Growth of early continental crust by water-present eclogite melting*, 5th IAS meeting, Perth, Australia.
- Laurie, A., Stevens, G., 2012. Water-present eclogite melting to produce Earth's early felsic crust. *Chemical Geology* (accepted).
- Le Bas, M.J. Le Maitre, R.W., Streckeisen, A. and Zanettin, B. 1986. A chemical classification of volcanic rocks based on the total alkali-silica diagram *Journal of Petrology* **27**, 745-750.
- Le Maitre, R.W., 2002. *A Classification of Igneous Rocks and Glossary of Terms*. 2nd Edition. Blackwell Scientific Publications, Oxford. 236 pp.
- Leshner, C.M., Burnham, O.M., Keays, R.R., Barnes, S. Stephen, J. and Hulbert, L., 2001. Geochemical discrimination of barren and mineralized komatiites associated with magmatic Ni-Cu-(PGE) sulphide deposits. *Canadian Mineralogist* **39**, 673-696.
- Martin, H., Smithies, R.H., Rapp, R., Moyen, J.-F. and Champion, D. 2005. An overview of adakite, tonalite-trondhjemite-granodiorite (TTG), and sanukitoid: relationship and some implications for crustal evolution. *Lithos* **79**, 1-24.
- McGregor, V.R. and Friend, C.R.L. 1997. Field recognition of rocks totally retrogressed from granulite facies: an example from Archaean rocks in the Paamiut region, South-West Greenland. *Precambrian Research* **86**, 59-70.
- McDonough, W. F. and Sun, S., 1995. The composition of the Earth. *Chemical Geology* **120**, 223-253.
- Nilsson, M.K.M., Söderlund, U., Ernst R.E. and Hamilton, M.A., 2010. Precise U–Pb baddeleyite ages of mafic dykes and intrusions in southern West Greenland and implications for a possible reconstruction with the Superior craton. *Precambrian Research* **183**, 399-415.
- Nutman, A.P. and Friend, C.R.L. 2007. Adjacent terranes with c. 2715 and 2650 Ma high pressure metamorphic assemblages in the Nuuk region of the North Atlantic craton, southern West Greenland: complexities of Neoarchaean collisional orogeny. *Precambrian Research* **155**, 159–203.
- Nutman, A.P., Friend, C.R.L., Baadsgaard, H., and McGregor, V.R. 1989. Evolution and assembly of Archaean gneiss terranes in the Godthåbs-fjord region, southern West Greenland: structural, metamorphic and isotopic evidence. *Tectonics* **8**, 573–589.
- Nutman, A.P., Friend, C.R.L., Barker, S.L.L. and McGregor, V.R. 2004. Inventory and assessment of Palaeoarchaean gneiss terrains and detrital zircons in southern West Greenland. *Precambrian Research* **135**, 281-314.
- Ohta, T. and Arai H. 2007. Statistical empirical index of chemical weathering in igneous rocks: A new tool for evaluating the degree of weathering. *Chemical Geology* **240**, 280-297.
- Parman, S., Grove, T.L., Dann, J. and de Wit, M.J., 2004. A subduction origin for komatiites and cratonic lithospheric mantle. *South African Journal of Geology* **107**, 107-118.
- Pidgeon, R.T. and Kalsbeek, F., 1978. Dating of igneous and metamorphic events in the Fiske-naesset region of southern west Greenland. *Canadian Journal of Earth Sciences*, 2021-2025.
- Polat, A., Frei, R., Appel, P.W.U., Fryer, B. and Ordóñez-Calderón, J.C., 2008. An overview of the lithological and geochemical characteristics of the Mesoarchaean (ca. 3075 Ma)

- Ivisaartoq greenstone belt, southern West Greenland. In: Condie, K.C., Pease, V. (eds.), When did plate tectonics begin on planet Earth? *Geological Society of America, Special Paper* **440**, 51-76.
- Polat, A., Appel, P.W.U., Fryer, B., Windley, B., Frei, R., Samson, I.M. and Huang, H. 2009: Trace element systematics of the Neoarchean Fiskenæsset anorthosite complex and associated meta-volcanic rocks, SW Greenland: Evidence for a magmatic arc origin. *Precambrian Research* **175**, 87-115.
- Polat, A., Appel, P.W.U. and Fryer, B.J., 2011. An overview of the geochemistry of Eoarchean to Mesoarchean ultramafic to mafic volcanic rocks, SW Greenland: Implications for mantle depletion and petrogenetic processes at subduction zones in the early Earth. *Gondwana Research* **20**, 255-283.
- Puchtel, J.S., Arndt, N.T., Hofmann, A.W., Haase, K.M., Kröner, A., Kulikov, V.S., Kulikova, V.V., Garbe-Schönberg, C.-D. and Nemchin, A.A., 1998. Petrology of mafic lavas within the Onega plateau, central Karelia: evidence for the 2.0 Ga plume-related continental crustal growth in the Baltic Shield. *Contributions to Mineralogy and Petrology* **130**, 134-153.
- Rapp, R.P., Watson, E.B and Miller, C.F, 1991. Partial melting of amphibolite/eclogite and the origin of Archean trondhjemites and tonalites. *Precambrian Research* **51**, 1-25.
- Roeder, P.L. and Emslie, R.F. 1970. Olivine-liquid equilibrium. *Contribution to Mineralogy and Petrology* **29**, 275-289.
- Rollinson, H.R. 1993. *Using geochemical data: evaluation, presentation, interpretation*. Longman, UK. 352 pp.
- Said, N., Kerrich, R., Groves, D., 2010. Geochemical systematics of basalts of the Lower Basalt Unit, 2.7 Ga Kambalda Sequence, Yilgarn craton, Australia: plume impingement at a rifted craton margin. *Lithos* **115**, 82-100.
- Saunders A.D., Norry M.J., Tarney J., 1991. Fluid influence on the trace element composition of subduction zone magmas. *Philosophical Transactions of the Royal Society, London* **A335**, 377-392.
- Scherstén, A. and Stendal, H., 2008. Geochemistry of the Tasiusarsuaq 'greenstone-granite' terrane, southern West Greenland. *Danmarks og Grønlands Geologiske Undersøgelse Rapport* **2008/15**, 40 pp.
- Schumacher, J.C., van Hinsberg, V.J. and Keulen, N. 2011 Metamorphism in supracrustal and ultramafic rocks in southern West Greenland and South-West Greenland 64-61.5 °N. *Geological Survey of Denmark and Greenland Report* **2011/06**, 29 pp.
- Springer, W. and Seck, H.A., 1997. Partial fusion of basic granulites at 5 to 15 kbar: implications for the origin of TTG magmas. *Contribution to Mineralogy and Petrology* **127**, 30-45.
- Sproule, R.A., Leshner, C.M., Ayer, J.A., Thurston, P.C. and Herzberg, C.T. 2002. Spatial and Temporal Variations in the Geochemistry of Komatiitic Basalts in the Abitibi Greenstone Belt. *Precambrian Research* **115**, 163-188.
- Sun, S. and McDonough, W. F. 1989. Chemical and Isotopic Systematics of Oceanic Basalts: Implications for Mantle Composition and Processes. In A.D. Saunders and M.J. Norry (editors.) *Magmatism in the Ocean Basins. Special Publication from the Geological Society of London* **42**, 313-345.
- Szilas, K., 2012. *Geochemistry of Archaean supracrustal belts in SW Greenland*. Unpublished PhD thesis. University of Copenhagen.
- Szilas, K., Kokfelt, T.F., Næraa, T. and Scherstén, A. 2011a. Geochemistry of Archaean felsic crust in SW Greenland. In: Kokfelt, T.F. (ed.). *Geochemistry of supracrustal rocks and associated intrusive TTG suites of the Archaean craton in South-West Greenland and southern West Greenland, 61°30' - 64°N. Geological Survey of Denmark and Greenland Report* **2011/10**.
- Szilas, K., Van Hinsberg, J., Kisters, A.F.M., Hoffmann, E.J., Kokfelt, T.F., Scherstén, A., Windley, B.F., Frei, R., Rosing, M.T., Münker, C., 2011b. Remnants of arc-related Mesoarchean oceanic crust in the Tartoq Group, SW Greenland. *Gondwana Research* **10.1016/j.gr.2011.11.006**.
- Szilas, K., Hoffmann, J.E., Scherstén, A., Rosing, M.T., Windley, B.F., Kokfelt, T.F., Keulen, N., Van Hinsberg, V.J., Næraa, T., Frei, R., Münker, C., 2012a. Complex calc-alkaline volcanism recorded in Mesoarchean supracrustal belts north of Frederiksbhåbs Isblink, southern West Greenland: implications for subduction zone processes in the early Earth. *Precambrian Research* doi:10.1016/j.precamres.2012.03.013

- Szilas, K., Næraa, T., Scherstén, A., Stendal, H., Frei, R., Van Hinsberg, V., Kokfelt, T.F. and Rosing, M. 2012b. Origin of arc related rocks with boninite/komatiite affinities from southern West Greenland. *Lithos* doi: 10.1016/j.lithos.2012.03.023.
- Tomlinson, K.Y., Hughes, D.J., Thurston, P.C., and Hall, R.P., 1999. Plume magmarism and crustal growth at 2.9 to 3.0 Ga in the Steep Rock and Lumby Lake area, western Superior province: *Lithos* **46**, 103-136.
- Tullis J. and Yund, R.A. 1977. Experimental deformation of dry Westerly Granite. *Journal of Geophysical Research* **82**, 5705-5718.
- Ulmer P. and Müntener O. 2005. "Adakites" formed by Garnet Fractionation at the Base of the Crust – An alternative Scenario supported by Field and Experimental Data. *Geophysical Research Abstracts* **7**, 09837. SRef-ID: 1607-7962/gra/EGU05-A-09837
- van Hunen, J., Keken, P.E., Hynes, A. and Davies, G. 2008. Tectonics of early Earth: Some geodynamic considerations. *Geological society of America, Special paper* **440**, 157-171.
- van Keken, P.E. and King, S.D., 2004. Thermal structure and dynamics of subductions zones: insights from observations and modelling. *Phys. Earth Planet. Interior* **149**, 1-6.
- Wells, P.R.A., 1976. Late Archean metamorphism in the Buksefjorden region, Southwest Greenland. *Contributions to Mineralogy and Petrology* **56**, 229-242.
- Windley, B.F. 1966: Anorthosites and polymetamorphism between Ravns Storø and Sukkertoppen, West Greenland. *Grønlands Geologiske Undersøgelser Rapport* **11**, 27-29.
- Windley, B. and Garde, A.A., 2009. Arc-generated blocks with sections in the North Atlantic craton of West Greenland: Crustal growth in the Archean with modern analogues. *Earth-Science Reviews* **93**, 1-30.
- Wood, D.A. 1980. The application of a Th–Hf–Ta diagram to problems of tectonomagmatic classification and to establishing the nature of crustal contamination of basaltic lavas of the British Tertiary volcanic province. *Earth and Planetary Science Letters* **50**, 11–30.
- Xie, Q. and Kerrich, R. 1994. Silicate-perovskite and majorite signature komatiites from Archean Abitibi Belt: Implications for early mantle differentiation and stratification: *Journal of Geophysical Research* **99**, 15,799-15,812.
- Zegers, T.E. and van Keken, P.E., 2001. Middle Archean continent formation by crustal delamination. *Geology* **29**, 1083–1086.

Appendices

Appendix 1: Zircon U/Pb age data for felsic sheets and TTG rocks at Ni-gerlikasik supracrustal sequence

Table 2. Zircon U/Pb data on felsic sheets and TTG samples from the Nigaiikasik profile, Kvanefjord area

Sample	Analysis	U (ppm) ^a	ThU ^a	RATIOS						AGES [Ma]				Conc.			
				²⁰⁷ Pb/ ²³⁵ U	2 σ ^a	²⁰⁶ Pb/ ²³⁸ U ^b	2 σ ^a	rho ^c	²⁰⁷ Pb/ ²⁰⁶ Pb ^a	2 σ ^a	²⁰⁷ Pb/ ²³⁵ U	2 σ ^a	²⁰⁶ Pb/ ²³⁸ U		2 σ ^a	%	
519629																	
519626	Zircon_sample-007	172	0.38	14.86	0.86	0.51	0.03	0.89	0.213	0.006	2806	55	2636	111	2931	43	90
519629	Zircon_sample-008	82	0.49	15.81	0.73	0.55	0.02	0.85	0.209	0.005	2865	44	2818	89	2898	40	97
519629	Zircon_sample-009	51	0.50	17.08	1.08	0.57	0.03	0.89	0.218	0.008	2938	80	2916	130	2953	48	99
519628	Zircon_sample-010	117	0.80	18.01	0.98	0.54	0.03	0.90	0.215	0.008	2877	59	2782	125	2944	43	94
519628	Zircon_sample-014	83	0.48	15.89	1.15	0.53	0.04	0.81	0.214	0.008	2858	70	2750	150	2935	48	94
519628	Zircon_sample-020	95	0.38	15.30	0.89	0.52	0.01	0.81	0.212	0.008	2834	43	2712	81	2922	58	93
519629	Zircon_sample-022	65	0.37	16.21	0.86	0.56	0.03	0.88	0.212	0.005	2889	51	2849	108	2917	41	98
519629	Zircon_sample-025	102	0.44	15.99	0.47	0.55	0.01	0.88	0.212	0.003	2876	28	2811	59	2921	22	98
519629	Zircon_sample-033	132	1.35	15.50	0.55	0.53	0.02	0.81	0.212	0.004	2948	34	2748	64	2918	34	94
519628	Zircon_sample-038	64	0.53	15.01	0.79	0.51	0.02	0.88	0.212	0.005	2819	50	2678	102	2917	40	92
519629	Zircon_sample-040	90	0.34	15.14	0.62	0.52	0.02	0.97	0.213	0.002	2824	39	2890	87	2928	15	92
519628	Zircon_sample-040	80	0.78	15.92	1.22	0.54	0.04	0.88	0.212	0.008	2872	73	2800	154	2923	58	98
519628	Zircon_sample-041	323	0.40	15.98	0.88	0.56	0.02	0.80	0.208	0.007	2876	52	2878	102	2875	54	100
519629	Zircon_sample-046	109	0.48	16.49	0.81	0.57	0.00	0.21	0.209	0.008	2906	35	2915	18	2999	58	101
519629	Zircon_Sample-048	87	1.12	15.04	0.72	0.51	0.02	0.85	0.213	0.005	2818	48	2871	88	2925	41	91
519628	Zircon_Sample-050	66	0.43	14.91	0.58	0.53	0.02	0.87	0.204	0.004	2809	37	2747	75	2855	32	96
519628	Zircon_Sample-051	58	0.47	16.81	0.62	0.57	0.03	0.85	0.212	0.008	2913	53	2900	109	2921	47	98
519628	Zircon_Sample-054	44	0.48	16.33	0.82	0.55	0.02	0.80	0.215	0.008	2886	48	2831	62	2942	49	98
519628	Zircon_Sample-059	131	0.58	16.23	0.75	0.55	0.02	0.80	0.215	0.004	2860	44	2811	65	2946	34	95
519628	Zircon_Sample-060	28	0.63	15.44	0.60	0.53	0.02	0.87	0.211	0.004	2843	37	2749	75	2910	31	94
519629	Zircon_Sample-061	89	0.44	15.49	0.89	0.52	0.03	0.90	0.214	0.005	2846	56	2720	115	2938	41	93
519628	Zircon_Sample-062	35	0.85	15.16	1.29	0.54	0.04	0.95	0.208	0.008	2825	81	2763	182	2871	44	96
519628	Zircon_Sample-064	52	0.48	16.42	0.89	0.58	0.03	0.85	0.212	0.008	2902	52	2870	107	2924	47	98
519628	Zircon_Sample-072	107	0.47	13.02	0.77	0.49	0.03	0.97	0.192	0.003	2881	58	2582	123	2758	24	94
519628	Zircon_Sample-075	88	0.49	16.82	1.72	0.57	0.05	0.91	0.211	0.009	2913	100	2912	221	2914	69	100
519628	Zircon_Sample-076	108	0.48	16.00	0.79	0.54	0.02	0.78	0.215	0.007	2877	47	2782	87	2943	49	95
519628	Zircon_Sample-088	84	0.42	15.13	1.48	0.54	0.05	0.93	0.203	0.007	2823	93	2788	206	2849	58	98
519629	Zircon_Sample-089	37	0.56	15.20	0.29	0.52	0.01	0.86	0.214	0.002	2828	18	2879	38	2936	10	91
519629	Zircon_Sample-090	211	0.73	13.97	1.28	0.55	0.05	0.90	0.185	0.007	2748	87	2817	188	2898	66	104
519628	Zircon_Sample-093	37	0.48	15.88	1.38	0.58	0.04	0.87	0.204	0.009	2857	84	2858	178	2855	72	100
519628	Zircon_Sample-100	84	0.47	15.88	1.28	0.58	0.04	0.97	0.213	0.004	2858	77	2752	175	2831	31	94
519628	Zircon_Sample-106	141	0.30	14.27	0.98	0.53	0.03	0.95	0.194	0.004	2768	85	2755	145	2777	35	98
519628	Zircon_Sample-108	92	0.41	15.23	0.70	0.51	0.02	0.94	0.215	0.003	2830	44	2878	95	2941	26	91
519628	Zircon_Sample-113	148	0.38	14.05	1.19	0.53	0.04	0.92	0.194	0.006	2753	80	2722	173	2778	53	98
519628	Zircon_Sample-115	214	0.19	15.41	0.84	0.53	0.02	0.92	0.210	0.003	2841	40	2748	88	2908	27	95
519628	Zircon_Sample-117	381	0.48	16.68	0.54	0.57	0.02	0.68	0.213	0.004	2917	31	2900	64	2928	27	98
519628	Zircon_Sample-126	80	0.34	15.25	0.37	0.51	0.01	0.86	0.218	0.003	2831	23	2886	45	2951	20	90
519628	Zircon_Sample-128	65	0.44	16.83	0.42	0.57	0.01	0.79	0.214	0.003	2831	24	2828	48	2934	25	100
519628	Zircon_Sample-131	39	0.55	16.37	0.44	0.55	0.01	0.64	0.217	0.005	2868	26	2809	39	2981	34	95
519629	Zircon_Sample-137	119	0.58	15.00	0.49	0.51	0.02	0.91	0.211	0.003	2815	31	2876	85	2918	22	92
519628	Zircon_Sample-140	89	0.41	16.51	0.28	0.58	0.01	0.81	0.218	0.002	2907	18	2848	31	2948	16	97
519629	Zircon_Sample-141	62	0.58	16.90	0.45	0.58	0.01	0.89	0.211	0.003	2929	25	2948	56	2918	19	101
519628	Zircon_Sample-142	92	0.36	17.11	0.39	0.58	0.01	0.84	0.211	0.003	2941	22	2878	45	2917	20	102
519628	Zircon_Sample-143	369	0.38	15.81	0.40	0.55	0.01	0.81	0.205	0.002	2853	24	2833	53	2887	17	98
519628	Zircon_Sample-144	115	0.53	15.91	0.42	0.54	0.01	0.80	0.212	0.003	2872	25	2799	48	2923	26	98
519628	Zircon_Sample-150	86	0.32	16.71	0.36	0.57	0.01	0.89	0.213	0.002	2918	21	2889	45	2932	18	98
519628	Zircon_Sample-151	125	0.48	15.39	0.76	0.52	0.02	0.89	0.215	0.005	2840	47	2891	87	2947	36	91
519629	Zircon_Sample-158	323	0.52	13.49	0.84	0.48	0.02	0.98	0.198	0.003	2715	45	2591	96	2808	23	92
519851																	
519851	Zircon_sample-007	157	0.35	16.46	0.37	0.56	0.01	0.83	0.213	0.003	2905	22	2872	44	2928	20	98
519851	Zircon_sample-008	109	0.52	19.41	0.40	0.56	0.01	0.83	0.212	0.003	2901	23	2875	47	2919	22	98
519851	Zircon_sample-008	42	0.48	19.23	0.42	0.55	0.01	0.81	0.213	0.003	2881	25	2834	49	2930	25	97
519851	Zircon_sample-010	168	0.48	16.51	0.80	0.57	0.03	0.85	0.211	0.003	2907	48	2901	107	2911	24	100
519851	Zircon_sample-011	148	0.37	16.48	0.44	0.58	0.01	0.80	0.210	0.003	2904	25	2869	49	2928	26	98
519851	Zircon_sample-012	33	0.68	12.72	0.80	0.43	0.02	0.62	0.210	0.004	2629	48	2283	86	2807	31	79
519851	Zircon_sample-013	64	0.58	12.68	0.44	0.43	0.01	0.90	0.214	0.003	2656	33	2307	61	2833	25	79
519851	Zircon_sample-014	123	0.35	16.63	0.71	0.57	0.02	0.85	0.213	0.005	2914	41	2889	84	2931	36	98
519851	Zircon_sample-015	142	0.76	17.08	0.95	0.58	0.02	0.77	0.214	0.008	2938	54	2944	101	2935	58	100
519851	Zircon_sample-021	119	0.53	16.73	0.85	0.58	0.02	0.78	0.210	0.007	2919	48	2938	84	2908	52	101
519851	Zircon_sample-022	132	0.50	17.13	0.77	0.59	0.02	0.74	0.212	0.008	2942	43	2969	79	2924	48	102
519851	Zircon_sample-023	100	0.18	14.20	0.56	0.49	0.01	0.78	0.211	0.005	2783	37	2591	65	2914	38	88
519851	Zircon_sample-024	148	0.32	14.48	1.10	0.50	0.03	0.77	0.209	0.010	2781	72	2620	125	2901	79	90
519851	Zircon_sample-025	109	0.44	17.04	0.57	0.57	0.02	0.84	0.216	0.004	2937	32	2913	66	2953	26	98
519851	Zircon_sample-027	77	0.35	16.13	0.98	0.55	0.03	0.82	0.212	0.007	2885	57	2834	112	2920	56	97
519851	Zircon_sample-028	611	0.55	16.86	0.59	0.58	0.02	0.97	0.209	0.002	2927						

Table 2. continued

Sample	Analysis	U [ppm] ^a	ThU ^b	RATIOS							AGES [Ma]						Conc. %
				²⁰⁷ Pb/ ²³⁵ U	2 σ ^a	²⁰⁶ Pb/ ²³⁸ U	2 σ ^a	Th/ ²³² Th	²⁰⁷ Pb/ ²⁰⁶ Pb	2 σ ^a	²⁰⁷ Pb/ ²³⁵ U	2 σ	²⁰⁶ Pb/ ²³⁸ U	2 σ	²⁰⁷ Pb/ ²⁰⁶ Pb	2 σ	
519651, continued																	
519651	Zircon_Sample-087	209	0.34	16.38	0.98	0.56	0.03	0.92	0.211	0.005	2899	57	2877	128	2915	38	99
519651	Zircon_Sample-088	285	0.56	16.67	0.60	0.56	0.02	0.83	0.212	0.004	2928	34	2940	70	2919	32	101
519651	Zircon_Sample-089	209	0.38	16.81	1.14	0.57	0.04	0.96	0.214	0.004	2930	85	2919	153	2937	29	99
519651	Zircon_Sample-090	153	0.57	17.56	0.73	0.60	0.02	0.88	0.213	0.004	2886	40	3019	89	2831	30	103
519651	Zircon_Sample-091	442	0.43	17.05	0.61	0.59	0.02	0.77	0.210	0.005	2938	35	2982	66	2906	37	103
519651	Zircon_Sample-092	58	0.69	12.38	1.00	0.42	0.03	0.93	0.216	0.006	2935	76	2241	141	2953	48	76
519651	Zircon_Sample-093	132	0.33	17.51	0.99	0.59	0.03	0.91	0.217	0.005	2963	54	2973	123	2957	37	101
519651	Zircon_Sample-099	335	0.64	17.10	0.78	0.58	0.02	0.80	0.213	0.006	2940	44	2963	86	2925	45	101
519651	Zircon_Sample-101	109	0.42	15.39	0.93	0.51	0.03	0.90	0.217	0.006	2839	58	2875	119	2959	42	90
519651	Zircon_Sample-102	298	0.44	16.06	0.85	0.54	0.02	0.75	0.215	0.007	2882	51	2794	91	2943	56	95
519651	Zircon_Sample-104	751	0.16	11.22	0.72	0.43	0.02	0.87	0.188	0.006	2542	80	2320	109	2724	62	85
519651	Zircon_Sample-106	892	0.13	14.87	0.94	0.56	0.03	0.91	0.194	0.005	2907	50	2853	132	2774	44	103
519651	Zircon_Sample-111	110	0.44	17.02	0.70	0.58	0.02	0.90	0.214	0.004	2936	40	2940	88	2933	29	100
519651	Zircon_Sample-112	196	0.84	16.66	0.56	0.57	0.01	0.78	0.212	0.004	2917	32	2906	61	2924	34	99
519651	Zircon_Sample-113	107	0.22	15.84	1.11	0.57	0.03	0.81	0.201	0.008	2887	87	2919	133	2832	87	103
519651	Zircon_Sample-114	233	0.59	17.31	0.88	0.60	0.03	0.88	0.209	0.005	2952	49	3028	108	2900	39	104
519651	Zircon_Sample-117	87	0.42	14.96	1.06	0.52	0.04	0.97	0.209	0.004	2813	68	2899	152	2885	28	93
519651	Zircon_Sample-119	85	0.42	15.52	0.66	0.53	0.01	0.65	0.211	0.007	2848	40	2756	82	2914	52	95
519651	Zircon_Sample-124	117	0.30	15.72	0.96	0.56	0.03	0.82	0.203	0.007	2860	58	2872	116	2851	57	101
519651	Zircon_Sample-126	97	0.51	16.57	0.73	0.57	0.02	0.90	0.211	0.004	2911	42	2902	62	2916	32	100
519651	Zircon_Sample-128	74	0.61	17.11	0.81	0.60	0.03	0.94	0.209	0.003	2941	46	3010	107	2894	27	104
519651	Zircon_Sample-129	867	0.33	11.20	0.84	0.44	0.03	0.85	0.196	0.007	2540	70	2340	125	2703	68	87
519651	Zircon_Sample-130	608	0.84	10.18	0.55	0.38	0.01	0.73	0.193	0.007	2451	50	2090	70	2788	80	76
519651	Zircon_Sample-131	177	0.61	17.49	0.85	0.60	0.02	0.86	0.212	0.005	2982	46	3020	100	2923	40	103
519651	Zircon_Sample-143	118	0.37	17.53	0.75	0.58	0.02	0.74	0.218	0.006	2984	41	2965	78	2953	46	100
519651	Zircon_Sample-144	134	0.82	17.31	0.76	0.59	0.02	0.89	0.211	0.004	2952	42	3007	94	2915	33	103
519651	Zircon_Sample-145	195	0.28	15.99	0.85	0.57	0.03	0.89	0.202	0.005	2878	51	2924	111	2842	39	103
519651	Zircon_Sample-152	323	0.13	11.15	0.48	0.42	0.02	0.95	0.193	0.003	2536	40	2257	77	2767	22	82
519651	Zircon_Sample-153	145	0.70	16.94	0.95	0.57	0.02	0.72	0.214	0.008	2931	54	2925	85	2908	63	100
519651	Zircon_Sample-154	209	0.35	17.41	1.01	0.60	0.03	0.80	0.210	0.007	2958	56	3041	112	2902	58	105
519651	Zircon_Sample-155	114	0.89	17.18	0.89	0.58	0.03	0.90	0.214	0.005	2945	50	2958	111	2937	37	101
519651	Zircon_Sample-156	71	0.48	15.19	1.07	0.54	0.03	0.90	0.205	0.006	2827	57	2769	143	2869	50	96
519651	Zircon_Sample-157	51	0.58	16.94	1.27	0.58	0.03	0.77	0.213	0.010	2932	72	2934	138	2930	77	100
519651	Zircon_Sample-158	110	0.50	17.38	0.65	0.58	0.02	0.87	0.214	0.002	2968	38	2988	88	2934	16	102
519677																	
519677	Zircon_Sample-164	212	0.34	17.24	1.04	0.60	0.04	0.97	0.209	0.003	2949	58	3027	141	2896	25	105
519677	Zircon_Sample-165	153	0.87	16.83	0.44	0.58	0.01	0.88	0.210	0.003	2914	25	2931	53	2902	21	101
519677	Zircon_Sample-166	161	0.34	15.91	1.41	0.54	0.05	0.96	0.214	0.005	2871	85	2783	193	2934	38	95
519677	Zircon_Sample-167	82	1.68	16.94	1.34	0.58	0.04	0.88	0.213	0.003	2932	76	2941	184	2925	22	101
519677	Zircon_Sample-171	179	0.42	16.87	0.85	0.58	0.02	0.70	0.210	0.008	2927	48	2962	84	2904	58	102
519677	Zircon_Sample-172	195	0.65	17.16	0.84	0.59	0.03	0.96	0.210	0.003	2944	47	2968	113	2907	22	103
519677	Zircon_Sample-177	159	0.47	15.46	0.80	0.53	0.02	0.86	0.210	0.006	2844	49	2757	100	2905	43	95
519677	Zircon_Sample-181	123	0.37	15.24	1.37	0.53	0.04	0.94	0.210	0.007	2831	86	2725	187	2906	50	94
519677	Zircon_Sample-183	80	1.08	16.10	1.13	0.58	0.04	0.96	0.207	0.004	2883	67	2879	155	2885	33	100
519677	Zircon_Sample-198	111	0.29	13.64	0.93	0.48	0.03	0.90	0.208	0.008	2725	84	2524	128	2878	47	88
519677	Zircon_Sample-197	276	0.44	16.90	1.56	0.58	0.05	0.97	0.208	0.005	2912	90	2935	215	2867	38	101
519677	Zircon_Sample-207	196	0.63	17.00	1.08	0.58	0.03	0.86	0.211	0.007	2935	61	2961	130	2976	52	102
519677	Zircon_Sample-209	362	0.79	14.18	0.96	0.53	0.03	0.94	0.192	0.004	2762	64	2762	142	2762	38	100
519677	Zircon_Sample-211	38	0.78	13.95	0.87	0.48	0.03	0.96	0.211	0.004	2747	59	2529	125	2910	29	87
519677	Zircon_Sample-212	212	0.59	13.66	0.82	0.48	0.03	0.89	0.207	0.006	2726	57	2518	111	2884	45	87
519677	Zircon_Sample-213	87	0.80	15.48	0.72	0.52	0.02	0.89	0.215	0.005	2845	45	2709	92	2943	35	92
519677	Zircon_Sample-218	294	0.33	15.55	1.28	0.54	0.04	0.90	0.207	0.007	2850	78	2864	168	2882	57	97
519677	Zircon_Sample-220	194	1.16	15.29	0.95	0.53	0.03	0.87	0.209	0.006	2834	59	2745	120	2867	50	95
519677	Zircon_Sample-222	83	0.44	13.70	1.07	0.48	0.03	0.95	0.215	0.005	2730	74	2450	151	2943	40	83
519677	Zircon_Sample-228	167	0.48	17.64	1.60	0.61	0.05	0.93	0.210	0.007	2970	88	3061	208	2909	53	105
519677	Zircon_Sample-231	127	0.51	17.46	0.79	0.59	0.02	0.75	0.213	0.008	2981	44	3008	82	2929	49	103
519677	Zircon_Sample-234	47	0.51	17.43	1.17	0.60	0.04	0.98	0.212	0.002	2958	85	3016	160	2921	16	103
519677	Zircon_Sample-238	136	1.09	15.86	0.56	0.55	0.02	0.87	0.209	0.004	2870	34	2828	70	2889	28	98
519677	Zircon_Sample-244	69	1.43	14.05	1.14	0.50	0.04	0.97	0.211	0.004	2793	74	2527	163	2914	28	98
519677	Zircon_Sample-245	110	0.54	15.39	1.17	0.55	0.04	0.93	0.203	0.006	2840	73	2820	161	2853	47	99
519677	Zircon_Sample-246	135	0.38	15.24	1.12	0.52	0.04	0.93	0.211	0.006	2830	70	2714	151	2914	45	93
519677	Zircon_Sample-249	96	0.42	14.70	0.91	0.50	0.03	0.90	0.212	0.008	2796	59	2830	120	2916	45	90
519677	Zircon_Sample-250	136	0.57	16.40	1.35	0.57	0.04	0.88	0.208	0.008	2900	79	2900	172	2901	60	100
519677	Zircon_Sample-251	221	0.85	17.20	1.44	0.60	0.04	0.84	0.209	0.010	2946	61	3018	189	2886	74	104
519677	Zircon_Sample-252	7	0.56	16.61	1.00	0.58	0.03	0.84	0.209	0.007	29						

Table 2. continued

Sample	Analysis	U [ppm] ^a	Th/U ^a	RATIOS						AGES [Ma]						Conc. %	
				²⁰⁷ Pb/ ²³⁵ U	2 σ ^b	²⁰⁶ Pb/ ²³⁸ U	2 σ ^b	rho ^c	2 σ ^b	²⁰⁷ Pb/ ²⁰⁶ Pb	2 σ ^b	²⁰⁷ Pb/ ²³⁸ U	2 σ ^b	²⁰⁶ Pb/ ²³⁸ U	2 σ ^b		²⁰⁶ Pb/ ²⁰⁷ Pb
519696, continued																	
519696	Zircon_sample-026	382	0.33	11.29	0.46	0.39	0.01	0.91	0.212	0.004	2547	36	2108	66	2919	27	72
519696	Zircon_sample-028	107	0.41	14.65	0.57	0.50	0.02	0.92	0.212	0.003	2792	37	2823	77	2918	25	90
519696	Zircon_sample-033	225	0.82	18.28	0.84	0.55	0.03	0.89	0.213	0.005	2863	50	2942	106	2929	38	97
519696	Zircon_sample-034	183	0.50	15.42	0.67	0.52	0.02	0.82	0.215	0.005	2841	35	2898	68	2948	34	82
519696	Zircon_sample-035	80	0.42	17.19	0.84	0.58	0.03	0.97	0.216	0.002	2946	47	2940	112	2949	18	100
519696	Zircon_sample-038	193	0.36	17.10	1.32	0.58	0.04	0.98	0.213	0.004	2940	74	2953	179	2931	27	101
519696	Zircon_sample-040	122	0.40	16.77	0.30	0.37	0.00	0.44	0.214	0.003	2922	17	2897	18	2939	26	99
519696	Zircon_sample-041	101	0.28	12.02	0.35	0.40	0.01	0.87	0.218	0.003	2806	27	2185	46	2869	23	73
519696	Zircon_sample-047	77	0.51	16.73	0.72	0.37	0.02	0.82	0.213	0.005	2920	41	2902	82	2922	40	96
519696	Zircon_sample-050	43	0.72	16.62	1.17	0.57	0.03	0.85	0.213	0.006	2925	67	2916	139	2933	59	100
519696	Zircon_sample-053	423	0.30	15.83	0.48	0.54	0.01	0.73	0.213	0.004	2866	26	2789	50	2928	34	95
519696	Zircon_sample-054	522	0.15	12.17	1.00	0.42	0.03	0.99	0.212	0.003	2817	77	2241	153	2923	23	77
519696	Zircon_sample-059	904	0.54	14.24	0.73	0.49	0.02	0.95	0.211	0.003	2766	48	2570	102	2912	27	88
519696	Zircon_sample-062	179	-2.10	14.24	1.38	0.48	0.05	0.98	0.213	0.004	2796	92	2548	201	2928	28	87
519696	Zircon_sample-063	54	0.61	14.81	0.95	0.50	0.03	0.91	0.213	0.006	2803	61	2833	126	2928	43	90
519696	Zircon_sample-065	456	0.72	14.83	0.85	0.51	0.03	0.92	0.211	0.005	2811	54	2912	115	2912	35	82
519696	Zircon_sample-067	611	0.51	17.38	1.18	0.60	0.04	0.92	0.211	0.006	2956	65	3079	151	2914	43	104
519696	Zircon_sample-077	53	0.54	16.84	1.16	0.58	0.04	0.95	0.211	0.004	2931	66	2957	154	2914	34	101
519696	Zircon_sample-079	195	0.52	16.55	0.60	0.57	0.02	0.88	0.212	0.005	2909	46	2994	99	2919	38	99
519696	Zircon_sample-080	296	0.55	17.49	0.70	0.59	0.02	0.96	0.215	0.002	2962	39	2994	93	2941	17	102
519696	Zircon_sample-085	103	0.48	17.20	0.67	0.58	0.02	0.80	0.213	0.006	2946	49	2967	86	2922	48	101
519696	Zircon_sample-089	510	0.57	17.19	0.94	0.59	0.03	0.89	0.213	0.005	2948	52	2971	118	2929	40	101
519696	Zircon_sample-090	278	0.40	15.67	0.55	0.54	0.02	0.99	0.214	0.003	2869	33	2777	70	2934	25	95
519696	Zircon_sample-091	294	0.42	17.71	0.45	0.60	0.01	0.92	0.215	0.002	2974	24	3015	66	2947	16	102
519696	Zircon_sample-093	207	0.33	16.58	0.52	0.36	0.02	0.89	0.215	0.003	2911	30	2822	64	2945	23	97
519696	Zircon_sample-098	228	0.35	15.07	0.25	0.51	0.01	0.80	0.214	0.002	2819	16	2882	29	2934	16	91
519696	Zircon_sample-100	963	0.58	17.24	1.05	0.58	0.03	0.88	0.213	0.007	2948	58	2974	124	2931	51	101
519696	Zircon_sample-102	878	0.50	10.03	0.65	0.38	0.02	0.98	0.200	0.002	2437	60	2003	110	2822	19	71
519696	Zircon_sample-103	222	0.51	17.25	1.84	0.60	0.06	0.96	0.210	0.006	2956	102	3033	245	2964	50	104
519696	Zircon_sample-104	338	0.53	15.34	0.61	0.52	0.02	0.96	0.214	0.002	2837	38	2703	64	2933	17	92
519696	Zircon_sample-106	236	0.54	15.70	0.85	0.54	0.02	0.92	0.211	0.004	2859	40	2777	66	2917	27	95
519696	Zircon_sample-111	170	0.60	15.63	0.63	0.53	0.02	0.71	0.213	0.006	2854	38	2747	64	2911	46	94
519696	Zircon_sample-112	490	0.31	16.08	0.70	0.56	0.02	0.91	0.207	0.004	2890	42	2873	92	2885	30	100
519696	Zircon_sample-113	149	0.42	16.72	0.79	0.59	0.03	0.97	0.218	0.002	2919	46	2974	107	2950	18	97
519696	Zircon_sample-114	486	0.29	17.03	0.68	0.58	0.02	0.81	0.211	0.005	2936	38	2968	77	2915	38	102
519696	Zircon_sample-115	359	0.52	16.61	0.97	0.57	0.03	0.90	0.211	0.003	2912	56	2912	132	2912	26	100
519696	Zircon_sample-117	284	0.34	16.81	0.62	0.58	0.03	0.92	0.211	0.004	2924	47	2941	107	2912	31	101
519696	Zircon_sample-118	309	0.93	13.59	1.05	0.46	0.04	0.89	0.218	0.002	2722	73	2425	155	2925	18	82
519696	Zircon_sample-124	169	0.36	15.74	0.42	0.54	0.01	0.94	0.210	0.002	2801	26	2794	57	2909	15	96
519696	Zircon_sample-125	93	0.52	15.54	0.49	0.53	0.01	0.76	0.212	0.004	2849	30	2748	54	2921	33	94
519696	Zircon_sample-127	170	0.52	17.01	0.57	0.58	0.01	0.74	0.213	0.005	2936	32	2943	58	2930	36	100
519696	Zircon_sample-129	245	0.37	16.16	0.61	0.56	0.02	0.87	0.211	0.004	2886	36	2850	75	2912	30	98
519696	Zircon_sample-130	192	0.55	16.93	0.68	0.57	0.02	0.82	0.214	0.005	2931	39	2920	78	2938	37	99
519696	Zircon_sample-131	987	0.46	13.36	0.52	0.48	0.02	0.92	0.204	0.003	2705	38	2519	74	2855	24	88
519696	Zircon_sample-132	198	0.30	14.89	0.81	0.51	0.03	0.90	0.210	0.005	2808	52	2872	107	2907	39	92
519696	Zircon_sample-138	439	0.40	11.67	1.01	0.42	0.03	0.96	0.205	0.005	2602	78	2281	165	2863	38	80
519696	Zircon_sample-141	526	0.32	11.54	0.70	0.40	0.03	0.98	0.210	0.003	2506	62	2154	118	2805	23	74
519696	Zircon_sample-143	91	0.35	15.85	0.87	0.54	0.03	0.91	0.212	0.005	2868	52	2795	112	2920	37	96
519696	Zircon_sample-144	344	0.52	17.35	0.62	0.59	0.02	0.97	0.213	0.002	2954	34	2967	83	2932	14	102
519696	Zircon_sample-152	150	0.53	15.67	0.45	0.53	0.01	0.88	0.218	0.003	2869	27	2736	56	2864	22	92
519696	Zircon_sample-153	839	0.60	16.83	0.45	0.57	0.01	0.89	0.214	0.003	2925	25	2911	55	2935	19	99
519696	Zircon_sample-166	121	0.11	10.13	2.05	0.36	0.07	0.89	0.202	0.006	2447	189	3033	349	2840	48	71
519696	Zircon_sample-157	142	0.50	17.04	0.67	0.58	0.02	0.91	0.213	0.004	2937	38	2947	84	2931	27	101
519696	Zircon_sample-158	55	0.41	15.42	0.70	0.54	0.02	0.92	0.208	0.004	2842	44	2789	94	2894	29	96
519901																	
519901	Zircon_sample-007	459	0.30	15.71	0.43	0.56	0.01	0.82	0.205	0.003	2890	26	2850	52	2867	25	96
519901	Zircon_sample-009	181	1.45	15.49	0.41	0.54	0.01	0.88	0.208	0.003	2846	26	2784	52	2860	22	96
519901	Zircon_sample-012	742	0.33	14.38	0.34	0.51	0.01	0.96	0.204	0.001	2775	23	2884	50	2857	11	93
519901	Zircon_sample-015	455	1.21	14.13	0.78	0.50	0.02	0.88	0.203	0.005	2758	52	2834	105	2851	42	92
519901	Zircon_sample-022	799	1.38	15.10	0.37	0.53	0.01	0.87	0.208	0.002	2821	23	2728	48	2860	19	94
519901	Zircon_sample-023	247	0.48	15.57	0.34	0.54	0.01	0.96	0.209	0.001	2851	21	2782	48	2900	9	96
519901	Zircon_sample-024	169	1.34	15.56	0.11	0.54	0.00	0.81	0.211	0.001	2850	7	2764	13	2912	7	95
519901	Zircon_sample-025	387	0.38	16.33	0.45	0.57	0.01	0.81	0.209	0.002	2867	26	2868	59	2901	18	100
519901	Zircon_sample-027	171	0.44	16.21	1.51	0.62	0.05	0.94	0.215	0.006	3001	60	3062	192	2941	46	105
519901	Zircon_sample-028	408	0.20	12.71	0.52	0.44	0.02	0.95	0.210	0.003	2658	38	2346	76	2905	20	81

Appendix 2: Sample processing and geochemical analysis at the Central Analytical Facility (CAF, University of Stellenbosch)

A: Sample processing (crushing and milling)

A steel jaw crusher and a steel mill pot was used for the crushing and milling, respectively, of the rocks. Table 2(a) reports tests that were performed in the laboratory to assess contamination induced by grinding/powdering during sample milling. The tests were performed on clean quartz in the various mill pots to test for maximum contamination. Quartz chips were too small for the steel jaw crusher, but the maximum contamination due to steel was simulated by using the steel mill pot. These tests show that the steel mill may introduce significant amounts of Fe₂O₃ and Cr, as well as smaller amounts of Ni, Pb and Zr. The results in Table 2(a) represent a "worst case scenario" due to the hardness of the tested material, and generally it is believed that the contamination is minor. No correlation has been attempted implemented to the analysed samples.

Sample	Al ₂ O ₃	CaO	Cr ₂ O ₃	Fe ₂ O ₃	K ₂ O	MgO	MnO	Na ₂ O	P ₂ O ₅	SiO ₂	TiO ₂	Sum
Quartz Standard bought	0.168	0.035	0.003	0.015	0.027	0.065	0.003	0.151	0.015	99.823	0.004	100.31
Quartz (Steel mill pot)	0.041	0.013	0.056	0.392	0.003	0.035	0.002	0.012	0.005	99.966	0.000	100.53

Table 2a: Contaminations in wt% determined on CAF's XRF instrument (see below). The composition of the quartz used in this milling experiment is not known, because the ICP unit uses the same preparation instruments. The bought standard SARM 49 (South African Reference Material) was already milled by the manufacturer. Fusions were prepared with a Claisse Fluxer, platinum ware crucibles and with Li-Meta/Tetraboride flux, which possibly also contain some traces.

Similar tests were performed for LA-ICPMS analyses on fused glass discs (Table 2b). Maximum contamination was determined on milled clean quartz, whereas minimum values where indicated were calculated from more than 400 samples processed in the same way but with hardness less than quartz. From these results we see that the Steel mill pot does contaminate mainly with Co and to a much lesser extent with Ni, Cu and Sc.

Element (ppm)	V	Cr	Co	Ni	Cu	Zn	Ga	Rb	Sr	Y
Quartz Standard bought	4	9	0	6	2	5	1	2	8	3
Quartz (Steel mill pot)	0	217	1	33	2	3	1	2	5	1
Element (ppm)	Zr	Nb	Ba	La	Ce	Nd	Pb	Th	U	
Quartz Standard bought	89	3	16	2	2	2	11	1	1	
Quartz (Steel mill pot)	13	2	5	2	9	5	11	2	3	

Table 2b: Contaminations in ppm determined on CAF's XRF instrument (see below). Results reflect any impurities present in the quartz as well. Red numbers emphasize the greatest contaminants.

B: Major oxide analysis on XRF instrument

Major element compositions (in wt%) were obtained at the Central Analytical Facility (University of Stellenbosch) by X-Ray Fluorescence (XRF) analysis, using a Phillip's PW1404w instrument (Axios from PANalytical with a 2.4 kWatt Rh X-ray Tube). The gas-flow proportional counting detector and scintillation detector, or a combination of the two, was used to cover the elements from fluorine to uranium. Major elements (Na₂O, MgO, SiO₂, K₂O, CaO, TiO₂, MnO, P₂O₅, Al₂O₃, Cr₂O₃ and Fe₂O₃T (total iron) were analysed on La-free fused glass beads. A wide range of international (NIST®) and national (SARM®) standards is used in the calibration procedures and quality control (precision and accuracy). Detection limits for the elements quoted, depending on the matrix (combination of elements present), are approximately 0.001 wt% for major elements on these fused beads (cf., Table 2c).

Fusion bead method for major element analysis:

- Weigh 1.0000g ± 0.0009g of milled sample
- Place in oven at 110 °C for 1 hour to determine H₂O⁻
- Place in oven at 1000 °C for 1 hour to determine LOI (loss on ignition)
- Add 10.0000g ± 0.0009g Claisse flux and fuse in M4 Claisse fluxer for 23 minutes.

Loss on Ignition (LOI) comprises contributions from the volatile compounds H₂O⁺, OH⁻, CO₂, F, Cl, S, and added O₂ due to oxidation (mainly of FeO to Fe₂O₃).

One or more of the following standard reference materials were used: NIM-N, NIM-G, NIM-S, NIM-P, NIM-D, AGV-1, BHVO-1, GA, GH, GSN, SY-2, SY-3, and BCR

Analyte	Al ₂ O ₃	CaO	Fe ₂ O ₃	MgO	MnO	P ₂ O ₅	K ₂ O	SiO ₂	Na ₂ O	TiO ₂	LOI
Uncertainty	0.11688	0.07288	0.14672	0.02416	0.00904	0.00364	0.0172	0.3506	0.10448	0.02096	0.03
LOD	0.06	0.04	0.01	0.04	0.01	0.01	0.01	0.03	0.01	0.02	0.01

Table 2c: Detection limits and uncertainties for major oxides (all in wt%).

C: Trace element analysis on LA-ICPMS instrument

Trace element compositions (in ppm) were obtained from the same fused beads as the major elements by applying the method described by Eggins (2003) and analysed using an Agilent 7500ce ICP-MS coupled with a Nd-YAG 223 nm New Wave LASER ablation (LA) system operating at a 12 Hz frequency with a mixed He-Ar carrier gas. Three spot analyses (each comprising a 30 s blank followed by data collection for 60 s) on each whole rock fused disc were obtained using a 100 µm diameter aperture, and the results averaged.

After every three samples (i.e., every 10th analysis) a National Institute on Standards and Technology NIST612 (Pearce et al. 1997) glass bead (in this case BCR, Table 1d) was analysed as calibration standard, in addition to fused discs of Nim-G (granite) and BhVO-1 (basalt) as secondary standards. Data were collected in the time-resolved mode and, were reduced using an Excel calculation spreadsheet using the SiO₂ content measured by XRF as the internal standard. For each element the reproducibility of replicate analyses of the samples, and deviation from the certified values of the secondary standards are better than 10%, and mostly below 5% relative (cf., Table 2d).

Element	Sc	V	Cr	Co	Ni	Cu	Zn	Rb	Sr	Y	Zr	Nb
LA QC std	33	425.00	17	38	13	21	125	47	342	35	184	12.5
Average Analysed	38.08	435.54	15.47	38.09	11.98	17.02	159.18	46.90	359.52	37.15	199.72	13.20
% Deviation	15.39	2.48	9.02	0.25	7.88	18.95	27.34	0.21	5.12	6.15	8.54	5.64
Fusion control std	33	416.00	18	37	18	21	127	46.9	340	37	184	12.6
Average Analysed	39.12	446.72	19.47	37.50	15.35	19.86	118.23	46.32	372.13	37.74	203.09	13.39
% Deviation	18.54	7.38	8.17	1.35	14.75	5.41	6.91	1.23	9.45	2.00	10.38	6.26
Element	Mo	Sn	Cs	Ba	La	Ce	Pr	Nd	Sm	Eu	Gd	Tb
LA QC std	270	2.6	1.16	683	24.7	53.3	6.7	28.9	6.59	1.97	6.71	1.02
Average Analysed	265.30	2.12	1.14	711.42	27.35	54.91	7.02	31.39	7.32	2.09	7.29	1.10
% Deviation	1.74	18.54	1.40	4.16	10.71	3.03	4.80	8.61	11.01	6.12	8.58	7.52
Fusion control std	250		1.1	677	24.9	52.9	6.7	28.7	6.58	1.96	6.75	1.07
Average Analysed	278.45	2.56	1.12	732.75	27.95	55.81	7.16	32.05	7.54	2.13	7.47	1.11
% Deviation	11.38		1.45	8.23	12.26	5.50	6.93	11.67	14.58	8.57	10.68	3.98
Element	Dy	Ho	Er	Tm	Yb	Lu	Hf	Ta	W	Pb	Th	U
LA QC std	6.44	1.27	3.7	0.51	3.39	0.503	4.84	0.78	0.50	11	5.90	1.69
Average Analysed	7.14	1.44	4.03	0.59	3.81	0.57	5.30	0.89	0.56	10.98	7.12	1.73
% Deviation	10.87	13.09	8.92	15.28	12.47	12.92	9.49	13.68	12.28	0.19	20.59	2.22
Fusion control std	6.41	1.28	3.66	0.54	3.38	0.503	4.9	0.74		11	5.7	1.69
Average Analysed	7.27	1.47	4.15	0.60	3.84	0.57	5.35	0.85	0.67	10.08	6.85	1.77
% Deviation	13.45	14.53	13.41	11.31	13.73	13.62	9.14	15.15		8.34	20.20	4.67

Table 2d: Accuracy of trace element analysis of BCR standard glass (LA-QC-std) and powder (Fusion-Control-std).

Appendix 3: Geochemical data for the Nigerlikasik supracrustal rock sequence

GEUS ID	519901	519689	519698	519697	519696	519695	519694	519693	519692	519691	519689	519690	519688	519687	519686	519684	519683	519682
Rock type	TTG	TTG	Schist	Amph.	Aplite	Amph.	Schist	Serp.	Serp.	Serp.	Serp.	Amph.	Serp.	Serp.	Amph.	Serp.	Serp.	Serp.
Strat. (m)	-4.0	-1.0	0.4	9.5	11.5	14.3	19.3	22.1	24.9	27.1	32.2	32.3	36.8	37.4	40.4	43.8	46.3	48.1
SiO ₂	69.13	74.28	54.89	48.39	72.18	52.12	54.49	45.97	48.07	46.75	50.02	50.02	48.49	47.40	48.62	49.14	49.35	50.28
TiO ₂	0.26	0.08	1.19	1.23	0.28	0.96	1.38	0.63	0.70	0.71	0.72	1.07	0.86	0.74	0.80	0.70	0.41	0.19
Al ₂ O ₃	14.33	14.25	15.77	13.70	14.60	12.03	13.20	3.32	4.38	4.46	3.98	7.23	5.23	4.69	5.15	4.67	13.13	5.49
Fe ₂ O ₃	2.19	1.02	6.89	16.07	2.85	11.63	14.28	12.36	15.51	15.17	13.66	18.18	16.36	16.03	16.42	18.51	12.80	11.83
CaO	1.99	0.86	9.85	9.53	1.94	9.63	7.54	15.60	8.92	13.39	12.61	9.28	12.02	13.19	12.03	7.89	6.51	5.13
MgO	0.54	0.08	4.77	6.64	0.84	9.09	4.28	15.54	17.96	14.51	13.02	10.36	14.08	12.82	12.90	16.97	12.87	23.77
MnO	0.06	0.05	0.11	0.29	0.06	0.24	0.28	0.33	0.32	0.31	0.29	0.29	0.31	0.33	0.30	0.30	0.21	0.18
Na ₂ O	4.04	3.73	4.35	2.04	4.58	2.08	2.33	0.31	0.42	0.46	0.60	1.60	0.60	0.55	0.53	0.42	1.81	0.24
K ₂ O	2.83	4.79	0.61	0.46	0.97	0.58	0.45	0.04	0.52	0.16	0.65	0.50	0.11	0.21	0.28	0.04	1.68	0.02
P ₂ O ₅	0.08	0.01	bd	0.09	0.07	0.09	0.09	0.03	0.03	0.04	0.03	0.07	0.04	0.04	0.04	0.04	0.03	0.01
Cr ₂ O ₃	0.001	0.001	0.020	0.020	0.001	0.112	0.001	0.235	0.245	0.224	0.143	0.031	0.204	0.255	0.275	0.275	0.143	0.326
LOI	0.50	0.29	0.93	0.95	0.96	1.55	1.68	6.23	3.58	4.09	4.07	1.18	2.01	3.94	2.74	1.27	1.12	3.86
H ₂ O-	0.05	0.03	0.03	0.01	0.00	0.08	0.12	0.04	0.02	0.01	-0.02	0.00	0.03	0.01	-0.01	0.04	0.02	0.02
Sum	96.00	99.48	99.42	99.42	99.32	100.19	100.11	100.62	100.66	100.29	99.77	99.82	100.33	100.21	100.07	100.27	100.08	101.35
C	7.14	4.72	46.55	45.04	6.40	44.11	55.03	47.55	34.44	33.55	58.52	37.17	39.22	37.91	47.11	36.00	47.14	21.94
V	25.93	11.02	299.98	312.75	33.45	266.20	444.58	181.80	181.80	186.41	222.52	252.11	213.39	226.69	287.80	204.43	231.16	109.60
Cr	13.25	12.37	193.86	135.65	21.24	744.02	20.19	1718.21	1639.80	1528.03	1022.95	209.28	1288.37	1691.97	2162.33	1921.25	1041.62	2189.19
Co	4.27	1.13	21.48	47.73	4.37	26.67	13.14	66.47	86.77	84.71	77.51	76.12	88.07	92.35	117.83	100.77	72.69	104.89
Ni	12.25	9.25	123.75	85.14	11.52	45.18	10.92	396.81	650.03	643.70	312.04	189.53	433.64	659.85	812.83	752.37	315.70	708.51
Cu	7.42	7.31	9.55	110.49	23.75	38.43	21.06	23.28	36.57	50.23	247.82	329.30	16.40	86.78	205.65	285.63	17.94	10.71
Zn	55.88	23.26	61.28	104.76	47.71	85.88	81.70	96.45	87.70	76.51	89.66	95.46	118.77	108.64	137.14	98.02	79.41	68.73
Rb	116.13	211.05	35.06	13.81	48.38	31.47	10.69	1.25	31.09	5.33	34.98	33.03	1.00	6.06	10.45	0.66	71.25	0.22
Sr	211.18	57.24	195.29	101.45	184.20	160.39	107.06	141.28	68.95	125.10	121.65	96.17	90.36	106.05	94.32	14.98	78.12	4.62
Y	7.96	5.40	26.62	26.54	3.71	20.79	32.72	9.54	10.21	10.73	12.16	16.97	10.85	9.81	11.64	10.21	14.58	6.01
Zr	87.48	49.21	86.33	76.05	81.70	69.96	103.28	33.14	36.55	38.25	38.47	64.42	43.82	40.47	55.47	39.60	30.96	12.35
Nb	6.72	9.62	4.68	3.32	3.90	4.53	3.70	1.57	2.04	2.01	1.82	3.13	2.31	2.02	2.72	2.47	1.30	0.38
Mo	0.83	0.97	3.09	5.59	1.69	10.85	1.16	0.98	0.97	0.74	0.83	0.69	0.71	0.79	0.99	0.91	1.20	0.89
Sn	2.14	1.40	2.29	1.57	1.54	3.09	1.30	1.52	1.42	1.27	1.47	1.61	1.39	1.72	1.91	2.35	1.94	1.16
Cs	4.96	4.48	0.48	0.48	1.59	0.61	1.73	1.36	59.01	9.46	43.03	35.96	0.86	3.98	6.54	0.88	53.05	0.24
Ba	598.62	272.13	133.09	63.42	390.06	115.25	59.59	12.03	115.55	77.64	193.36	245.15	24.50	70.31	109.92	8.07	462.09	4.41
La	18.64	4.69	3.34	4.00	9.21	2.48	3.93	2.15	2.62	2.62	2.78	4.69	2.55	2.72	4.78	3.83	3.00	0.86
Ce	42.46	12.20	8.02	10.55	19.07	5.88	9.49	6.00	7.58	7.53	7.99	12.08	7.68	7.74	12.63	9.63	7.67	2.10
Pr	4.06	1.37	1.37	1.66	1.90	0.92	1.32	0.97	1.15	1.21	1.33	1.97	1.24	1.23	1.91	1.48	1.00	0.27
Nd	15.01	5.03	8.04	8.99	7.03	5.19	6.99	5.68	6.16	6.42	7.48	10.73	6.90	6.51	9.90	7.31	4.40	1.34
Sm	2.40	1.02	2.88	2.99	1.01	2.19	2.75	1.77	2.14	2.52	3.22	2.04	2.06	2.93	2.09	1.32	0.48	
Eu	0.51	0.20	0.62	0.99	0.38	0.78	0.90	0.63	0.52	0.69	0.79	1.00	0.76	0.72	0.92	0.61	0.77	0.24
Gd	1.64	0.92	3.33	3.80	0.82	3.00	3.99	2.09	2.05	2.18	2.55	3.51	2.08	2.05	2.81	2.28	1.86	0.76
Tb	0.19	0.12	0.62	0.66	0.10	0.53	0.73	0.29	0.33	0.34	0.45	0.58	0.35	0.34	0.45	0.34	0.33	0.16
Dy	1.32	0.82	4.47	4.81	0.64	3.75	5.76	1.98	2.05	2.19	2.81	3.67	2.43	2.24	2.65	2.22	2.60	1.08
Ho	0.24	0.20	0.94	1.02	0.12	0.80	1.22	0.41	0.42	0.41	0.51	0.68	0.47	0.41	0.51	0.43	0.57	0.26
Er	0.63	0.62	2.83	3.04	0.45	2.35	3.67	1.14	1.12	1.16	1.44	1.89	1.27	1.12	1.34	1.14	1.68	0.74
Tm	0.11	0.08	0.43	0.45	0.05	0.34	0.58	0.15	0.16	0.15	0.16	0.27	0.17	0.15	0.18	0.16	0.25	0.12
Yb	0.76	0.66	2.95	2.89	0.42	2.16	3.93	0.88	0.98	0.95	1.19	1.57	1.03	0.97	1.10	0.91	1.76	0.84
Lu	0.13	0.11	0.47	0.42	0.06	0.34	0.59	0.14	0.13	0.14	0.16	0.23	0.15	0.14	0.16	0.13	0.30	0.12
Hf	2.33	1.96	2.38	2.19	2.14	1.98	2.85	0.93	1.01	1.00	1.32	1.80	1.25	1.17	1.54	1.16	0.88	0.35
Ta	0.47	0.88	0.45	0.23	0.31	0.27	0.22	0.10	0.14	0.12	0.12	0.20	0.14	0.13	0.16	0.13	0.07	0.03
W	0.52	0.49	0.88	0.96	0.76	0.91	0.97	0.84	0.69	0.59	0.99	0.63	0.53	0.45	0.56	0.47	0.57	0.56
Pb	22.78	32.39	66.36	5.02	20.70	5.78	9.81	2.73	1.08	1.96	2.63	2.09	1.34	1.55	3.08	0.80	1.47	0.63
Th	4.50	5.71	2.41	0.42	2.70	0.54	0.76	0.45	0.28	0.32	0.24	0.47	0.52	0.30	0.54	0.33	0.19	0.11
U	1.03	2.38	0.75	0.23	1.14	0.55	0.20	0.07	0.12	0.08	0.07	0.12	0.10	0.09	0.11	0.13	0.11	0.04

Appendix Table 3 (continued)

GEUS ID	519681	519680	519679	519678	519676	519677	519675	519674	519673	519672	519671	519670	519669	519667	519668	519666	519665	519664	519663
Rock type	Amph.	Schist	Amph.	Amph.	Amph.	Aplite	Amph.	Amph.	Amph.	Schist	Amph.	Amph.	Amph.	Amph.	Schist	Amph.	Amph.	Amph.	Amph.
Strat. (m)	51.7	54.2	57.7	66.0	70.7	71.2	74.0	83.1	88.5	95.7	98.5	102.7	109.1	110.5	110.9	112.3	119.2	130.2	144.6
SiO ₂	48.65	63.68	52.23	49.81	51.05	71.82	49.35	51.16	52.54	69.57	50.99	49.83	53.84	52.17	68.47	52.96	53.98	51.37	47.52
TiO ₂	0.40	0.49	1.64	0.95	1.37	0.28	1.08	0.92	0.97	0.31	0.64	0.60	1.71	1.83	0.42	1.81	1.80	1.75	1.26
Al ₂ O ₃	14.78	16.21	13.90	14.55	15.19	15.68	13.88	14.31	14.59	15.24	14.81	14.97	11.62	12.94	15.69	12.62	12.36	13.62	14.88
Fe ₂ O ₃	9.17	5.95	14.97	10.91	13.79	2.44	11.54	11.68	10.79	2.96	11.39	11.40	17.05	16.89	3.79	16.18	16.13	16.81	16.68
CaO	13.85	6.27	7.94	9.92	8.50	2.00	11.72	11.26	9.99	3.55	11.25	11.91	6.91	7.14	2.82	7.49	6.28	6.14	7.49
MgO	10.03	2.29	4.58	7.11	5.47	0.74	5.42	6.20	5.11	1.18	7.21	6.86	5.14	4.18	1.44	3.93	3.90	4.77	7.60
MnO	0.23	0.14	0.26	0.20	0.27	0.04	0.24	0.24	0.23	0.05	0.24	0.26	0.31	0.07	0.28	0.31	0.28	0.28	0.29
Na ₂ O	0.81	3.69	2.87	2.76	2.78	4.70	2.04	1.83	2.49	2.66	0.92	1.65	1.93	2.79	4.26	2.74	2.74	3.22	2.81
K ₂ O	0.12	0.11	0.14	0.30	0.11	1.02	0.18	0.06	0.05	2.29	0.39	0.11	0.38	0.22	1.41	0.21	0.23	0.15	0.22
P ₂ O ₅	0.01	0.10	0.12	0.05	0.08	0.08	0.08	0.07	0.07	0.08	0.04	0.03	0.31	0.28	0.12	0.27	0.29	0.20	0.14
Cr ₂ O ₃	0.051	0.001	0.001	0.020	0.010	0.001	0.020	0.020	0.020	0.001	0.041	0.041	0.010	0.001	0.001	0.001	0.001	0.001	0.010
LOI	1.72	0.98	0.97	1.62	0.70	0.98	4.30	2.30	2.55	1.81	1.89	2.42	0.45	0.89	1.18	1.29	1.48	1.70	1.46
H ₂ O-	0.03	0.02	0.04	0.02	0.03	0.01	0.03	0.03	0.04	-0.02	0.07	0.07	0.09	0.11	0.02	0.13	0.14	0.16	-0.01
Sum	99.86	99.94	99.67	98.23	99.34	99.79	99.89	100.08	99.44	99.68	99.89	100.16	99.73	99.69	99.70	99.89	99.63	100.18	100.35
Sc	78.48	17.08	47.04	42.83	49.42	6.37	43.42	46.99	46.13	5.81	59.55	65.45	57.12	40.98	9.35	41.76	44.06	46.04	33.31
V	304.44	111.17	452.49	257.96	376.55	27.78	286.99	279.03	270.86	39.85	293.67	327.92	226.28	276.07	58.45	268.93	275.22	286.08	244.33
Cr	432.54	56.34	22.45	144.11	103.71	17.86	141.33	148.17	140.17	33.91	284.12	399.60	142.21	27.20	31.26	29.00	86.59	48.33	116.14
Co	55.73	18.54	50.20	40.51	48.60	5.03	38.06	40.42	40.29	6.83	41.78	52.64	42.59	41.28	10.12	39.98	42.12	41.58	64.23
Ni	86.81	26.03	48.00	116.54	70.22	11.73	68.31	75.61	74.45	19.30	87.58	138.38	67.88	49.25	22.17	51.76	87.77	59.19	190.24
Cu	34.60	24.86	97.70	68.13	147.57	27.82	132.77	100.12	97.81	22.47	125.75	54.90	93.61	101.98	13.49	108.69	71.96	93.56	57.17
Zn	54.90	45.05	85.26	49.42	104.43	32.49	72.55	76.39	75.67	45.11	59.37	81.04	115.01	143.64	39.91	110.63	104.09	111.47	110.06
Rb	6.96	2.83	2.03	9.89	1.56	23.74	4.10	1.13	1.09	61.48	10.18	1.66	7.36	2.96	32.66	2.72	7.40	2.42	3.93
Sr	150.84	288.09	196.74	187.78	197.11	99.97	197.25	153.10	145.70	53.91	105.64	78.19	131.66	82.46	84.30	88.62	142.74	83.65	126.74
Y	15.51	10.19	34.53	16.10	28.31	3.34	22.13	18.14	18.25	3.14	16.63	18.28	53.88	54.11	6.40	53.19	34.72	43.56	30.00
Zr	32.30	95.48	131.25	57.67	104.71	113.33	79.73	60.49	62.35	76.51	38.28	43.40	147.08	162.61	121.81	158.76	112.71	131.48	90.99
Nb	1.27	2.52	6.72	2.95	5.57	3.65	3.97	3.01	2.91	2.73	1.57	1.66	6.13	6.60	3.47	6.56	4.96	5.05	3.88
Mo	1.26	1.68	1.08	0.83	1.22	1.07	1.03	0.99	0.78	1.07	1.02	1.13	1.14	1.40	1.02	1.23	1.19	1.16	1.01
Sn	1.81	1.92	1.58	1.35	2.08	1.40	1.63	1.29	1.42	1.01	1.29	1.39	1.81	1.88	1.77	1.99	1.71	1.69	1.39
Cs	2.12	0.27	0.56	0.63	0.34	1.56	0.64	0.35	0.25	3.68	1.48	0.49	6.72	0.69	4.71	0.45	0.58	0.37	0.70
Ba	48.58	47.92	41.53	51.20	18.56	472.44	45.38	18.99	16.80	628.76	108.70	46.79	40.03	82.83	434.91	75.44	78.46	30.47	60.01
La	1.50	13.24	7.86	4.25	7.73	15.92	5.88	4.52	4.57	9.52	2.26	2.62	11.76	12.10	17.57	12.58	8.91	10.00	6.85
Ce	3.74	27.51	22.02	10.85	19.59	28.26	13.91	11.00	11.36	20.71	5.65	6.28	28.06	29.01	33.32	29.95	20.87	23.10	16.86
Pr	0.58	3.26	3.40	1.58	2.80	2.99	2.05	1.65	1.69	1.96	0.83	0.91	4.08	4.25	3.73	4.31	3.08	3.38	2.45
Nd	3.49	13.31	17.95	8.02	14.81	10.38	11.39	8.45	8.83	7.15	4.48	4.84	21.70	21.76	13.83	22.35	15.38	17.27	12.76
Sm	1.40	2.62	5.34	2.61	4.47	1.51	3.49	2.57	2.74	1.25	1.48	1.79	6.52	6.68	2.36	6.54	4.53	5.30	3.68
Eu	0.41	0.77	1.67	0.81	1.35	0.42	1.16	0.83	0.89	0.37	0.55	0.57	1.97	2.01	0.66	1.93	1.28	1.59	1.18
Gd	1.93	2.30	6.31	2.84	5.20	1.04	3.91	3.10	3.15	0.82	2.16	2.43	8.15	8.12	1.72	7.92	5.36	6.69	4.52
Tb	0.38	0.26	1.01	0.46	0.82	0.15	0.68	0.53	0.50	0.11	0.38	0.43	1.39	1.36	0.21	1.32	0.89	1.11	0.79
Dy	2.87	1.83	6.78	3.24	5.55	0.72	4.24	3.59	3.39	0.54	2.75	3.33	9.96	9.62	1.23	9.56	6.33	7.73	5.72
Ho	0.57	0.38	1.36	0.61	1.10	0.11	0.88	0.70	0.70	0.11	0.63	0.71	2.14	2.10	0.22	2.05	1.27	1.71	1.17
Er	1.82	1.10	3.83	1.73	3.14	0.29	2.47	2.04	1.99	0.32	1.83	2.07	6.28	6.27	0.59	6.08	3.81	5.00	3.57
Tm	0.27	0.18	0.56	0.26	0.44	0.04	0.34	0.31	0.30	0.05	0.27	0.33	0.91	0.92	0.11	0.90	0.56	0.74	0.51
Yb	1.86	1.21	3.58	1.75	2.86	0.28	2.33	1.97	1.91	0.31	1.92	2.21	6.27	6.21	0.67	5.92	3.88	4.92	3.54
Lu	0.27	0.19	0.54	0.24	0.42	0.04	0.36	0.29	0.28	0.04	0.31	0.35	0.94	0.91	0.09	0.88	0.54	0.73	0.54
Hf	1.04	2.64	3.52	1.65	2.87	2.74	2.18	1.74	1.73	1.89	1.10	1.25	4.25	4.57	3.11	4.47	3.09	3.83	2.69
Ta	0.07	0.15	0.44	0.16	0.35	0.29	0.26	0.20	0.20	0.19	0.09	0.11	0.41	0.44	0.22	0.43	0.30	0.33	0.28
W	0.80	0.57	1.25	0.71	0.69	1.07	0.87	0.55	0.52	1.26	0.57	0.83	0.63	0.68	0.52	1.05	1.09	1.31	0.98
Pb	2.38	4.36	3.53	1.33	3.05	4.01	1.96	1.24	1.80	2.77	2.02	1.26	2.39	3.36	2.61	3.63	7.76	1.94	2.80
Th	0.20	2.02	1.19	0.50	0.86	2.94	0.68	0.53	0.56	2.48	0.39	0.33	1.35	1.48	2.48	1.43	2.10	1.18	0.89
U	0.04	0.48	0.32	0.11	0.25	0.67	0.17	0.13	0.12	0.51	0.06	0.08	0.36	0.35	0.53	0.35	0.23	0.26	0.23

Appendix Table 3 (continued)

GEUS ID	519662	519661	519660	519659	519658	519657	519656	519655	519654	519653	519652	519651	519650	519649	519648	519647	519646	519645	519644
Rock type	Amph.	Amph.	Schist	Amph.	Quartz.	Aplite	Quartz.	Amph.	Amph.	Amph.	Amph.	Amph.	Amph.						
Strat. (m)	150.7	159.5	163.1	171.7	186.6	188.5	196.8	202.6	207.5	213.1	215.2	216.1	216.6	217.4	219.7	222.4	229.6	231.6	233.9
SiO ₂	51.42	50.49	59.33	52.17	52.68	56.05	53.34	47.92	49.50	49.89	52.11	71.69	61.29	52.85	44.93	47.46	50.53	50.02	47.04
TiO ₂	1.68	1.25	0.60	1.29	1.37	1.33	1.41	0.95	0.79	1.95	1.45	0.27	0.63	1.49	1.34	1.26	1.21	1.25	1.24
Al ₂ O ₃	13.60	14.89	16.72	14.20	14.26	14.67	15.16	15.53	15.89	12.46	13.17	15.41	17.70	13.72	16.69	16.26	14.01	13.97	14.13
Fe ₂ O ₃	16.52	14.94	7.72	13.24	13.76	11.47	13.17	13.82	11.31	21.09	17.08	2.36	5.47	16.29	15.90	15.01	14.79	14.43	15.64
CaO	7.48	7.55	5.81	8.52	7.26	7.08	7.84	9.18	8.70	7.66	7.99	1.94	5.21	7.29	8.72	9.55	9.60	9.96	11.21
MgO	5.35	6.95	3.56	5.48	6.15	4.93	5.12	8.12	8.28	4.36	4.51	0.80	3.17	4.58	8.13	7.01	5.59	6.11	5.85
MnO	0.27	0.27	0.16	0.26	0.23	0.21	0.27	0.28	0.26	0.41	0.29	0.04	0.13	0.26	0.32	0.32	0.30	0.32	0.32
Na ₂ O	2.62	2.86	3.99	1.38	1.13	2.93	2.63	2.66	2.94	1.60	2.23	3.97	5.48	2.60	2.57	2.39	2.33	2.31	0.63
K ₂ O	0.28	0.16	0.73	1.30	1.36	0.30	0.24	0.35	0.41	0.33	0.29	2.04	0.08	0.17	0.14	0.11	0.10	0.09	1.19
P ₂ O ₅	0.19	0.13	0.13	0.13	0.15	0.15	0.15	0.06	0.04	0.12	0.12	0.08	0.13	0.13	0.09	0.10	0.09	0.08	0.09
Cr ₂ O ₃	0.010	0.020	0.010	0.020	0.010	0.020	0.020	0.031	0.092	0.001	0.001	0.001	0.020	0.001	0.031	0.020	0.020	0.031	0.031
LOI	0.94	1.01	1.14	1.95	1.61	0.74	0.87	1.03	1.64	0.36	0.30	1.07	0.42	1.02	1.25	0.68	1.59	1.51	2.81
H ₂ O-	0.12	0.00	0.03	-0.01	0.02	0.01	0.01	0.00	0.04	0.01	0.04	0.08	0.04	0.03	0.06	0.00	0.01	0.03	0.00
Sum	100.47	100.53	99.94	99.91	100.00	99.88	100.24	99.92	99.88	100.23	99.56	99.74	99.78	100.44	100.16	100.16	100.17	100.10	100.17
Sc	44.02	38.66	20.40	46.23	44.84	46.42	45.08	43.61	50.42	55.92	49.88	5.50	17.27	55.70	46.68	45.26	51.97	49.58	52.80
V	299.20	261.63	140.60	296.34	262.79	262.97	310.80	262.14	253.77	472.61	372.94	28.81	110.92	407.87	338.34	298.54	343.35	344.47	340.26
Cr	67.28	165.33	97.65	146.26	124.89	133.71	129.12	233.23	591.65	10.07	13.76	21.02	155.25	17.32	225.56	172.11	198.01	191.58	210.64
Co	45.97	49.54	23.86	41.51	43.70	40.67	42.02	53.88	39.52	56.62	46.52	5.28	30.96	49.74	56.71	54.00	48.12	40.19	52.31
Ni	73.08	124.95	47.89	65.02	67.11	71.20	66.52	143.48	92.90	25.25	39.58	14.44	116.02	43.13	160.01	129.96	71.99	65.86	79.91
Cu	118.98	92.36	26.69	80.92	82.67	87.84	49.45	96.20	86.69	124.26	125.53	4.89	26.67	97.14	44.08	57.55	31.23	48.59	47.05
Zn	87.71	94.12	59.18	93.17	106.66	93.64	103.02	96.66	62.32	157.53	108.73	52.17	199.68	111.51	89.05	119.98	97.74	77.19	99.11
Rb	3.40	3.01	20.25	32.03	34.90	7.25	6.62	7.16	13.49	4.06	2.61	64.78	1.97	1.81	1.82	0.77	1.59	1.38	28.97
Sr	117.61	141.22	264.92	74.89	74.15	114.31	145.59	163.69	138.12	77.86	136.53	68.18	125.21	148.42	165.16	165.80	209.05	74.87	37.04
Y	41.02	31.42	12.28	35.53	37.13	37.07	36.46	20.73	15.87	41.06	32.55	2.65	12.61	38.13	32.41	32.23	27.31	24.35	30.97
Zr	121.29	101.32	94.50	105.69	118.97	117.41	115.87	51.53	37.30	107.46	99.61	95.02	103.83	121.61	82.65	83.01	73.82	64.04	77.19
Nb	5.15	4.06	2.89	4.44	4.77	4.73	4.79	1.98	1.40	4.35	3.81	3.07	4.14	4.55	2.87	2.85	2.67	2.28	2.77
Mo	1.10	1.24	0.94	0.78	1.06	0.90	0.96	1.20	0.70	1.03	0.68	0.77	0.98	1.01	0.85	0.94	0.86	0.76	0.97
Sn	2.01	1.41	1.67	1.63	1.85	2.06	2.26	1.32	1.61	1.99	1.92	1.38	1.50	1.94	1.35	1.62	1.28	1.21	1.97
Cs	0.38	0.26	1.15	4.55	2.07	0.48	0.26	1.10	0.40	0.97	0.20	6.24	0.34	0.60	0.41	0.16	0.21	0.17	5.11
Ba	82.95	59.44	488.72	356.67	619.88	90.44	67.06	114.36	140.41	63.82	179.53	598.73	38.55	50.01	40.13	26.52	23.17	21.39	409.95
La	9.71	7.66	16.42	8.75	10.41	12.28	9.42	2.72	1.99	5.09	7.38	12.86	11.06	8.18	3.98	3.17	3.62	3.10	3.99
Ce	21.98	20.03	30.31	21.32	24.66	24.41	22.54	7.12	5.02	13.59	17.10	23.31	26.32	19.48	10.04	9.79	9.76	8.08	10.20
Pr	3.15	2.61	4.16	2.94	3.44	3.81	3.16	1.14	0.81	2.13	2.49	2.42	3.14	2.88	1.60	1.49	1.51	1.26	1.51
Nd	16.50	13.43	17.41	14.77	17.23	18.89	15.79	6.13	4.24	11.80	12.22	8.24	13.22	14.60	8.89	8.19	7.86	6.75	8.70
Sm	5.09	4.03	2.88	4.18	4.73	5.26	4.71	2.19	1.46	4.44	3.58	1.28	2.82	4.66	3.05	3.35	2.78	2.44	3.16
Eu	1.59	1.34	0.83	1.30	1.58	1.56	1.51	0.77	0.56	1.40	1.16	0.38	0.89	1.44	1.04	1.10	0.94	0.78	1.76
Gd	6.23	4.88	2.55	5.06	6.01	5.82	5.73	2.95	2.09	5.84	4.62	0.85	2.70	5.47	4.22	4.30	3.75	3.04	4.16
Tb	0.99	0.79	0.37	0.87	1.01	0.95	0.91	0.49	0.39	1.04	0.77	0.10	0.38	0.96	0.73	0.73	0.68	0.55	0.70
Dy	7.45	5.89	2.26	6.48	6.72	6.62	6.35	3.78	2.74	7.42	5.65	0.59	2.41	6.74	5.62	5.75	4.85	4.00	5.66
Ho	1.59	1.26	0.46	1.32	1.48	1.41	1.44	0.80	0.60	1.59	1.19	0.10	0.50	1.45	1.24	1.22	1.04	0.86	1.20
Er	4.73	3.61	1.40	4.11	4.43	4.01	4.15	2.34	1.86	4.60	3.59	0.28	1.34	4.36	3.62	3.75	3.20	2.66	3.51
Tm	0.69	0.55	0.17	0.63	0.63	0.63	0.61	0.35	0.25	0.71	0.53	0.04	0.24	0.67	0.56	0.56	0.46	0.38	0.54
Yb	4.57	3.68	1.39	4.08	4.26	4.05	4.07	2.27	1.60	4.72	3.55	0.27	1.45	4.29	3.54	3.69	3.17	2.61	3.64
Lu	0.70	0.56	0.22	0.63	0.63	0.57	0.58	0.34	0.25	0.70	0.52	0.04	0.24	0.66	0.52	0.56	0.47	0.38	0.52
Hf	3.33	2.77	2.30	2.94	3.46	3.12	3.26	1.55	1.03	3.13	2.61	2.23	2.78	3.36	2.28	2.36	2.04	1.69	2.25
Ta	0.34	0.27	0.18	0.29	0.34	0.32	0.30	0.13	0.06	0.27	0.24	0.23	0.29	0.30	0.19	0.20	0.18	0.15	0.16
W	0.53	0.56	0.49	0.61	0.79	0.77	0.46	0.50	0.47	0.76	0.50	0.53	0.57	0.68	0.58	0.51	0.46	0.38	0.67
Pb	1.95	3.01	3.62	2.57	3.30	2.84	3.54	2.70	0.87	1.90	2.68	3.59	3.83	2.99	1.76	2.88	1.11	1.07	1.21
Th	1.19	1.09	1.99	1.15	1.82	1.34	1.59	0.28	0.20	0.63	0.85	2.09	1.89	1.12	0.51	0.46	1.17	0.32	0.52
U	0.25	0.27	0.36	0.29	0.30	0.26	0.33	0.07	0.05	0.14	0.19	0.55	0.55	0.25	0.11	0.11	0.09	0.09	0.10

Appendix Table 3 (continued)

GEUS ID	519643	519642	519641	519640	519639	519638	519637	519636	519635	519634	519633	519632	519631	519630	519629	519626	519627	519628	519625
Rock type	Amph.	Amph.	Schist	Schist	Amph.	Amph.	Schist	Schist	Schist	Schist	Quartz.	Schist	Schist	Schist	Aplite	Schist	Schist	Schist	Schist
Strat. (m)	237.6	240.9	243.2	247.8	251.3	255.9	257.4	258.6	267.8		278.1	284.1	286.0	295.9	303.6	312.8	315.4	315.4	315.4
SiO ₂	47.28	49.98	59.94	59.22	50.49	50.19	48.41	59.57	62.12	57.82	61.93	54.55	56.38	55.84	71.99	57.48	55.41	57.78	57.03
TiO ₂	1.12	1.11	0.63	0.46	1.16	1.73	1.13	0.82	0.50	0.63	0.54	0.70	0.63	0.69	0.33	0.63	0.64	0.62	0.63
Al ₂ O ₃	13.42	14.10	17.49	17.72	14.02	13.21	15.75	16.57	17.10	15.32	16.25	17.47	17.60	17.28	15.72	16.30	15.64	14.92	16.05
Fe ₂ O ₃	13.04	14.23	7.23	7.83	14.76	18.12	15.10	6.46	4.95	8.22	6.82	9.78	8.66	8.55	2.88	8.81	8.96	8.80	8.53
CaO	12.92	9.99	6.13	4.88	8.40	6.87	8.99	7.21	4.87	8.74	3.36	7.40	7.39	7.26	2.74	5.85	8.47	7.83	7.94
MgO	4.49	6.55	3.35	3.64	7.13	5.87	6.32	4.04	2.71	4.62	4.23	5.10	4.12	5.05	1.34	4.61	4.81	4.93	5.02
MnO	0.32	0.22	0.15	0.19	0.29	0.28	0.23	0.14	0.10	0.13	0.17	0.22	0.21	0.16	0.10	0.17	0.17	0.18	0.16
Na ₂ O	2.36	1.49	2.48	2.36	2.43	2.26	0.53	1.97	3.75	0.67	5.26	1.68	2.18	1.49	2.57	3.61	0.26	0.38	0.27
K ₂ O	0.10	0.23	0.82	1.01	0.11	0.08	0.97	0.96	1.70	1.15	0.20	0.93	1.07	1.22	1.14	0.96	2.59	2.50	1.75
P ₂ O ₅	0.08	0.08	0.12	0.14	0.07	0.11	0.07	0.14	0.11	0.13	0.11	0.12	0.13	0.13	0.09	0.11	0.13	0.12	0.12
Cr ₂ O ₃	0.031	0.031	0.010	0.001	0.031	0.001	0.010	0.010	0.010	0.03	0.010	0.020	0.001	0.020	0.001	0.010	0.020	0.020	0.010
LOI	4.91	1.69	1.73	2.88	1.29	1.01	2.13	2.43	1.76	2.11	0.97	2.18	1.43	2.29	1.18	1.62	3.33	2.28	2.48
H ₂ O	0.02	0.04	0.05	0.07	0.04	-0.03	-0.04	0.02	0.09	0.04	0.05	0.04	0.02	0.05	0.08	0.05	0.05	0.02	0.01
Sum	100.10	99.75	100.14	100.40	100.22	99.70	99.61	100.14	99.78	99.61	99.92	100.21	99.82	100.05	100.16	100.22	100.48	100.39	100.00
Sc	47.84	50.44	18.96	14.61	53.40	56.75	48.62	17.52	15.13		20.45	25.27	24.66	24.88	6.98	27.58	26.60	25.69	24.38
V	316.96	313.56	130.27	99.86	330.71	423.54	302.78	107.28	93.88		125.74	155.15	146.33	155.81	40.31	161.10	159.18	148.76	146.21
Cr	183.00	227.41	67.31	28.40	217.49	19.94	137.53	104.37	125.08		113.35	168.87	46.11	132.18	22.96	107.13	171.01	173.85	133.41
Co	41.40	48.56	22.74	17.86	51.13	48.48	76.34	13.85	21.01		22.71	31.42	23.77	27.85	7.03	27.38	30.96	30.57	26.44
Ni	65.20	88.96	52.63	19.33	80.15	27.35	142.62	58.02	63.26		53.99	76.85	29.00	59.39	15.53	41.58	71.46	69.72	55.68
Cu	65.84	103.65	40.15	6.83	192.10	82.16	138.27	10.73	118.79		22.38	56.35	11.70	10.14	40.43	11.17	44.39	41.56	54.23
Zn	73.53	94.74	58.81	89.33	109.92	125.59	141.10	94.34	701.68		58.73	79.27	64.23	101.12	42.75	68.21	68.65	73.36	60.10
Rb	1.15	6.98	16.34	32.87	2.43	0.99	27.43	18.46	30.17		6.08	26.15	20.71	33.52	29.41	15.60	61.01	58.09	36.96
Sr	181.27	273.16	376.63	216.69	235.98	195.54	124.64	188.92	118.21		259.44	238.31	263.67	266.47	257.13	349.75	140.09	122.60	155.43
Y	26.56	26.43	10.56	11.89	29.07	42.92	24.53	8.69	10.28		9.59	12.59	17.62	11.89	5.35	12.89	12.87	11.88	12.19
Zr	67.10	69.80	86.29	96.15	75.11	119.85	65.71	89.27	96.96		90.14	96.26	91.07	89.25	105.87	82.57	90.74	80.50	87.00
Nb	2.36	2.54	1.97	2.97	2.73	4.21	2.47	2.79	3.25		2.79	3.27	2.90	3.08	3.50	2.44	3.05	2.65	2.79
Mo	0.97	1.09	0.80	0.85	0.85	0.96	0.89	0.90	6.32		0.71	0.81	0.57	0.91	1.45	0.91	0.77	0.94	0.75
Sn	1.36	1.57	2.56	1.35	1.86	2.15	1.83	1.42	4.34		2.12	2.03	2.26	2.05	1.08	1.24	1.35	1.76	1.60
Cs	0.17	0.58	1.75	3.57	0.28	0.34	1.97	1.41	1.46		0.40	1.79	2.26	2.15	1.53	0.78	3.45	3.06	2.70
Ba	21.38	77.23	278.76	372.28	53.70	23.99	129.61	245.00	500.74		83.29	230.62	439.87	409.84	227.47	527.81	702.27	624.32	565.26
La	3.42	3.65	9.55	16.34	3.75	6.06	3.09	13.10	11.99		11.10	10.07	12.03	12.56	14.72	10.77	12.94	10.49	11.27
Ce	8.70	9.22	21.81	33.04	9.55	14.84	8.32	27.66	25.82		21.93	21.61	26.28	26.98	29.11	22.51	26.31	22.60	23.38
Pr	1.33	1.41	2.85	3.83	1.57	2.42	1.30	3.35	3.15		2.70	2.72	3.46	3.27	2.90	2.88	3.32	2.80	3.00
Nd	7.12	8.21	12.22	15.64	8.42	13.03	6.71	14.40	13.29		11.27	12.13	15.38	14.60	9.97	12.92	14.50	12.17	13.43
Sm	2.54	2.77	2.68	2.58	2.94	4.53	2.37	2.86	2.65		2.41	2.86	3.33	2.88	1.78	2.71	2.94	2.63	2.92
Eu	0.86	0.89	0.73	0.79	1.02	1.40	0.77	0.67	0.67		0.68	0.70	0.99	0.82	0.50	0.73	0.93	0.74	0.79
Gd	3.56	3.77	2.20	2.07	3.88	6.16	3.27	2.14	2.29		1.87	2.31	3.10	2.66	1.38	2.40	2.58	2.46	2.39
Tb	0.62	0.66	0.30	0.30	0.72	1.05	0.59	0.29	0.31		0.28	0.37	0.49	0.35	0.19	0.34	0.37	0.34	0.36
Dy	4.49	4.79	2.11	1.95	5.17	7.78	4.21	1.63	1.95		1.86	2.19	3.44	2.03	1.09	2.36	2.48	1.97	2.26
Ho	0.98	1.02	0.41	0.44	1.15	1.67	0.93	0.32	0.40		0.34	0.46	0.65	0.47	0.19	0.50	0.50	0.42	0.46
Er	2.96	2.98	1.27	1.34	3.21	4.94	2.74	0.76	1.06		1.13	1.37	2.21	1.24	0.54	1.49	1.39	1.14	1.39
Tm	0.43	0.46	0.14	0.21	0.47	0.75	0.43	0.12	0.16		0.14	0.20	0.34	0.18	0.09	0.21	0.20	0.18	0.20
Yb	2.84	3.02	1.18	1.49	3.16	4.80	2.88	0.85	1.08		1.10	1.39	2.02	1.19	0.52	1.44	1.38	1.19	1.29
Lu	0.42	0.45	0.18	0.24	0.49	0.74	0.41	0.15	0.19		0.17	0.21	0.33	0.21	0.06	0.21	0.21	0.18	0.20
Hf	1.86	1.92	2.34	2.46	2.20	3.38	1.89	2.10	2.55		2.21	2.38	2.52	2.21	2.59	2.24	2.42	1.99	2.24
Ta	0.15	0.17	0.13	0.15	0.17	0.25	0.16	0.16	0.24		0.19	0.23	0.17	0.18	0.28	0.15	0.22	0.17	0.16
W	0.46	0.68	0.56	0.86	0.49	0.94	0.89	1.54	0.95		0.55	0.92	0.69	0.63	0.77	1.02	0.57	0.56	0.64
Pb	1.22	2.43	5.43	4.16	6.08	1.90	2.56	4.50	24.91		2.54	3.91	6.80	6.31	9.93	5.32	3.18	2.76	2.84
Th	0.36	0.41	0.80	2.00	0.46	0.65	0.64	1.37	1.79		1.35	1.25	1.40	1.47	2.53	1.53	1.47	2.09	1.40
U	0.09	0.09	0.24	0.49	0.12	0.15	0.12	0.36	0.60		0.38	0.36	0.40	0.38	0.68	0.33	0.36	0.32	0.34

Appendix Table 3 (continued)

GEUS ID	519624	519623	519622	519621	519620	519619	519618	519617	519616	519615	519614	519613	519612	519611	519610	519609	519608	519607	519606
Rock type	Schist	Calc-sil.	Amph.	Gran.	Schist	Amph.	Schist	Schist	Schist	Schist	Schist	Mylon.	Schist						
Strat. (m)	330.0	339.0	347.3	362.6	365.7	370.0	378.3	389.6	391.1	401.5	409.2	420.2	429.7	439.3	461.8	467.3	474.0	482.3	487.6
SiO ₂	57.81	57.52	62.59	62.16	64.62	61.76	59.19	49.44	58.07	63.16	60.48	59.90	64.42	65.21	58.30	64.25	64.47	62.89	64.37
TiO ₂	0.63	0.68	0.56	0.65	0.71	0.60	0.63	0.26	0.68	0.56	0.58	0.62	0.43	0.44	0.62	0.44	0.42	0.44	0.45
Al ₂ O ₃	16.19	18.26	15.21	16.11	18.71	15.91	15.32	6.67	15.03	13.73	16.40	15.56	16.34	16.25	15.95	15.46	15.93	16.43	16.52
Fe ₂ O ₃	8.76	8.28	7.89	8.04	7.22	7.51	7.62	10.73	8.63	6.36	7.00	7.87	5.43	5.42	8.03	5.37	5.53	5.69	5.13
CaO	6.67	6.81	6.78	4.87	0.70	6.01	5.45	17.70	8.30	7.60	6.52	5.72	4.48	3.20	5.89	5.36	5.04	4.69	3.54
MgO	4.69	2.81	4.89	3.91	2.22	4.82	4.28	11.97	5.41	5.74	4.10	4.82	3.01	2.68	4.76	2.64	2.43	2.88	3.08
MnO	0.16	0.15	0.18	0.16	0.09	0.16	0.14	0.53	0.22	0.16	0.13	0.13	0.15	0.15	0.26	0.14	0.19	0.17	0.10
Na ₂ O	2.61	2.01	1.42	1.37	1.06	1.59	3.84	bd	0.85	0.44	0.74	2.55	2.71	4.14	3.99	3.04	3.01	3.73	3.38
K ₂ O	0.95	0.96	0.11	0.98	2.46	0.69	0.36	0.03	0.95	0.13	2.27	0.97	0.67	0.71	0.83	0.68	1.11	1.07	1.24
P ₂ O ₅	0.13	0.15	0.11	0.13	0.13	0.11	0.15	0.08	0.17	0.08	0.11	0.10	0.11	0.11	0.16	0.11	0.11	0.12	0.12
Cr ₂ O ₃	0.020	0.010	0.020	0.020	0.020	0.020	0.020	0.001	0.020	0.010	0.010	0.010	0.001	0.001	0.020	0.001	0.001	0.001	0.001
LOI	1.29	1.57	0.69	2.26	2.17	1.40	2.82	2.77	1.61	2.46	1.45	1.16	1.89	1.49	1.38	1.97	1.47	1.52	2.00
H ₂ O-	0.01	0.01	0.04	0.18	0.14	0.21	0.03	0.08	-0.01	0.10	0.05	0.01	0.09	0.02	0.02	0.04	0.05	0.16	0.16
Sum	99.93	99.23	100.49	100.83	100.26	100.80	99.85	100.25	99.94	100.53	99.85	99.43	99.74	99.83	100.21	99.50	99.77	99.80	100.11
Sc	30.87	20.84	20.39	25.67	27.39	25.81	17.97	10.78	23.68	20.03	20.39	22.98	14.75	14.89	24.01	14.03	14.27	13.47	13.33
V	173.49	124.26	129.66	142.78	144.72	149.13	117.57	87.68	151.37	117.46	129.66	144.98	75.58	82.85	151.32	73.36	81.18	94.03	81.26
Cr	174.16	102.55	124.18	161.39	160.53	175.24	139.35	49.89	164.35	93.10	124.18	98.84	43.72	46.87	127.43	43.44	45.84	47.20	42.56
Co	35.55	21.29	25.69	27.70	23.75	29.89	21.83	24.08	27.35	20.79	25.69	27.45	12.39	16.14	24.36	11.84	15.51	11.66	7.34
Ni	76.18	39.36	55.12	69.00	51.06	70.16	52.31	36.55	61.93	30.38	55.12	46.54	20.86	24.01	48.13	21.20	22.28	24.19	19.54
Cu	55.08	9.60	8.32	32.14	149.52	61.73	8.71	8.01	75.11	27.46	8.32	36.43	10.58	13.60	11.27	6.23	24.79	10.33	10.49
Zn	78.47	65.36	107.49	64.60	160.05	71.73	54.37	40.14	68.29	55.62	107.49	67.42	61.06	50.56	103.31	52.97	69.41	128.85	53.87
Rb	24.05	36.18	2.25	23.35	51.02	17.23	6.66	0.55	21.53	4.77	2.25	22.70	13.51	23.80	20.28	12.98	21.29	19.17	28.48
Sr	208.40	314.69	255.14	330.88	278.11	417.72	174.13	169.33	266.52	124.97	255.14	223.51	351.32	457.05	426.62	417.69	314.32	316.35	258.51
Y	14.53	12.69	10.43	13.12	11.25	11.13	9.80	7.36	14.05	10.33	10.43	12.60	7.46	10.04	12.67	7.60	9.31	12.98	4.61
Zr	103.95	92.34	80.24	100.03	99.51	105.31	80.94	36.04	118.19	76.25	80.24	89.44	93.20	107.98	97.75	94.56	100.60	105.45	93.58
Nb	3.40	2.87	2.49	3.21	3.40	3.13	2.84	1.37	4.08	2.02	2.49	2.72	2.65	3.14	2.67	2.67	2.98	3.11	2.80
Mo	1.02	0.91	0.88	0.97	0.81	0.89	0.78	1.11	0.92	1.16	0.88	0.91	0.76	1.03	0.94	0.67	2.87	0.94	1.06
Sn	2.16	1.68	1.40	1.66	1.78	1.54	0.83	1.12	1.54	2.20	1.40	1.57	1.37	1.66	1.39	1.29	1.82	2.16	1.49
Cs	3.29	4.16	0.30	2.64	3.76	2.30	1.29	0.11	1.49	1.04	0.30	2.11	0.71	0.83	0.87	0.47	1.48	0.94	2.18
Ba	728.34	547.84	47.01	174.45	610.11	330.49	110.16	22.36	205.69	36.62	47.01	487.33	417.18	431.43	430.89	393.14	789.44	576.10	463.79
La	14.37	11.71	8.56	12.16	10.89	13.96	11.82	8.39	17.00	8.98	8.56	14.37	13.50	12.71	33.35	12.06	17.36	32.52	3.43
Ce	27.95	25.26	17.53	24.93	23.40	27.87	25.71	16.61	34.95	18.28	17.53	30.50	30.06	35.27	52.31	24.10	31.10	60.46	5.50
Pr	3.70	3.23	2.20	3.21	2.93	3.62	3.04	2.15	4.45	2.38	2.20	3.88	3.34	3.40	7.63	2.81	3.91	7.20	0.65
Nd	16.11	14.11	9.88	14.14	12.68	15.01	13.12	9.30	19.44	10.18	9.88	17.36	13.58	13.92	32.25	11.52	16.12	29.84	2.70
Sm	3.42	3.09	1.95	2.80	2.60	3.04	2.60	2.10	3.64	1.97	1.95	3.45	2.20	2.85	5.09	2.23	2.65	4.17	0.47
Eu	0.96	0.86	0.64	0.87	0.60	0.86	0.76	0.56	1.04	0.54	0.64	1.07	0.66	0.69	1.18	0.67	0.71	1.55	0.28
Gd	2.88	2.72	1.81	2.52	2.10	2.23	1.98	1.80	3.12	2.09	1.81	2.79	1.93	2.05	3.41	1.64	2.11	3.14	0.45
Tb	0.44	0.37	0.27	0.37	0.33	0.35	0.28	0.25	0.48	0.31	0.27	0.40	0.26	0.33	0.40	0.23	0.28	0.38	0.09
Dy	2.75	2.39	1.90	2.48	2.07	2.11	1.81	1.49	2.77	1.87	1.90	2.45	1.47	1.84	2.39	1.52	1.76	2.54	0.67
Ho	0.54	0.48	0.42	0.50	0.42	0.42	0.34	0.27	0.55	0.37	0.42	0.48	0.30	0.37	0.51	0.30	0.35	0.44	0.15
Er	1.54	1.27	1.26	1.47	1.30	1.22	0.99	0.73	1.49	1.00	1.26	1.35	0.78	1.12	1.37	0.88	1.01	1.46	0.56
Tm	0.24	0.21	0.18	0.25	0.18	0.19	0.13	0.12	0.21	0.12	0.18	0.21	0.13	0.21	0.19	0.13	0.17	0.16	0.10
Yb	1.56	1.35	1.19	1.39	1.17	1.37	0.96	0.61	1.49	1.01	1.19	1.32	0.83	1.13	1.31	0.91	1.13	1.37	0.75
Lu	0.25	0.19	0.19	0.22	0.18	0.19	0.15	0.10	0.23	0.15	0.19	0.19	0.15	0.20	0.20	0.14	0.17	0.19	0.11
Hf	2.71	2.37	2.20	2.61	2.54	2.67	1.84	1.03	3.12	1.98	2.20	2.57	2.33	2.85	2.51	2.42	2.72	2.55	2.57
Ta	0.22	0.18	0.17	0.20	0.23	0.21	0.17	0.08	0.24	0.14	0.17	0.18	0.18	0.21	0.14	0.19	0.19	0.20	0.18
W	0.69	0.42	0.65	0.55	0.57	0.73	0.34	0.86	0.56	3.58	0.65	0.51	0.42	0.55	0.57	0.72	0.95	1.05	0.60
Pb	4.28	4.79	10.50	4.51	4.00	5.48	2.65	2.75	3.34	3.12	10.50	4.63	5.74	4.63	5.30	5.48	5.23	83.22	4.56
Th	1.65	1.41	1.23	1.62	1.53	1.70	1.27	0.89	2.09	1.73	1.23	1.79	2.11	2.47	3.41	2.25	2.48	2.53	2.14
U	0.31	0.34	0.29	0.37	0.38	0.46	0.34	0.21	0.45	0.31	0.29	0.35	0.39	0.58	0.53	0.47	0.49	0.71	0.54

Appendix Table 3 (continued)

GEUS ID	519605	519604	519603	519602	519601
Rock type	Schist	Schist	Schist	Schist	Schist
Strat. (m)	510.3	517.9	525.4	535.6	544.2
SiO₂	63.77	63.36	63.90	64.02	64.15
TiO₂	0.44	0.44	0.45	0.44	0.45
Al₂O₃	15.94	16.31	16.56	16.36	16.36
Fe₂O₃	5.63	6.02	6.02	5.71	5.55
CaO	4.93	3.90	4.09	4.54	4.61
MgO	3.04	3.01	2.92	2.64	2.52
MnO	0.14	0.12	0.10	0.10	0.11
Na₂O	3.27	3.74	3.42	3.87	2.77
K₂O	1.24	1.45	1.32	0.74	1.49
P₂O₅	0.12	0.12	0.11	0.12	0.11
Cr₂O₃	0.001	0.001	0.010	0.001	0.001
LOI	0.74	1.19	0.93	0.86	1.62
H₂O-	0.04	0.08	0.08	0.15	0.25
Sum	99.31	99.74	99.90	99.55	99.99
Sc	13.38	15.43	14.47	13.54	15.51
V	71.74	90.40	87.78	88.62	86.28
Cr	53.36	52.51	47.84	50.01	52.40
Co	12.29	9.93	12.66	7.37	8.02
Ni	23.87	28.31	23.87	23.19	23.76
Cu	5.77	18.30	8.49	33.31	28.96
Zn	78.35	78.55	75.42	81.62	82.09
Rb	25.57	39.33	26.41	19.64	39.28
Sr	349.79	422.12	450.45	502.89	582.32
Y	8.48	11.80	10.86	9.51	7.49
Zr	82.33	105.36	98.71	100.93	97.47
Nb	2.43	3.00	2.97	2.96	2.93
Mo	1.27	1.11	1.22	1.00	1.41
Sn	1.49	1.41	1.65	1.74	1.61
Cs	1.72	2.72	2.23	1.30	2.53
Ba	488.26	858.18	639.01	387.83	646.42
La	17.34	26.81	25.34	9.32	9.29
Ce	35.20	37.79	37.48	16.24	17.91
Pr	4.21	5.80	5.53	2.24	2.20
Nd	16.42	23.18	21.87	9.52	8.99
Sm	2.74	3.72	3.65	2.02	1.42
Eu	0.76	1.04	0.91	0.65	0.47
Gd	2.04	3.22	2.89	1.70	1.33
Tb	0.28	0.36	0.36	0.25	0.19
Dy	1.57	2.43	2.17	1.77	1.33
Ho	0.33	0.46	0.39	0.33	0.26
Er	0.89	1.30	1.14	1.07	0.94
Tm	0.14	0.19	0.15	0.16	0.13
Yb	0.93	1.10	1.10	1.06	0.98
Lu	0.15	0.19	0.16	0.16	0.15
Hf	2.25	2.70	2.54	2.67	2.56
Ta	0.14	0.21	0.20	0.22	0.20
W	0.49	0.51	0.64	0.49	0.44
Pb	5.60	6.06	6.97	13.75	25.38
Th	1.85	2.32	2.22	8.43	2.32
U	0.43	0.41	0.49	0.56	0.44

Figure 6

